Experimentally-Driven Model for the Baffled-Tube Ram Accelerator

Trever J. Byrd

A thesis
submitted in partial fulfillment of the
requirements for the degree of

Master's of Science

University of Washington

2018

Committee:

Carl Knowlen, Chair

Adam Bruckner

Program Authorized to Offer Degree:
Aeronautics and Astronautics

University of Washington

Abstract

Experimentally-Driven Model for the Baffled-Tube Ram Accelerator

Trever J. Byrd

Chair of the Supervisory Committee:
Associate Research Professor Carl Knowlen
Aeronautics and Astronautics

The baffled-tube ram accelerator is a hypervelocity mass driver with the capability to become a reusable space launch technology. The device is a derivative of a smooth-bore ram accelerator in that it uses a series of washer-like internal baffles, normal to the tube wall, as obstructions to attenuate the combustion-driven shock wave system associated with the ram accelerator's propulsive cycle. The device with baffles normal to the wall produces 30-100% more thrust than the conventional smooth-bore ram accelerator. The attenuation effected by the baffles allows for higher energy propellants to be utilized, thus enabling a higher level of thrust to be produced. However, compared to the performance model of the ram accelerator, the normal-baffled-tube only produces a fraction of the predicted thrust. To realize the full potential of the device a set of slanted internal baffles was designed, manufactured, and tested. The slanted baffles were tested with both an inward slant and outward slant configuration with respect to the direction of motion. From preliminary tests outward slanted baffles showed a 41% increase in thrust with 20% more diluent in the propellant mixture than in the normal-baffled-tube, which, however, was still less than predicted. A modified performance model was developed to accounted for the combustion efficiency of the baffled-tube ram accelerator. This model has shown the combustion efficiency plays a predominant role in the under-performance of the baffled-tube ram accelerator. Furthermore, by coupling the combustion efficiency and baffle drag the model lent insight into how the ram accelerator

performed differently with baffles. The slanted-baffled-tube experiments are presented along with the results of the modified performance model, as applied to the experimental data for both baffle geometries.

TABLE OF CONTENTS

LIST OF FIGURES

LIST OF TABLES

NOMENCLATURE

Variables

β	Volume Void Ratio
Δq	Heat Release
$\dot{q}$	Heat Release Rate
η_β	Void Volume Efficiency
η_q	Combustion Efficiency
$\frac{L}{D}$	Aspect Ratio
γ	Specific Heat Ratio
λ	Control Volume Area Corrective Factor
ϕ	Equivalence Ratio
Ψ	Shear Stress
ρ	Density
τ	Time Constant
A	Area
a	Acceleration
a	Acoustic Speed
c_d	Drag Coefficient
c_f	Friction Coefficient
c_p	Specific Heat Capacity at Constant Temperature
D	Drag
d	Diameter
F	Thrust Force
h	Specific Enthalpy
I	Non-Dimensional Thrust
L	Length
M	Mach Number
m	Mass
P	Pressure

Q Non-Dimensional Heat Release

R Gas Constant

T Temperature

t Time

u velocity

V Volume

Superscripts and Subscripts

$*$ Choked State

1 Entrance State

2 Thermally Choked Exit State

b Tube-Bore

$BTRA$ Baffled-Tube Ram Accelerator

c Baffle Chamber

$c.v.$ Control Volume

eff Effective

EM Electromagnetic Probe

exp Experimental

f Final

i Initial

lab Laboratory Reference Frame

p Projectile

p, b Axial Projected Baffle Area

$SBRA$ Smooth Bore Ram Accelerator

t Stagnation State

u Universal

w Wall Between Baffles

LIST OF ABBREVIATIONS

BTRA: Baffled-Tube Ram Accelerator

CAD: Computer Aided Design

CFD: Computational Fluid Dynamics

CJ: Chapman-Jouguet

EM: Electromagnetic

FEA: Finite Element Analysis

MFC: Mass Flow Controller

SBRA: Smooth Bore Ram Accelerator

TCRA: Thermally-Choke Ram Accelerator

UW: University of Washington

ACKNOWLEDGMENTS

First I'd like to thank my advisor Dr. Carl Knowlen for presenting me with the opportunity to explore the technical challenges of the ram accelerator. My time working with him has taught me invaluable lessons about gasdynamics, thermodynamics, and the ram accelerator. As a member of my thesis committee, I'd like to thank Dr. Adam Bruckner; as one of the people around during the being of the ram accelerator; for giving me feed back on my work with the baffled-tube ram accelerator.

A special thanks to Colin Hamburg for teaching me the ins and outs of the experimental procedure in the ram accelerator laboratory. With his help it was a seamless transition from one research assistant to another. Navid Daneshvaran for his incredible computation fluid dynamics work in on the baffled-tube ram accelerator. His simulations proved insight into the flow dynamics present in the baffled-tube. Jeff Glusman for conducting the preliminary baffled-tube experiments and exploring combustion efficiency which became the catalyst for my own work. Without funding from EnergeticX.net, LLC and the Washington Research Foundation (WRF) the baffled-tube ram accelerator would not be possible.

Last but certainly not least I'd like to thank the research assistances that put countless hours into helping setup for each shot and giving me feed back on my ideas. Specifically Ty Mundt, Clay Davis, Kimmy Liu, Chinmay Upadhye, Nick Kano, Andrew Hadford, Jeremy Nguyen, and Matthew Edwards.

DEDICATION

to my mother, Rondella; sister, Kylie; and niece, Cali for always encouraging me to follow my dream and never give up

Chapter 1

INTRODUCTION

The ram accelerator is a hypervelocity chemical mass driver that was developed to be an alternative space launch system. The first stage of conventional rockets require large propellant tanks which add more weight and reduce the allowable payload mass. In the end, only a fraction of the overall rocket weight is payload. With the ram accelerator, payloads can be driven to suborbital speeds from ground level, inside a projectile, making the first stage of a rocket obsolete and drastically increasing the mass of payload that can be placed in orbit per launch. Future applications also include interplanetary launches from celestial bodies with lower escape velocities than Earth. In the 1980s an experimental ram accelerator was developed at the University of Washington. It possessed a 38 millimeter bore, a length of 16 meters, and a maximum exit velocity of 2.7 kilometers per second. The U.S. Army Research Laboratory (ARL) and the French-German Research Institution (ISL) proved the scalability of the technology with a 120 millimeter bore and 90 millimeter bore, respectively. The ram accelerator propulsive cycle works similar to a ramjet (Fig. 1.1).

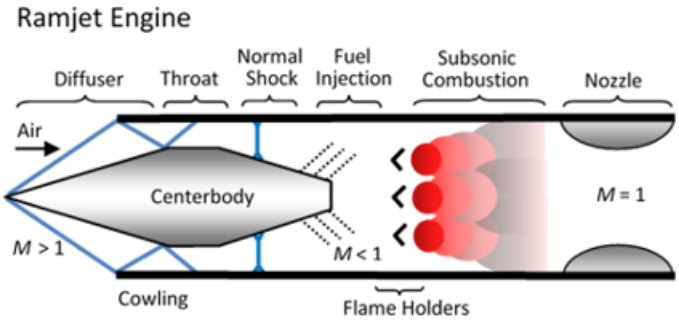

Figure 1.1: Conventional air-breathing ramjet

Instead of a center-body with an attached cowling the ram accelerator utilizes a projectile and stationary tube wall. Alternative to ingesting oxidizer from the atmosphere and injecting fuel, the projectile is launched at supersonics speeds, via gas gun, into a charge of premixed oxidizer and fuel. Similarly, a shock systems decelerates the supersonics flow and initiates the subsonic combustion. The energy release increases the local pressure and temperature accelerating the flow to a thermally choked state. The high pressure region created between the shock system and thermally choke plane driving the projectile forward. The propulsive mode where this occurs was dubbed the thermally-choke ram accelerator (Fig. 1.2). As the projectile accelerates the shock system recedes towards the base of the projectile eventually falling off. If the projectile's base tapered to a point, the velocity of the projectile would approach the Chapman-Jouguet (CJ) detonation speed when the shock system recede to the end of the projectile [2].

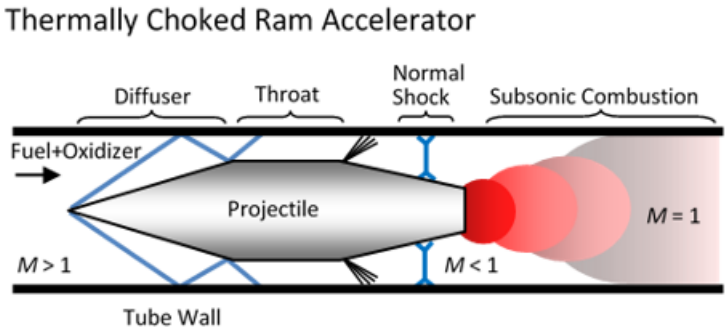

Figure 1.2: Thermally-choked ram accelerator propulsive cycle

The operational envelope of the thermally choked smooth-bore ram accelerator has been explored throughly. As a result of this dedicated research two main limitation were identified. The first was projectile Mach number which must satisfy conditions to maintain supersonic flow over the projectile body for a given area ratio and out-pace the combustion driven shock system attached to the projectile body. The second was the heat release of the propellant during the combustion process. A propellant mixture with excess energy causes the combustion to drive the shock system passed the projectile and with a lack of energy

the shock system can recede off the base of the projectile. The former was referred to as an unstart and the latter wave-fall off. The term "unstart" refers to the shock system disgorging from the projectile exposing it only to subsonic flow, thus no longer providing the conditions to produce thrust. A model to predict these limitation in terms of Mach number and non-dimensional heat release will be discussed in detail later in Chapter 2.

To expand the operational envelope and relax the TCRA limitation a device call the baffled-tube ram accelerator was design, built, and tested. The in-tube baffles were washer-like flow obstructions meant to attenuate the surging shock system and allow more energetic propellants to be used (Fig. 1.3). An initial theoretical model of the BTRA was developed to directly compare the performance to the traditional TCRA. The model predicted elevated thrust at low Mach numbers due to a "negative drag" from the flow moving away from the projectile and building pressure against an aft baffle. Preliminary experiments showed a 30 to 100% increase in thrust with 40 to 70% more heat release than the SBRA at similar fill pressures [3]. However, this was still 30 to 50% less then the potential thrust predicted from the initial model. To realize the full potential of the BTRA a set of slanted baffles was design, installed, and tested. A modified model to better understand the gasdynamics of the BTRA for both geometries was developed in conjunction. The methodology and results for the model will be describe in detail in Chapter 5.

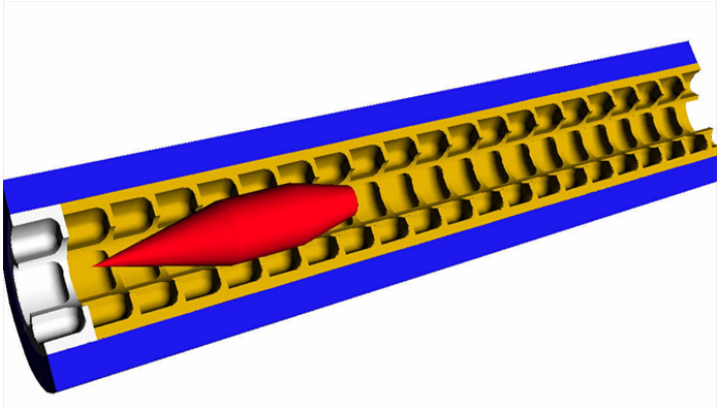

Figure 1.3: Normal baffled-tube ram accelerator illustration

Chapter 2

THEORETICAL MODELS

This chapter will discuss the theoretical models when considering the ram accelerator. The original thermodynamic model for the thermally-choked ram accelerator is presented as well as a model for its operational limits. Building off of the original TCRA model, an overview of the initial BTRA performance model is presented alongside a modified BTRA performance model with experimentally-driven constants.

2.1 Thermally-Choked Smooth-Bore Ram Accelerator

The propulsive mode which utilizes subsonic heat addition and a resulting sonic plane behind the projectile is referred to as the thermally-choked ram accelerator (TCRA). The thermally-choked plane stabilizes a shock system on the projectile body establishing a quasi-steady process. By assuming 1-dimensional flow the thrust from the TCRA can be determined by the conditions of the flow upstream of the projectile, the downstream thermally-choked flow, and the heat addition produced by the subsonic combustion. To do this the projectile is surrounded by a control volume, Fig. 2.1, where boundary 1 and 2 are the entrance and exit planes, respectively; relative to the projectile. Since the entrance plane and thermally choked exit plane are entropy extremum [1] the flow phenomena inside the control volume can be neglected. The conservation laws are applied to the control volume where they are normalized and solved simultaneously.

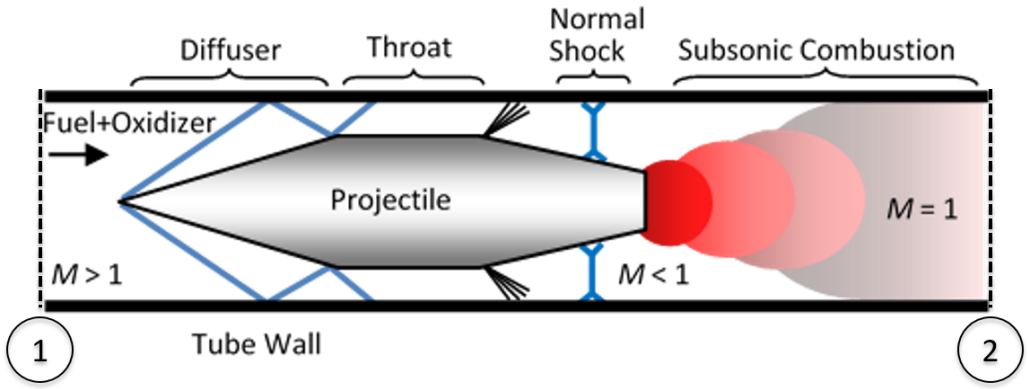

Figure 2.1: Smooth bore ram accelerator control volume

Applying conservation of momentum to the control volume results in

$$P_1 A_1 + \rho_1 u_1^2 A_1 + F = P_2 A_2 + \rho_2 u_2^2 A_2 \tag{2.1}$$

which can be simplified further by recognizing that $A_1 = A_2 = A_b$, where A_b refers to the cross sectional area of the tube bore. Eq. 2.1 is then normalized by the constant area and the pressure at boundary 1, P_1.

$$1 + \frac{\rho_1 u_1^2}{P_1} + \frac{F}{P_1 A} = \frac{P_2}{P_1} + \frac{\rho_2 u_2^2}{P_1}$$

Using the ideal gas law ($P = \rho RT$) and the definition of the local acoustic speed ($a = \sqrt{\gamma RT}$) the above equation can be put in terms of Mach number ($M = \frac{u}{a}$).

$$\frac{F}{P_1 A} = \frac{P_2}{P_1}(1 + \gamma_2 M_2^2) - (1 + \gamma_1 M_1^2) \tag{2.2}$$

With the conservation of mass ($\rho_1 u_1 A_1 = \rho_2 u_2 A_2$), ideal gas, and acoustic speed equations the ratio $\frac{P_2}{P_1}$ can be put into terms of Mach number, gas constants, and temperature.

$$\frac{P_2}{P_1} = \frac{M_1 \sqrt{\gamma_1 R_2 T_2}}{M_2 \sqrt{\gamma_2 R_1 T_1}} \tag{2.3}$$

Next, the conservation of energy equation is applied to the control volume; where Δq is the change in the heat of formation, referenced at zero Kelvin, from boundary 1 to boundary

2:

$$\rho_1 u_1 A_b[h_1 + \frac{u_1^2}{2} + \Delta q] = \rho_2 u_2 A_b[h_2 + \frac{u_2^2}{2}] \tag{2.4}$$

Dividing the equation by $\rho_1 u_1$ and utilizing the conservation of mass equation results in:

$$h_1 + \frac{u_1^2}{2} + \Delta q = h_2 + \frac{u_2^2}{2} \tag{2.5}$$

Then the equation is put in terms of Mach number.

$$h_1 + \frac{M_1^2 \gamma_1 R_1 T_1}{2} + \Delta q = h_2 + \frac{M_2^2 \gamma_2 R_2 T_2}{2}$$

To create dimensionless variables, the energy equation in this form is normalized by $c_{p1}T_1$. This introduced the non-dimensional heat release term ($Q = \frac{\Delta q}{c_{p1}T_1}$) which is an important independent variable when determining the SBRA thrust performance. Properly manipulating the gas constants and specific heats result in the below equation.

$$\frac{h_1}{c_{p1}T_1} + \frac{\gamma_1 - 1}{2} M_1^2 + Q = \frac{h_2}{c_{p1}T_1} + \frac{\gamma_2 - 1}{2} M_2^2 \frac{c_{p2}T_2}{c_{p1}T_1}$$

Manipulating this equation further to find the ratio $\frac{T_2}{T_1}$ allows the expression Eq. 2.3 to be solved uniquely in terms of the non-dimensional heat release, Q, and boundary Mach numbers.

$$\frac{T_2}{T_1} = \frac{c_{p1}}{c_{p2}} \left(\frac{Q + \frac{h_1}{c_{p1}T_1} + \frac{\gamma_1 - 1}{2} M_1^2}{\frac{h_2}{c_{p2}T_2} + \frac{\gamma_2 - 1}{2} M_2^2} \right) \tag{2.6}$$

Combining Eq. 2.6, Eq. 2.3, and Eq. 2.2 results in the non-dimensional thrust equation for the smooth-bore ram accelerator.

$$\frac{F}{P_1 A_b} = \frac{M_1 \gamma_1}{M_2 \gamma_2} (1 + \gamma_2 M_2^2) \sqrt{\frac{\gamma_2 - 1}{\gamma_1 - 1} \left(\frac{Q + \frac{h_1}{c_{p1}T_1} + \frac{\gamma_1 - 1}{2} M_1^2}{\frac{h_2}{c_{p2}T_2} + \frac{\gamma_2 - 1}{2} M_2^2} \right)} - (1 + \gamma_1 M_1^2)$$

Finally, applying the thermally choked assumption to the exit boundary of the control volume simplifies the expression to the non-dimensional thrust for a thermally-choked propulsive mode.

$$I_{SBRA} = \frac{F}{P_1 A_b} = M_1 \frac{\gamma_1}{\gamma_2} (1 + \gamma_2) \sqrt{\frac{\gamma_2 - 1}{\gamma_1 - 1} \left(\frac{Q + \frac{h_1}{c_{p1}T_1} + \frac{\gamma_1 - 1}{2} M_1^2}{\frac{h_2}{c_{p2}T_2} + \frac{\gamma_2 - 1}{2}} \right)} - (1 + \gamma_1 M_1^2) \tag{2.7}$$

The thrust of the TCRA is now solely in terms of the local Mach number of the projectile inside a given propellant and its non-dimensional heat release. With two independent variables the thrust performance can be plot as a three dimensional envelope, Fig. 2.1.

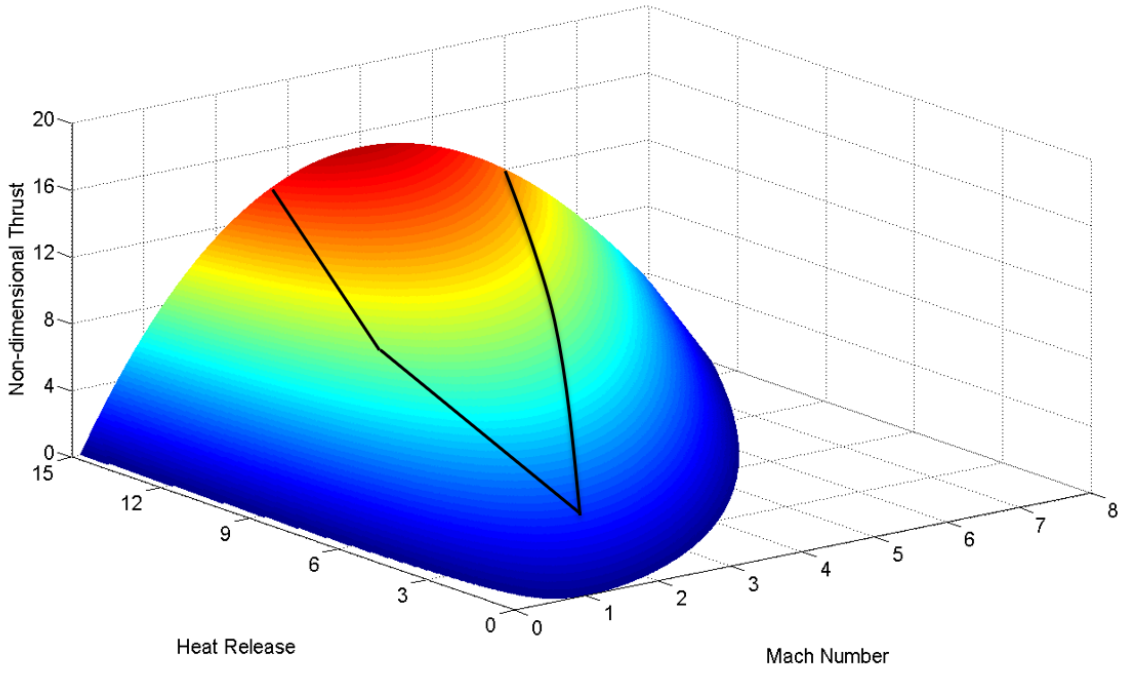

Figure 2.2: TCRA non-dimensional thrust envelope

From the thrust envelope it can be seen for a given heat release there is a peak thrust Mach number and zero thrust Mach number. As the heat release increases the Mach number where these features occur also increases, effectively widening the thrust envelope. The zero thrust Mach number is of special interest because this is the Chapman-Jouget Mach number for a given chemistry [1]. Due to the thermally choked exit plane assumption the propulsive cycle cannot accelerate the projectile pass the CJ speed. This is where the mode of propulsion would transition from sub-detonative to super-detonative ($M_2 > 1$), which will not be discussed in detail in this paper. In reality the heat release is not constant as Mach number varies due to the changing equilibrium condition. However, in practice the

non-dimensional heat release is held constant at the CJ condition. Other features of the expression include the scaling implications of the normalized thrust. It suggests that the thrust of the propulsive cycle can be scaled linearly with bore area and fill pressure.

The non-dimensional thrust theory for the TCRA has been tested in several propellants and at different Mach number. Fig. 2.3 shows an example of a test conducted where the projectile transits in to different propellants charges as it is accelerated. This experiment was designed to keep the projectile at the peak thrust Mach number during operation. The Eq. 2.7 was used to determine velocity as a function of distance along the 16-m long tube. The dots are experimental values while the dashed line is the theoretical curve. The excellent correlation between theory and experiment validates the gasdynamic and thermally-chocked assumptions made in the derivation. However, in Fig. 2.3 there is also a theoretical curve for mixtures that would result in maximum thrust for this given experiment. Upon testing it was learned that the TCRA has limitations in entrance Mach number and heat release.

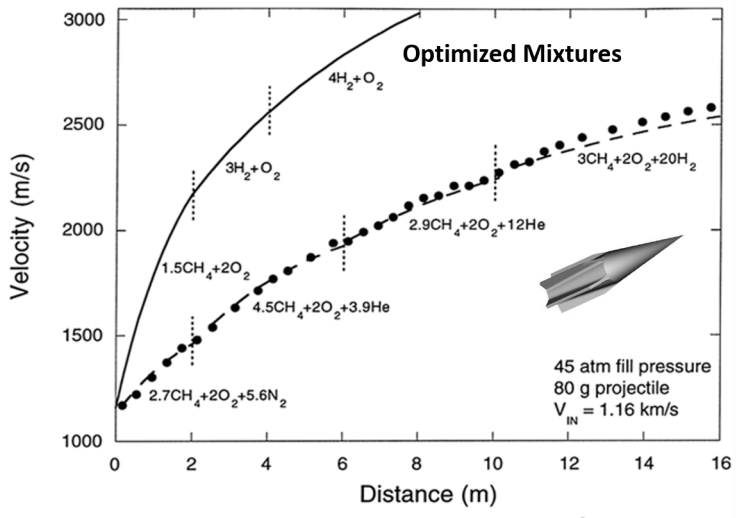

Figure 2.3: TCRA experimental-theoretical correlation velocity profile when using optimized mixtures

2.2 TCRA Limitations

Regardless of how well the above theory predicts the thrust of the TCRA, it does not take into account the gasdynamics required to obtain the stable state necessary for the control volume analysis. In the early stages of ram accelerator development a one-dimensional flow field model was utilized to predict the TCRA operational limits [4]. To start, The model predicted a projectile entrance Mach number and area ratio sufficient to maintain supersonic flow through its throat, or largest diameter. Isentropic compression (Eq. 2.8) was used to approximate the minimum Mach number for the given area ratio to achieve the supersonic flow condition. A is the tube bore area and A^* is the annular area between the tube bore and projectile throat.

$$\frac{A}{A^*} = \frac{1}{M}\left(\frac{\frac{\gamma+1}{2}}{1+\frac{\gamma-1}{2}M_1^2}\right)^{\frac{\gamma+1}{2(1-\gamma)}} \tag{2.8}$$

Furthermore, the model predicted a required heat release, Δq, that is sufficient to stabilize a shock system on the projectile body but not drive the shock system passed its throat. As a result of these requirements the model imposed three limits on the operation of the ram accelerator.

As mentioned above the first limit is the minimum Mach number of the projectile for a given area ratio. Below the requisite minimum Mach number the flow will choke at the projectile nose cone causing subsonic flow over the projectile. The second is a gasdynamic limit which imposes a maximum on the heat release of the propellant. Above this maximum the shock system upstream of the heat addition is driven forward and eventually surpasses the projectile. The phenomenon is called unstart, which describes the normal shock pushing in front of the projectile resulting in high pressure behind it and a net drag on the projectile. The last limit is a minimum propellant heat release. If the heat addition is insufficient to drive the shock system at the same speed as the projectile enters the propellant the system recedes until it falls off from the projectile. This is referred to as wave fall-off. These three limits are expressed in terms of non-dimensional heat release, Q, and projectile Mach number. The relationship is shown in Fig. 2.4.

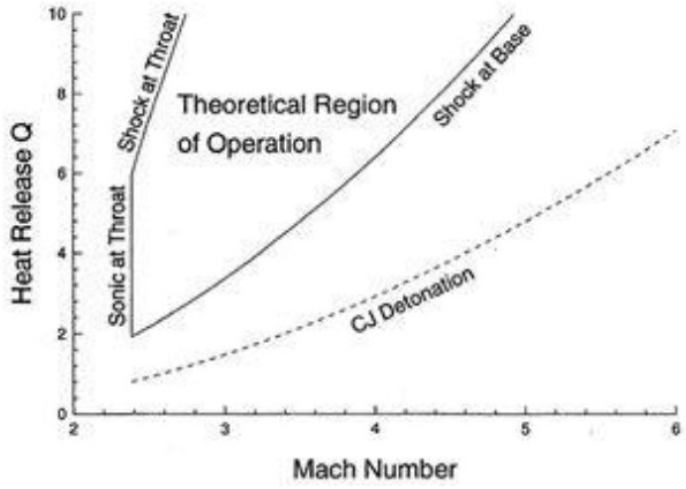

Figure 2.4: Theoretical operational envelop for TCRA

The minimum Mach number was approximated to be 2.4 for a projectile with a 29 millimeter throat diameter, bore diameter of 38 millimeters, and $\gamma = 1.4$. As the projectile is accelerated, if the heat release minimum is not sufficient wave fall-off occurs. On the other hand, if the heat release is above the maximum value an unstart occurs. To tailor the heat release of a propellant mixture to meet the operational requirements, diluent can be added. Diluent takes two forms, excess fuel or inert gas. In Ref. [4] the effects of the two diluent methods where explored.

2.3 Baffled-Tube Ram Accelerator

For the passed decade the baffled-tube ram accelerator has been at the center of research to expand the TCRA operational envelope. It was conceptualized to attenuated the shock system on the projectile body and isolate the inlet conditions from the combustion influences. Essentially the baffles would act as a one way valve for the propellant (Fig. 2.5). This would allow the use of higher energy mixtures since the combustion, in theory, would not drive the shock system forward and cause an unstart.

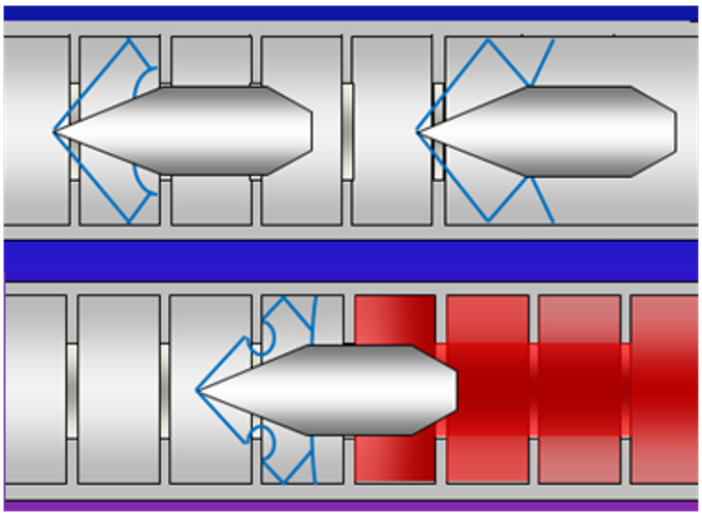

Figure 2.5: Normal baffled-tube inlet-combustion isolation

An added benefit to expanding the allowable heat release for the TCRA is a reduction in minimum entrance Mach number. Applying similar isentropic compression analysis (Eq. 2.8) to the baffled-tube resulted in a lower entrance Mach number limit. With a 37 millimeter projectile throat diameter and 76 millimeter chamber diameter, the minimum entrance Mach number was reduced to 1.7. However, so far no flow field model as been produced to predict the limits of operation similar to the TCRA limits.

2.4 Initial Baffled-Tube Ram Accelerator Performance Model

In 2016 [5] a performance model for the BTRA was proposed. It intended to draw a direct analogy to the SBRA performance. First, it took into account the complex internal geometry of the baffled-tube. Without a constant bore area to normalize the thrust; an effective area, A_{eff}, had to be introduced. Second, the SBRA non-dimensional thrust equation was re-derived with a drag term indicating lost projectile momentum and energy to the baffles. The drag term required an accompanying model which applied the drag to the high pressure region between the shock system and thermally choked plane.

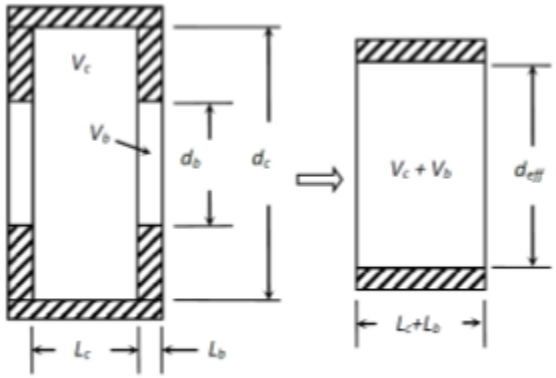

Figure 2.6: Schematic of baffle effective area

The effective area was defined as follows

$$\frac{1}{A_eff} = \frac{L_c + L_b}{V_c + V_b}$$

where $L_c + L_b$ denotes the total length of the baffle and $V_c + V_b$ denotes the total volume of the baffles. Fig. 2.6 illustrates the dimensions used to equate the baffle geometry to a smooth bore constant area. Expanding the lengths and volumes further results in

$$\frac{1}{A_{eff}} = \frac{L_c + L_b}{V_c + V_b} = \frac{1 + \frac{L_c}{L_b}}{A_b[1 + (\frac{d_c^2}{d_b^2})(\frac{L_c}{L_b})]} = \frac{1}{A_b\beta} \tag{2.9}$$

Finally the effective area was applied to the non-dimensional thrust derived in Section 2.1 (Eq. 2.7).

$$I_{BTRA} = \frac{F}{P_1 A_{eff}} = \frac{F}{P_1 A_b \beta} = \frac{I_{SBRA}}{\beta} \tag{2.10}$$

To take into account the momentum and energy loss to the baffles during projectile transit the non-dimensional thrust equation was re-derived with a drag term. The affected conservation equation of momentum and energy are stated below, respectively, with the drag loss term.

$$P_1 A_{eff} + \rho_1 u_1^2 A_{eff} + F - D = P_2 A_{eff} + \rho_2 u_2^2 A_{eff}$$

$$\rho_1 u_1 A_{eff}[h_1 + \frac{u_1^2}{2} + \Delta q] - D u_1 = \rho_2 u_2 A_{eff}[h_2 + \frac{u_2^2}{2}]$$

Following the same procedure as Section 2.1 the baffled-tube non-dimensional thrust was derived to be:

$$I_{BTRA} = \frac{F}{P_1 A_{eff}} = M_1 \frac{\gamma_1}{\gamma_2}(1+\gamma_2)\sqrt{\frac{\gamma_2 - 1}{\gamma_1 - 1}\left(\frac{Q + \frac{h_1}{c_{p1}T_1} + \frac{\gamma_1 - 1}{2}M_1^2 - \frac{D(\gamma_1 - 1)}{P_1 A_{eff}\gamma_1}}{\frac{h_2}{c_{p2}T_2} + \frac{\gamma_2 - 1}{2}}\right)} - (1+\gamma_1 M_1^2) - \frac{D}{P_1 A_{eff}} \tag{2.11}$$

Now the drag term, D, must be calculated using the baffle specific geometry and assuming the drag mainly contributes to the flow between the shock system on the projectile body and the thermally chocked plane, referred to as the high pressure region.

$$D = \frac{1}{2} c_d \rho_1 A_{p,b} \eta_c \mid u_1 - u_2 \mid (u_1 - u_2) \tag{2.12}$$

The area term, $A_{p,b}$, corresponds to the projected area of the baffles perpendicular to the flow and n_c accounts for the number of baffles in the region of interest. These two terms describe the total baffle area the high pressure region is exposed to in steady-state. From CFD [6] it has been shown that n_c is approximately 6, however more CFD was required to validate this number. Lastly, the velocity term corresponds to the velocity of the high pressure region in the laboratory reference frame, referred to as v_{lab}. The density terms, for simplicity, is taken from the inlet flow properties. Any discrepancies in the model are assumed to be adjusted with the drag coefficient. In Fig. 2.7, the non-dimensional thrust equation with the drag model incorporated is showed as a function of projectile Mach number at various drag coefficients and Q = 12.

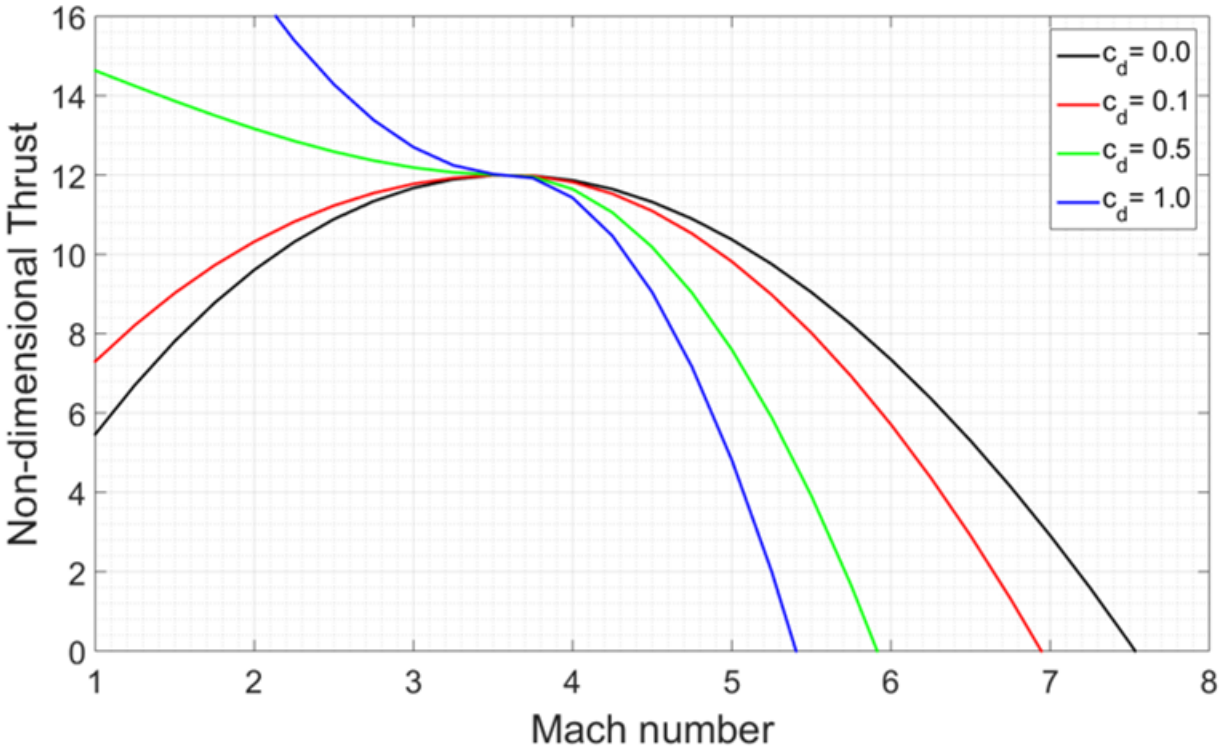

Figure 2.7: BTRA model with drag (Q = 12) at various drag coefficients

At low Mach numbers the model predicts higher thrust performance while at higher Mach numbers this is the opposite. The features are directly caused by the velocity in the drag term changing sign. At low Mach numbers v_{lab} is negative which causes the BTRA to experience negative drag. This is when the projectile velocity is slower then the acoustic velocity of the thermally choked plane. In this scenario the flow inside the high pressure region is moving in the opposite direction of the projectile. The switch in flow direction occurs at the peak thrust Mach number where $v_{lab} \approx 0$. The last thing to note is the model collapses to back to the SBRA performance model when the drag terms is zero.

2.4.1 Constant Area Heat Addition

When calculating the baffle drag the velocity of the high pressure region in the laboratory frame must be determined. This includes the incoming flow velocity and outgoing flow

velocity. The incoming flow speed, u_1 is already a known quantity while the outgoing flow velocity, u_2 is unknown. Assuming the outgoing flow is thermally choked ($u_2 = a_2$) the velocity is proportional to the flow temperature and equals $a_2 = \sqrt{\gamma_2 R_2 T_2}$. Following the thermally choked assumption the outgoing flow temperature can be estimated with constant area heat addition.

The total temperature of a constant area flow post heat addition is defined as:

$$T_{t2} = T_{t1} + \frac{\Delta q}{c_p}$$

Using the definition of total temperature for a isentropic procress

$$\frac{T_t}{T} = 1 + \frac{\gamma - 1}{2} M_1^2$$

and the definition of non-dimensional heat release, the ratio of total temperatures was determined.

$$\frac{T_{t2}}{T_{t2}} = \frac{1 + \frac{\gamma-1}{2} M_1^2 + Q}{1 + \frac{\gamma-1}{2} M_1^2} \tag{2.13}$$

Finally the definition of total temperature for an isentropic process was used again to find T_2 assuming $M_2 = 1$.

2.5 Friction-Based Drag and Combustion Efficiency

When comparing the initial BTRA performance model to experimental data, it over-predicted the non-dimensional thrust by a 30 to 50%. In Chapter 4 the theory and data will be compared in detail. The discrepancy suggested the initial model did not effectively describe the physics at work in the BTRA. As a way to better understand how the BTRA operation differs from the SBRA, an experimentally-driven model was developed. The model required a theoretical performance curve and experimental data correlation to determine empirical constants. In the end the aspect ratio of the control volume became the single empirical constant the model depended on. In this section an alternate drag model and a baffle influenced combustion efficiency will be presented as well as the effects of the aspect ratio.

2.5.1 Friction Based Drag Model

In 2005 Tangauy and Higgins [7] investigated the effect of friction on 1-D detonation waves. They concluded that the friction on a detonation wave produces a non-negligible work input to the control volume even if it is formally inconsistent with the 1-D formulation. This was argued from a physical point of view and with Galilean transformations from the laboratory reference frame to the detonation wave reference frame. If the ram accelerator is analogous to a quasi-detonation [2] than the same principle can be applied to the drag effects of the baffled-tube ram accelerator.

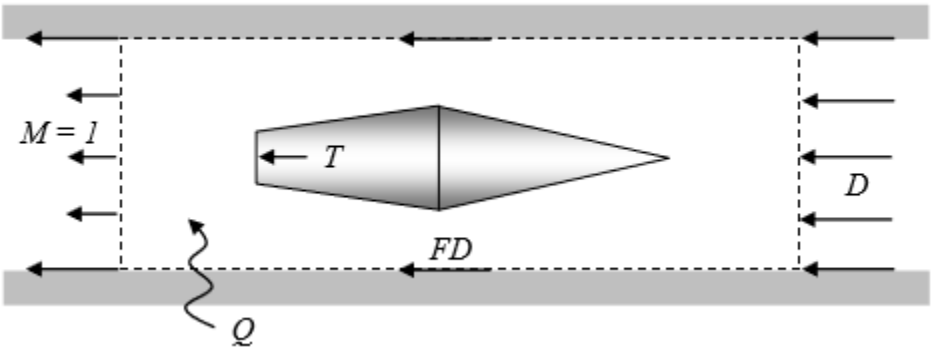

Figure 2.8: Ram accelerator control volume with frictional work inclusion

In Fig. 2.8 a control volume is set up for the formulation of the conservation equations. The projectile applies an equal but opposite thrust and the bore wall applies a friction shear stress to the control volume. Since the velocity between the control volume and tube wall is non-zero the friction applies work to the control volume at the wall velocity. This is not the case for the thrust since the projectile and control volume move a the same velocity.The term D is the inlet velocity which can also be considered as u_1. Conservation of momentum worked out to be:

$$P_1 A_b + \rho_1 u_1^2 A_b + F + \Psi L \pi d = P_2 A_b + \rho_2 u_2^2 A_b \tag{2.14}$$

As to not abuse notation the shear stress F in Fig. 2.8 is denoted as Ψ and thrust is denoted

by F. Then formulating the conservation of energy equation resulted in:

$$\rho_1 u_1 A_b[h_1 + \frac{u_1^2}{2} + \Delta q] + \Psi L \pi d u_1 = \rho_2 u_2 A_b[h_2 + \frac{u_2^2}{2}] \tag{2.15}$$

L is the length of the control volume while d is the diameter. Ψ is the shear force between the wall and control volume, which is taken to be proportional to the square of the relative velocity between the flow and the wall (Eq. 2.16). Applying the thermally choked assumption sets the exit velocity to the local acoustic velocity. However, this approach does not give any indication of the flow velocity so the average of the incoming flow and outgoing flow is used but the information of flow direction is maintained.

$$\Psi = \frac{1}{2} c_f \rho_1 \mid \frac{u_1 - a_2}{2} \mid (\frac{u_1 - a_2}{2}) \tag{2.16}$$

The transformation from baffle drag, which is caused by obstacles perpendicular to the flow, to friction drag is done with the friction coefficient, c_f. It is estimated by evenly distributing the projected baffle area on the area between the baffles. The following expression was the result:

$$c_f = c_d \frac{A_p}{A_w}$$

A_p is the projected baffle area and A_W is the surface area between each baffle. The drag coefficient, c_d, is experimentally determined.

Solving Eq. 2.14, Eq. 2.15 and the continuity equation similarly to Section 2.1 results in a non-dimensional thrust equation which depends on the projectile Mach number, non-dimensional heat release, and the ratio of control volume length to diameter.

$$\frac{F}{P_1 A_b} = M_1 \frac{\gamma_1}{\gamma_2}(1+\gamma_2)\sqrt{\frac{\gamma_2 - 1}{\gamma_1 - 1}\left(\frac{Q + \frac{h_1}{c_{p1}T_1} + \frac{\gamma_1 - 1}{2}M_1^2 + \frac{4\Psi(\gamma_1 - 1)}{P_1 \gamma_1}\frac{L}{D}}{\frac{h_2}{c_{p2}T_2} + \frac{\gamma_2 - 1}{2}}\right)} - (1 + \gamma_1 M_1^2) - \frac{4\Psi}{P_1}\frac{L}{D} \tag{2.17}$$

Fig. 2.9 illustrates the non-dimensional thrust as a function of Mach number for a TCRA with friction. The aspect ratio of the control volume is varied from 0 to 3, where an $\frac{L}{D} = 0$ indicates no drag. The result looks very similar to the initial BTRA performance model

when it varied drag coefficient. However, the advantage of the aspect ratio it is grounded in geometric constants.

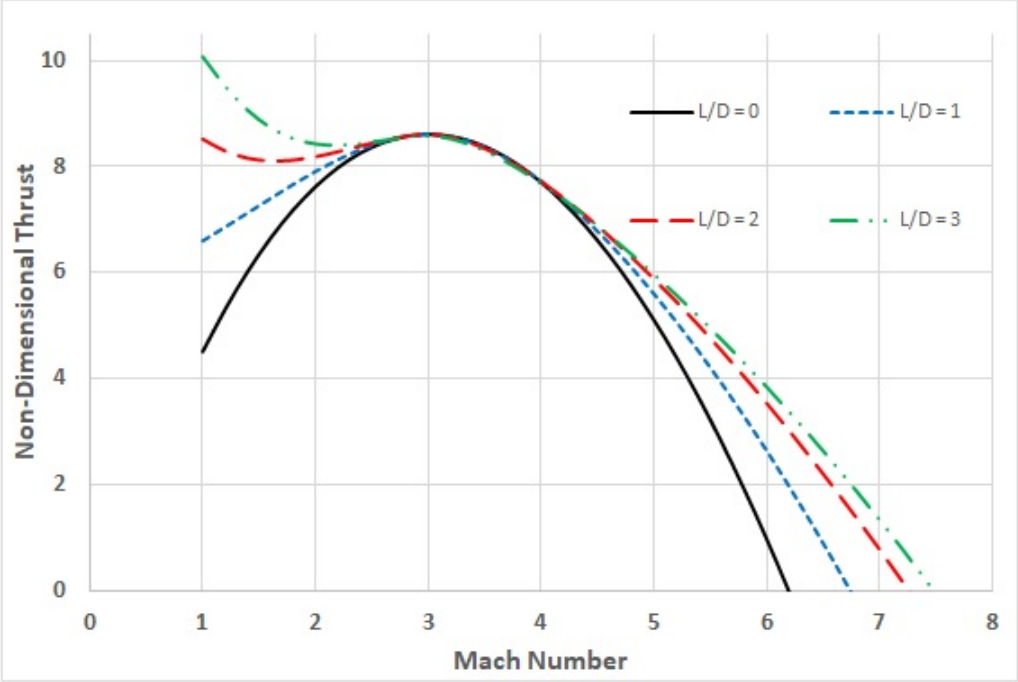

Figure 2.9: Non-dimensional thrust with the inclusion of friction (Q=10.8)

2.5.2 Combustion Efficiency

In the SBRA performance model the propellant reaction was always assumed to be complete. This was a valid assumption because their was no obstructions disrupting the combustion. In the smooth-bore ram accelerator the combustion stabilized at the base of the projectile, acting as a flameholder, and the thermally choked plane did not allow pressure relief. Furthermore, the heat release was such that the shock system was stable on the projectile body. On the other hand, inside the baffled-tube there are periodic disruptions to the flow field as well as a constantly surging shock system due to the higher heat release.

To quantify the resultant heat release inside the BTRA a combustion efficiency, η_q, was derived using dimensional analysis.

$$\eta_q = \frac{\dot{q}}{q}\tau$$

The $\frac{\dot{q}}{q}$ is the ratio of the propellant mixture heat release rate to total heat release, which acts as rate of reaction. The value τ is as a residence time meant to describe the time the reacting flow is in a single chamber defined by the baffles.

$$\tau = \frac{L_c}{v_{lab}}$$

The length of a baffled chamber is denoted by L_c and the flow velocity is estimated to be the difference between the incoming flow and outgoing flow velocities, v_{lab}.

$$\eta_q = \frac{\dot{q}}{q}\frac{L_c}{\mid v_{lab} \mid} \tag{2.18}$$

The combustion efficiency acts as a modification factor to the already established non-dimensional heat release. A range of 0 to 1 was imposed as well to keep it non-physical quantities of heat release from being produced. Since the BTRA control volume is defined to end at the thermally choked plane the length at which the combustion occurs, plays a role in determining the aspect ratio, $\frac{L}{d}$, for the drag model. In this scenario the control volume length would be defined from the shock system on the projectile to the quasi-steady thermally choked plane.

Figure 2.10 illustrates the effects of the combustion efficiency on the non-dimensional thrust. For this example a propellant mixture of $2.5CH_4 + 2O_2$ was used. In the plot the thrust at 100% combustion efficiency is depicted in black and the rest of the curves are variable values of $\frac{\dot{q}}{q}$. The actual value of $\frac{\dot{q}}{q}$ is determined uniquely for each mixture however for representative purposes the value was varied. With the combustion efficiency, low and high Mach numbers see a significant decrease in thrust. The velocity of the reacting flow, $v_{lab} = u_1 - a_2$, became large when $u_1 << a_2$ and $a_2 >> u_1$. The thermally choked plane temperature followed Eq. 2.13 as the projectile Mach number increased thus the local acoustic velocity, a_2 increased. Eventually $u_1 = a_2$ was where the thrust peaked but as Mach

number increases a_2 grew faster than u_1 creating a large v_{lab} in the opposite direction of the projectile. The absolute value of the reacting flow velocity in Eq. 2.18 was taken to keep the combustion efficiency from going negative.

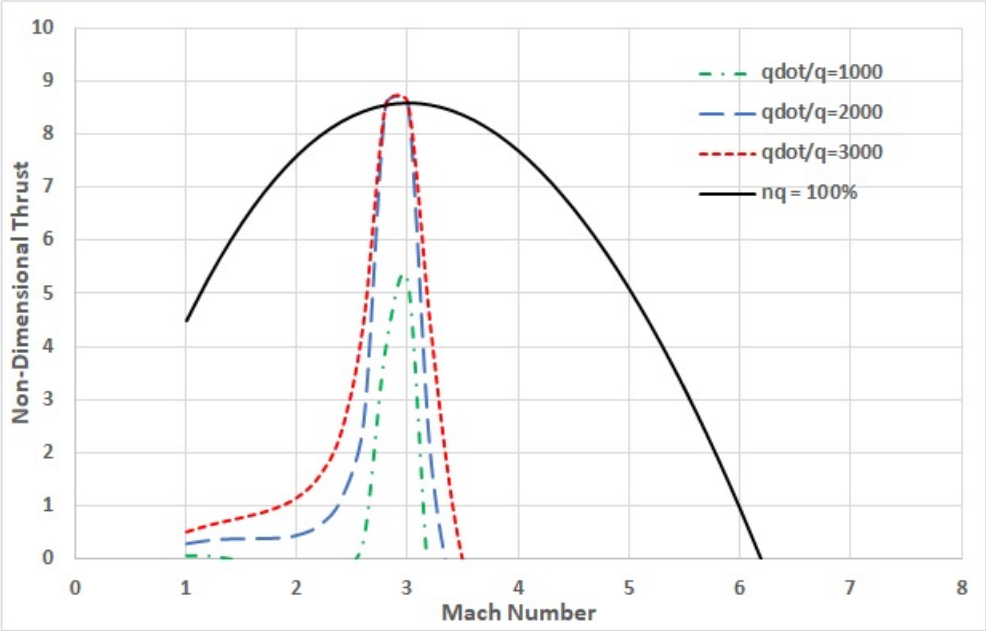

Figure 2.10: Combustion efficiency applied to the non-dimensional thrust equation (Q=10.8)

Chapter 3

EXPERIMENTAL APPARATUS AND METHODOLOGY

This chapter describes the ram accelerator facility, where all the data presented in subsequent chapters was collect, and the procedures followed to ensure reliable results. Specifically three types of tests were carried out all being BTRA shots with combustible propellants. The first used baffles normal to the direction of the projectile, the second used baffles slanted into the flow, and the third used baffles slanted outward from the flow. The laboratory components and procedures required to successfully run these tests and collect the data are presented in detail.

3.1 Experimental Facility

Composed of a light gas gun, 16 meter long tube with a 38 millimeter bore, and gas handling system; this facility is where all of the UW Ram Accelerator experiments have been conducted.

3.1.1 Experimental Set-up

The single-stage light gas gun utilized helium to accelerate the projectile to the requisite starting velocity to maintain supersonic flow through its throat. Two sets of aluminum diaphragms are used to contain the breech pressure. There is a small volume between the two diaphragm sets filled to a certain pressure to regulate the pressure difference across the most upstream diaphragm set. Each of these diaphragms was scored with an 'X' with a specific pressure to maintain a predictable peddle burst. Depending on the projectile mass the breech pressure can range from 28.9 to 37.9 MPa.

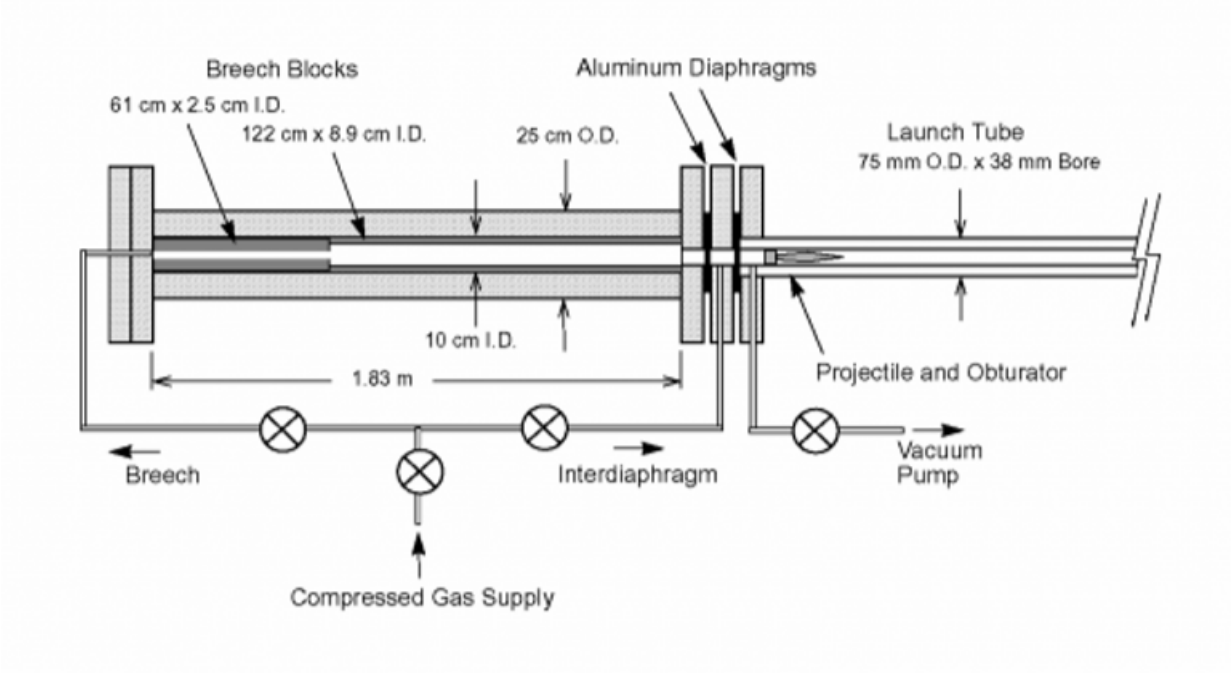

Figure 3.1: Single-stage light gas gun schematic

The entire test section of the ram accelerator totals 16 meters, which was parsed into 8 two meter long sections. Each two meter section had 5 equidistant instrumentation station. The tube has a 28 millimeter bore and 102 millimeter outer diameter. Each section can be removed or isolated using a thin Mylar diaphragm. This is done when a multistage experiment is conducted with different mixtures. Upon removal of a 2 meters section the system is equipped to integrate at BTRA test section in its place. The test section was designed to withstand fill pressures up to 5 MPa. A schematic of the system layout can be seen in Fig. 3.2 and a more detailed description of the system can be found in Ref. [8].

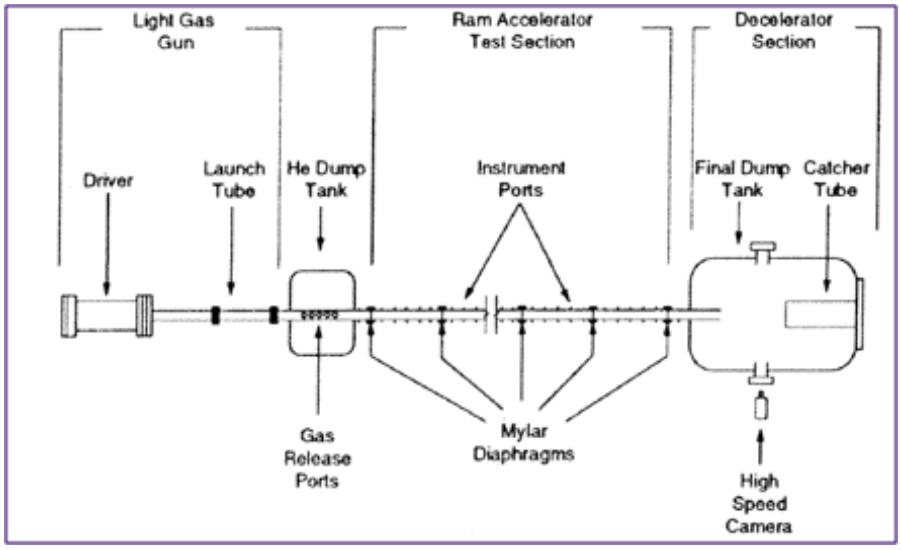

Figure 3.2: Schematic of the University of Washington ram accelerator

Each instrumentation station was designed to accommodate 2 to 4 equidistant instrumentation ports space circumferentially around the tube. The ports were designed specifically for standard piezoelectric pressure transducers. Electromagnetic sensors were designed in house [9] to also fit inside the instrumentation ports. Each station in a test section was outfitted with at least one electromagnetic (EM) sensor and one piezoelectric pressure (PCB) transducer. The data acquisition system utilized a National Instruments PXIc-1071 bus which collected data from the PCB and EM sensors at 1.25 MHz across 32 channels. The PCB sensors measured the pressure at the tube wall and pressure wave arrival times at a given station. The EM sensors measured the arrival time of a neodymium magnet on board the projectile at a given station.

3.1.2 Gas Handling

In Ref. [10], the gas handling capabilities of the ram accelerator facility are explain in detail. To summarize, the facility used Brooks Instrument Mass Flow Controllers (MFCs) to control molar ratios of fuel, oxidizer, and diluent. The gases were regulated and mixed inside the

tubing as they were led into the desired test section segment. Recently, a new procedure to calibrate the MFCs has been developed. The concept used the time derivative of the ideal gas equation.

$$\frac{d}{dt}(PV = nR_uT)$$

Where V was the volume of the test section being filled, T was the gas temperature, P was the fill pressure, n was the molar count, and R_u was the universal gas constant. The volume, temperature, and universal gas constant were assumed to be unchanged. Reorganizing the above equation resulted in a proportionality of the molar flow rate and fill pressure rate:

$$\frac{dn}{dt} = \frac{dP}{dt}(\frac{V}{R_uT}) \tag{3.1}$$

Calibrations were performed in one of the 2-meter long sections which was isolated from the rest of the system with diaphragms. The volume was pressurized and LabView monitored the pressure while calculating the $\frac{dP}{dt}$ for a given MFC flow percentage,or set point. A propellant mixture molar ratios required specific $\frac{dP}{dt}$, which was correlated to the MFC set point. The calibration points were linearly interpolated or extrapolated to calculated the set point required for a given molar ratio.

3.2 Baffled-Tube Designs

Two different baffled-tube designed have been installed and tested in the ram accelerator. The first were an annular ring design where the baffles were directly normal to the projectile direction, they were referred to as the normal baffles. The second were a set of baffles slanted by 31° with respect to the tube axis. The purpose of both were to act as a one way valve to permit the use of higher energy propellants which result in higher combustion pressures. The normal BT design included structural analysis to ensure the they would not fail during experimentation. The lessons learned from the normal baffles lent to the design of the slanted baffles.

3.2.1 Normal Baffles

The normal baffles were made up of a series of joined inserts (Fig. 3.3) which were housed inside an outer shell which replaced a 2 meter segment in the ram acceleration test section. The use of inserts allowed new geometries to be tested, aided in manufacturing costs, and allowed damaged inserts to be replaced with ease. The design focus of baffle inserts aimed to maximize void space while structural integrity was maintained. Maximized void space space was motivated by an attempt to maximize the systems performance by increasing the available propellant. Since the inserts would be exposed to high combustion pressures an AISI-4141 carbon steel hardened to RC 32-36 was chosen to handle the subsequent stresses.

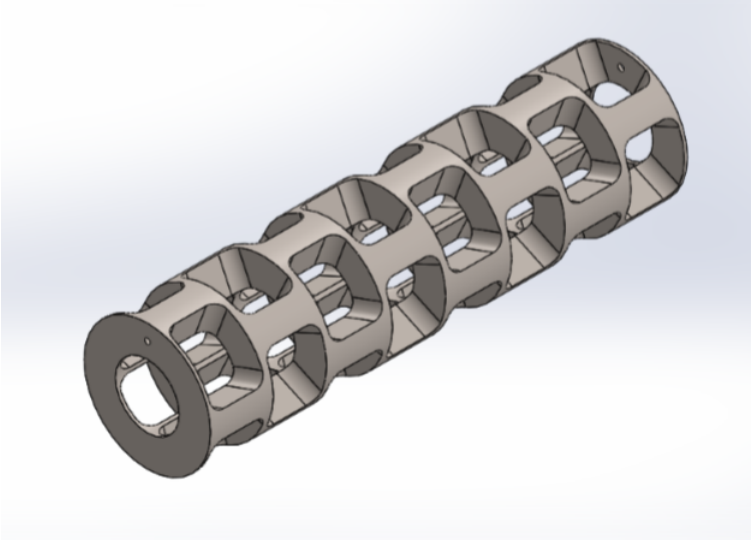

Figure 3.3: 3D CAD model of normal BT insert

Before production began on the baffle inserts, a design study to determine the orientation of the longitudinal rail supports between the baffles was complete. The work was down by Lucas Heflin and more on the subject can be found in Reference [11]. The longitudinal rails served two functions: keep the axisymmetric projectile from canting and provide structural reinforcement to the baffles in the flow-wise direction. The structural integrity of linear an offset rails were studied using ANSYS static structural analysis (Fig. 3.4). With 14

MPa loaded to one side of the baffle, the offset rail design displayed a 250% decrease in equivalent stress compared to the linear rail design. However, the offset design showed signs of longitudinal deformation and seemed to be susceptible to compressive forces. In contrast, the linear rail design showed a resistance to longitudinal deformation. The compressive forces were assumed to be minimal so the offset rail design was chosen.

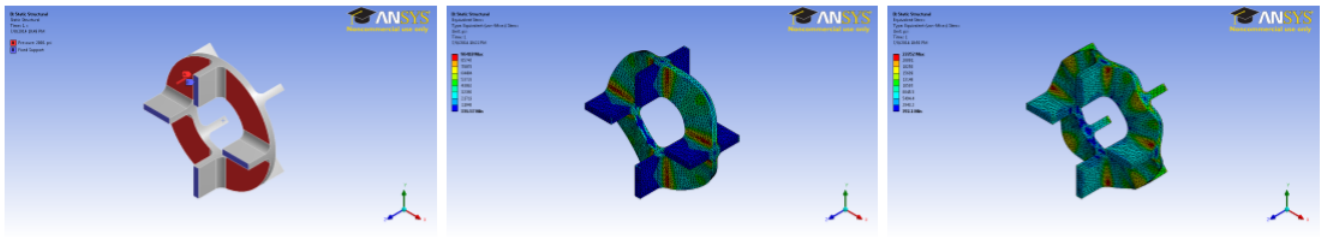

(a) FEA load conditions (b) Linear rail setup (c) 45° offset rail setup

Figure 3.4: ANSYS structural analysis on varying rail orientations

In addition, the cross section of the rail was studied in ANSYS to maximize the void space and minimize stress concentrations. Under consideration were linear rails, pie cut rails, 20° tapered rails, and exponential power-law rails (Fig. 3.5). With the same loading condition as the analysis describe above the tapered rail resulted in nearly half the stress concentration while slightly reducing the void volume. In the end, the tapered rails were chosen with the offset orientation.

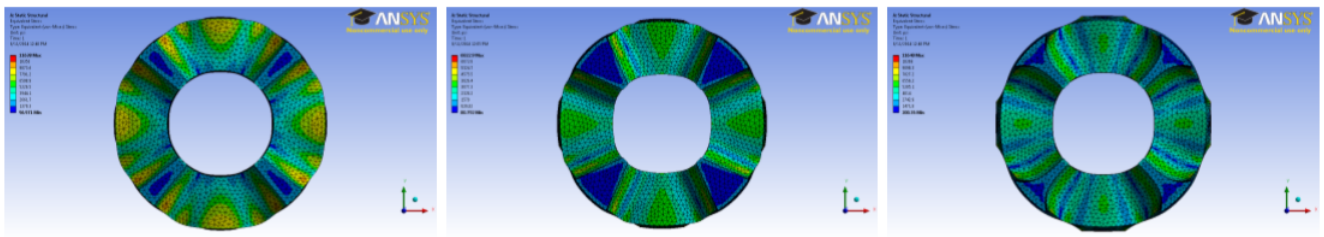

(a) Pie Rail (b) Tapered Rail (c) Power-Law Rail

Figure 3.5: ANSYS structural analysis on varying rail cross sections

A total of 112 chambers over four meters was manufactured and the final design of the insert had eight baffle chambers (Fig. 3.3). However, the initial testing of the baffled-tube inserts resulted in a buckling failure. After successive tests a projectile lodged its self in the insert (Fig. 3.6). Upon inspection is was deduced that the rapid testing caused the inserts to compressively yield and a localized failure was found near the region of peak stress according to the FEA [12]. It was concluded that the axial load on the baffles and therefore the compressive forces were greater than expected.

Figure 3.6: Yielded insert with local failure; Broken and lodged projectile

To address the initial failure the insert configuration was changed. Rather than seven 8-chambered inserts; seven 6-chambered inserts and one 7-chambered insert was used. Never the less, the lack of structural reliability did not allow for higher than the nominal pressure, 1.5 MPa, experiments in the BTRA to be conducted. Motivated by a CFD study to optimize performance with different baffle geometries and the investigation of high pressure BTRA performance the slanted baffles were designed.

3.2.2 Slanted Baffles

Attempting to open up the BTRA performance envelope further and realize the thrust predicted by the initial BTRA performance model, a CFD study by Navid Daneshvaran [13, 14] was conducted. The transient CFD simulations with reactive mixtures using FLUENT first investigated 45° outward slanted baffles (case 1), 45° inward slanted baffles (case 2), and the original normal baffles (case 3). Shown in Fig. 3.7 are temperature contours of the baffle configuration cases run with stoichiometric methane-oxygen and a fill pressure of 5 MPa.

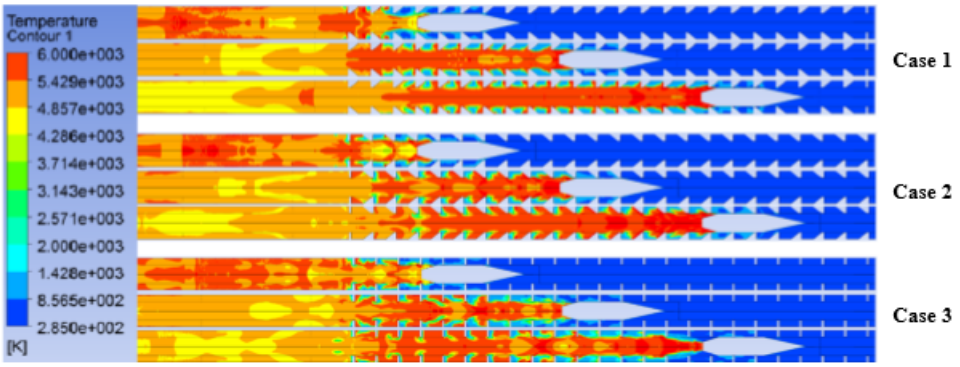

Figure 3.7: Static temperature contours at M = 4 for case 1-3 baffle configurations

The temperature contours show that the combustion intensity in case 1 and 2 are much higher suggesting the slanted baffles would perform better than the normal baffles. This conclusion was propped up by the thrust profiles in Fig. 3.8. After the entrance transients subside the inward slanted baffles were shown to produce the highest average thrust. In Chapter 5 the inward and outward slanted baffles will be experimentally compared.

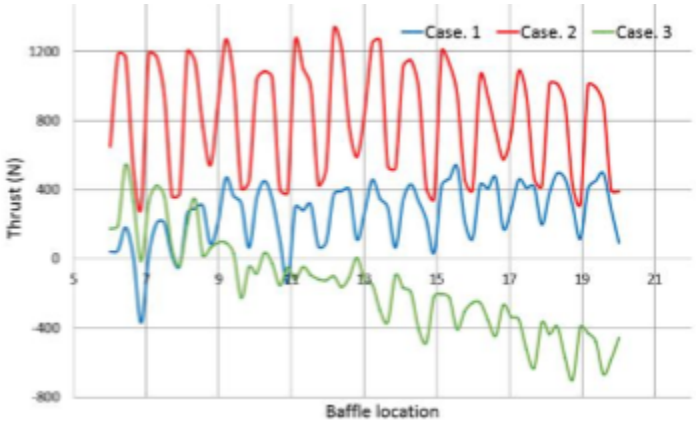

Figure 3.8: Thrust profile of cases 1-3 at M = 4

With the understanding that the inward slanted baffles performed best, a study of optimal slant angle, with respect to the axial direction, was conducted. Only two angles were considered, 45° (case 2) and 23° (case 4). Case 5 used the slant angle of 23° but the projectile tail was lengthened and body shortened. From the temperature contours (Fig. 3.9) the combustion intensity in case 4 and 5 seemed to be the more than case 2, indicating better performance. The thrust profiles (Fig. 3.10 correlated with this indication showing case 4 and 5 having the higher average thrust. A more detailed look into the CFD study can be found in Ref. [13].

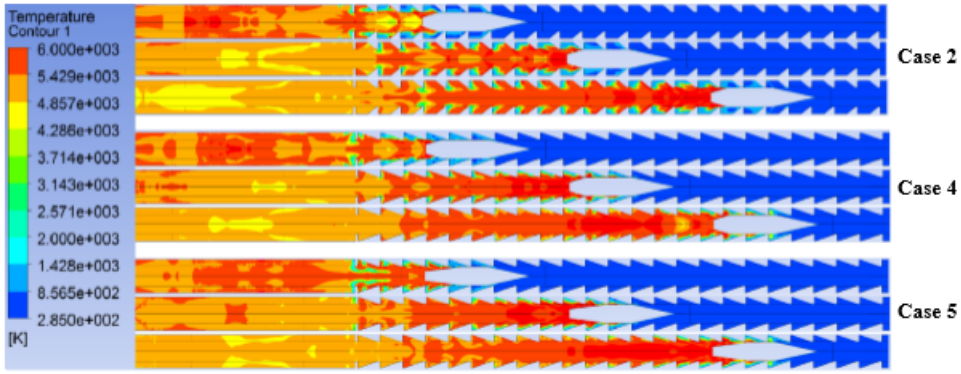

Figure 3.9: Static temperature contours of cases 2,4, and 5 at M = 4

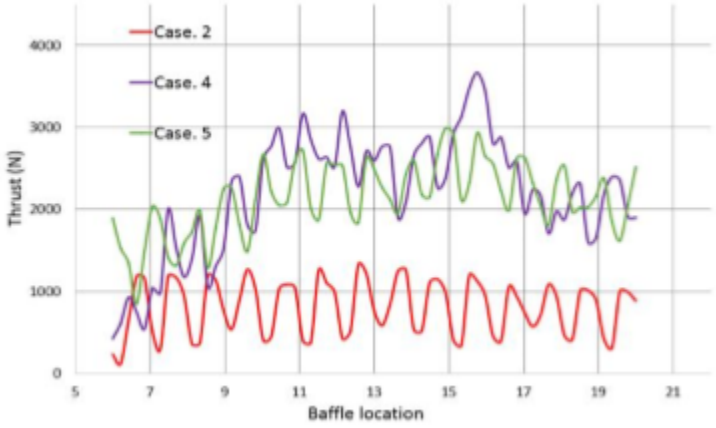

Figure 3.10: Thrust profile of case 2,4 and 5 at M = 4

Based off the CFD results and machining considerations 31° inward slanted baffles were designed. They were manufactured out of 17-4PH stainless steel with a H-1075 heat treatment. Instead of multi-chambered inserts each baffled chamber was an individual insert (Fig 3.11, top left). Each insert was attached to the next with steel bolts forming a single 2 meter long insert (Fig 3.11, top right). In total 52 of the individual inserts were used to complete the 2 meter test section.

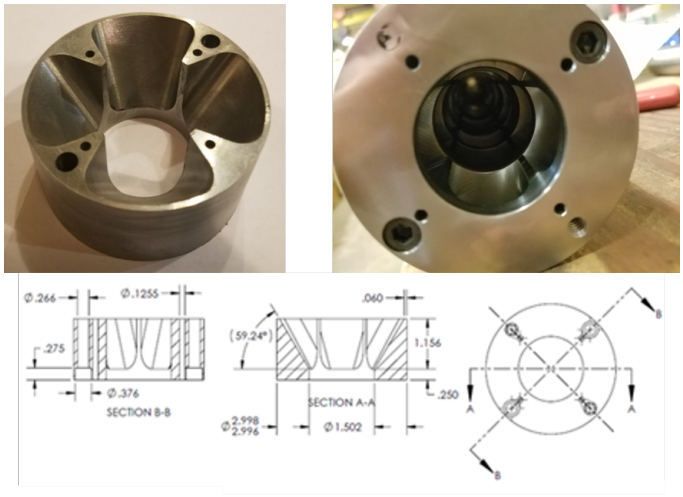

Figure 3.11: Photo of slanted baffle chamber insert and machine drawing

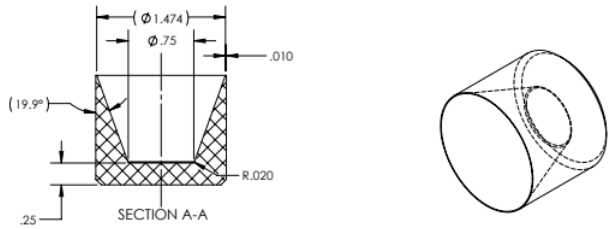

Figure 3.12: Technical drawing of the obturator used in BTRA experiments

3.3 Projectile Configurations

For the BTRA experiments presented in this paper two projectile types were used: finned and axisymmetric. Each projectile utilized a sabot (Fig. 3.12), with an 1.496" OD and 1.25" in length, of in-house design referred to as the obturator. The mass of the obturator ranged from 21 - 25 gm. The obturator is essentially to establishing the shock system on the projectile body at the entrance of the propellant. An in-depth analysis of the transient behavior of ram accelerator ignition and the importance of the obturator can be found in Reference [15].

The finned projectiles were made from an aluminum body and titanium nose cone. They were used in experiments with a normal BTRA and SBRA transition. The fins were important for these experiments because the SBRA requires fins to keep the projectile stable. The rails on the baffles perform the same task in the BTRA. The axisymmetric projectiles were used in the remaining experiments and were made from polycarbonate. A one piece and two piece configurations where used. Specifically, in the slanted baffle experiments the diameter of the projectile throat was reduced creating more variations.

3.3.1 Polycarbonate Projectiles

The one piece and two-piece polycarbonate axisymmetric projectile configurations are depicted in Fig. 3.13. The one piece projectile used a cavity in the tail 1.75" deep and tapped

to 1/2"-13 to store a 0.25" long neodymium plug magnet. This allowed the EM sensors to track the projectile. The remainder of the cavity was filled with a threaded plastic stud. The two-piece projectile used an annular neodymium magnet which was 0.125" long with 1.25" OD X 0.75" ID. The magnet was housed in a cavity of the same dimensions, with a slip fit, at the joint between the two pieces. The nose cone and body were held together with a piece of plastic all-thread fastened inside tapped cavities on both pieces.

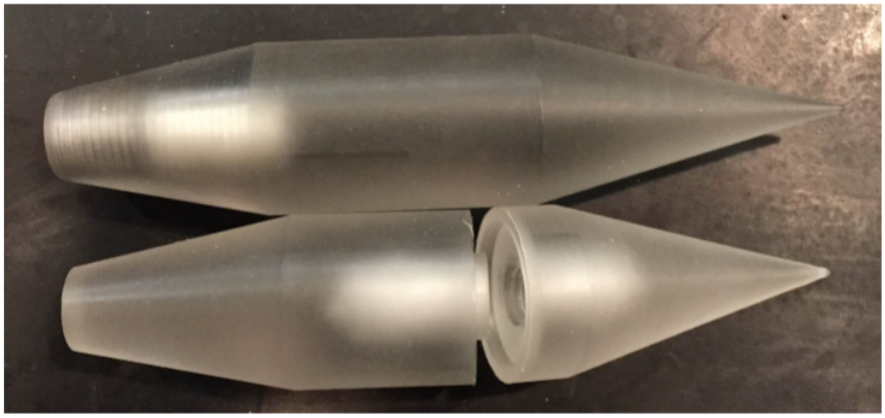

Figure 3.13: One and two piece polycarbonate projectile

Once assembled the two projectile configurations had the same dimensions (Fig. 3.14). The length of the projectiles were 6.751" with the throat diameter being 1.485". The nose cone had a half angle of 15° and made up 2.771" of the total length. The boat tail angle was 12° and made up 1.823" of the total length. That leaves 2.157" for the throat of the projectile. This was important because for the baffles to operate as theorized, as a one way valve, the throat of the projectile needed to be at least 1.5 times the length of a baffle chamber. The nominal mass of this type of projectile was approximately 146 g.

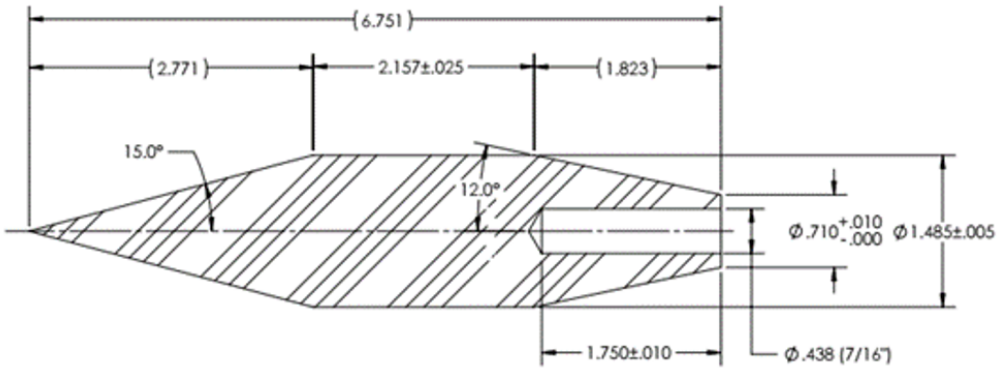

Figure 3.14: Machine drawing for one-piece axisymmetric polycarbonate projectile

During the slanted BTRA tests the throat diameter of the polycarbonate axisymmetric projectiles was reduced. Starting at 1.485" it was reduced all the way to 1.320". The results of these tests can be seen in Chapter 5. In the end a nominal throat diameter of 1.420" was chosen for the slanted BTRA tests.

3.3.2 Finned Projectile

The finned projectile is illustrated in Fig. 3.15. It was designed as a two piece finned projectile separated into nose cone and body (Fig. 3.16). The titanium alloy nose cone was threaded to 7/8"-20 at the base and hollow. The 6061-T6 aluminum alloy finned body began as an entire finned projectile that was modified. To attach the two halves the aluminum alloy finned projectile had its nose cone machine off and a cavity was bored out. A counter bore was machined into the cavity and tapped to accommodate the threads of the titanium nose cone. The rest of the cavity was tapped to 1/2"-13 to house a 0.25" long neodymium plug magnet and plastic all-thread stud. The composite metal aluminum projectile, after assembly, had 1.14" throat diameter and a nose cone angle of 10°. The length of the fins which act as the throat of the projectile were about 3" long which covers roughly 2 baffle chamber lengths. The tail is tapered by 3.6°.

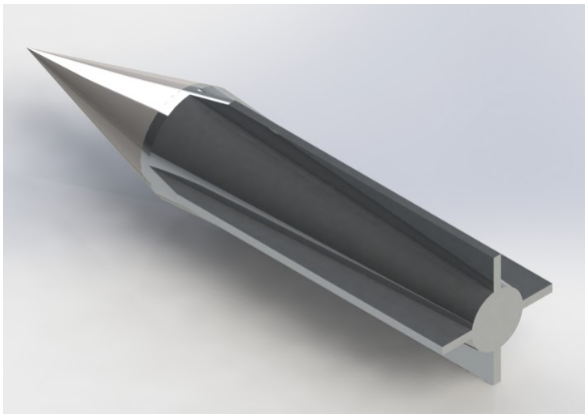

Figure 3.15: 3D rendering of two-piece finned projectile

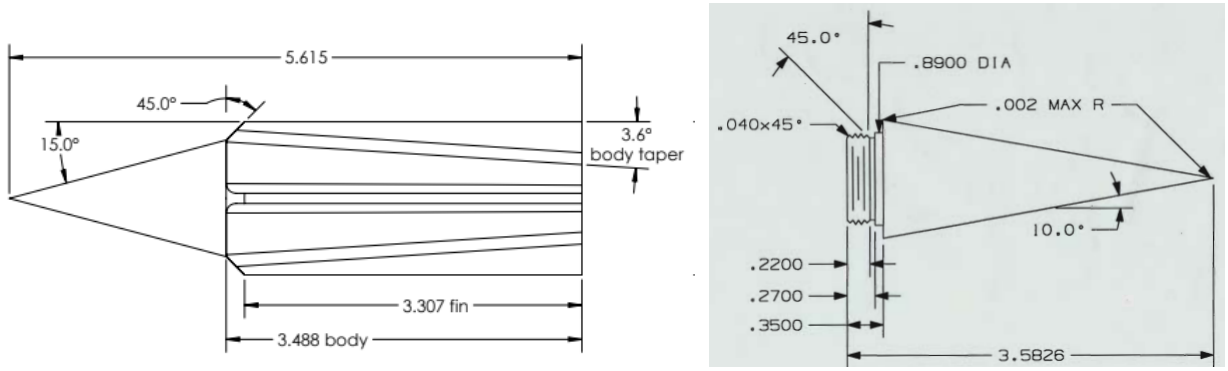

Figure 3.16: Whole aluminum alloy finned projectile (top), Titanium alloy hollow nose cone (bottom)

3.4 BTRA Experimental Procedure

The procedure when conduction BTRA experiments required special attention since high pressure gas, combustible and inert, were in use. The first step was preparation the projectile and obturator. The projectile was loaded with a neodymium magnets, whether it be plug or annular shaped, and sealed using a plastic all-thread plug. The individual mass of the equipped projectile and obturator were recorded along with the projectile technical drawing title. The projectile was then attached with a drop of adhesive concentrically to the obtura-

tor then the total mass was recorded. The combination was then loaded into the launch tube downstream of the light gas gun. From the mass of the projectile and requisite entrance velocity the breech pressure was determined. From the breech pressure, the aluminum diaphragm configuration and inner-diaphragm pressure was determined. The diaphragm configuration consists of thickness of diaphragms, score pressure, and number of diaphragms. Before the gas gun was sealed the requisite diaphragm configuration was recorded and loaded into th system. At the rear of the gas gun a viscous damper was attached to absorb recoil from the launch.

Next, 0.014" thick Mylar diaphragms are used to isolate the test section from the rest of the system when it was pulled down to vacuum. The section downstream of the test section was either held at vacuum or pressured with inert gases to decelerate the projectile. The catcher tube at the end of the system was packed with a dense carpet roll, bookend with aluminum sheet metal, and a steel block to absorb any excess kinetic energy. With the test section isolated, it was pressure checked with N_2 to confirm propellant at pressure during the experiment will be held. Before the experiment the electrical continuity was confirmed across the instrumentation suite and the data acquisition triggering mechanism was test. This involves plugging an external EM sensor into the data system and swiping a magnet across it to confirm the system will trigger once the projectile passes the first sensor.

Then two vacuum pumps are used evacuate the entire system, excluding the light gas gun, down to less then 1 Torr of pressure. Once down to an adequate vacuum level the pumps are isolated, turned off, and the test section propellant filling procedure begins. Four different propellant mixture classes were used for the data presented in Chapter 5: methane-oxygen, methane-air, methane-nitrous oxide, and methane-oxygen-carbon dioxide. Methane chosen as the fuel because it has the highest heat of combustion of any hydrocarbon at 55.7 kJ/g. Hydrogen has the highest of any fuel but due to its acoustic speed (1270 m/s) obtaining Mach numbers to initial starting conditions was difficult with a light gas gun alone. The non-dimensional heat releases, Q, of all the mixture classes ranged from 5.87 to 12.8 and the sound speeds ranged from 302.4 to 393.3 m/s.

For the methane-oxygen mixtures an equivalence ratio, ϕ, range of 2.5 to 4 was used. The gauge fill pressure of the mixtures ranged from 1.03 to 1.9 MPa. The methane-air mixture used was stoichiometric, $\phi = 1$, and a fill pressure range of 1.03 to 1.4 MPa. The methane-nitrous oxide mixture had a $\phi = 2$ and a fill pressure range of 0.93 to 1.4 MPa. To create the methane-oxygen-carbon dioxide mixture stoichiometric methane-oxygen was diluted with 2 moles of carbon dioxide. Its fill pressure ranged from 0.93 MPa to 2.10 MPa.

After filling the test section with the requisite propellant mixture the light gas gun operation begins. In preparation to shot, the gas gun was filled to the bottle pressure of the source helium bottles. Special care was taken to slowly fill the inner-diaphragm volume as well so the most up stream diaphragm set was not exposed to a failure inducing pressure difference. With the breech, inner-diaphragm volume, and helium bottles equalized the inner-diaphragm volume was isolate. The light gas pump was energized and the helium pumping process begins. As the breech raised in pressure the inner diaphragm was periodically equalized with the breech until it reaches its requisite pressure. If a specific entrance velocity was preferred, once the breech reaches its prescribed pressure the inner-diaphragm volume was exposed to the breech pressure rapidly pressurizing it and breaking the diaphragm set between it and the launch tube. Subsequently, the most upstream diaphragm set burst due to the rapid expansion in the inner-diaphragm volume releasing the remained pressurized helium, this was referred to as a hand-break. Otherwise, the breech is allow to pressurize until the most upstream diaphragm breaks on its own. This was referred to as a pump-break.

Upon launch the projectile passes the first EM sensor triggering the data acquisition system to save data the occurs within a specified time spanned. Since a typical experiment with a successful start occurs within a 20 ms time frame a reliable trigger was essential. The rest of the EM sensors track the projectile down the launch tube, test section, and deceleration section. The PCB sensors complete the same task but for pressure waves and shock systems. For a successful start, the shock systems and projectile position coincide. The post shot data analysis of the BTRA experiments will be covered in the proceeding chapter.

Chapter 4
DATA ANALYSIS

In this chapter the collection and processing techniques of the raw experimental data will be discussed as well as the procedure to analyze the data. The collection of the raw data introduces uncertainties due to signal distortion, delay, and sample rate limits inherent in the data acquisition system. The processing of raw data introduces uncertainty also due to the techniques used to present the data for analysis. Once processed the data is analyzed with qualitative and quantitative techniques.

4.1 Collection and Processing of Raw Experimental Data

In the ram accelerator facility the data for a given ram accelerator experiment was collected with EM and PCB sensors across 32 channels at 1.25 MHz. The EM sensor records the arrival time and magnitude of the induced voltage of the projectile. The PCB records arrival time and magnitude of pressure waves. The EM sensor signals were concatenated into six strings and amplified using multiplexers. Each PCB sensor signal is individually amplified. On arrival to the National Instruments PXIc-1071 data acquisition system LabVIEW organizes the signals into a readable .lvm file. A MATLAB script were developed to read this .lvm file, plot the pressure signals at each instrumentation station and plot the concatenated EM signals from the multiplexers.

From the plotted magnitude-time data and known instrumentation station position kinematics can be applied. The velocity and acceleration of the projectile and pressure waves were determined at all stations. Since the station positions were known the velocity data was used to create velocity-distance diagrams. The magnitude-time plots from the pressure data were also used qualitatively to determine if an unstart, wave fall-off, or successful oper-

ation occurred at a given point in the test section. Furthermore the time and distance data from both sensors can be used to construct time-distance (t-x) diaphragm to determine the relative position of the shock system to the projectile.

4.1.1 Data Collection Uncertainty

When collecting data in the ram accelerator facility the following uncertainties arises: non-uniform station separation distance, digitization of analog signal due to a finite sample rate, signal distortion, and delays. The maximum relative uncertainty in knowing the distance between each instrumentation station is 0.5%. The finite sample rate of 1.25 MHz introduces a maximum uncertainty of 0.4 μs in time of arrival. The signal distortion an delay were not as easily quantified.

The signal distortion was the largest contributer to uncertainty. In Fig. 4.1 depicts the output of four EM sensors 90° apart at a single station. The vertical scale was 500 mV/div and the horizontal scale had 20 μs intervals. Each signal was presented with a individual voltage range. Typically the time of arrival of the magnet was found from the intersection of the signal and zero voltage line. From the top trace to bottom the projectile time of arrivals were 4.138, 4.137, 4.137, and 4.136 ms. Assuming this was the typically distortion of a signal the maximum uncertainty for arrival time was 2 μs, this includes the uncertainty due to a 1.25 MHz sample rate. Finally, the uncertainty to signal delay was most prevalent in the EM sensors. The case of the EM probes were 316 stainless steel which was electrically conductive. The casing of the probe causes diffusion of the magnetic field thus resulting in a phase shift. However if this was assumed to occur in equal amounts at each EM sensor the shift was negligible.

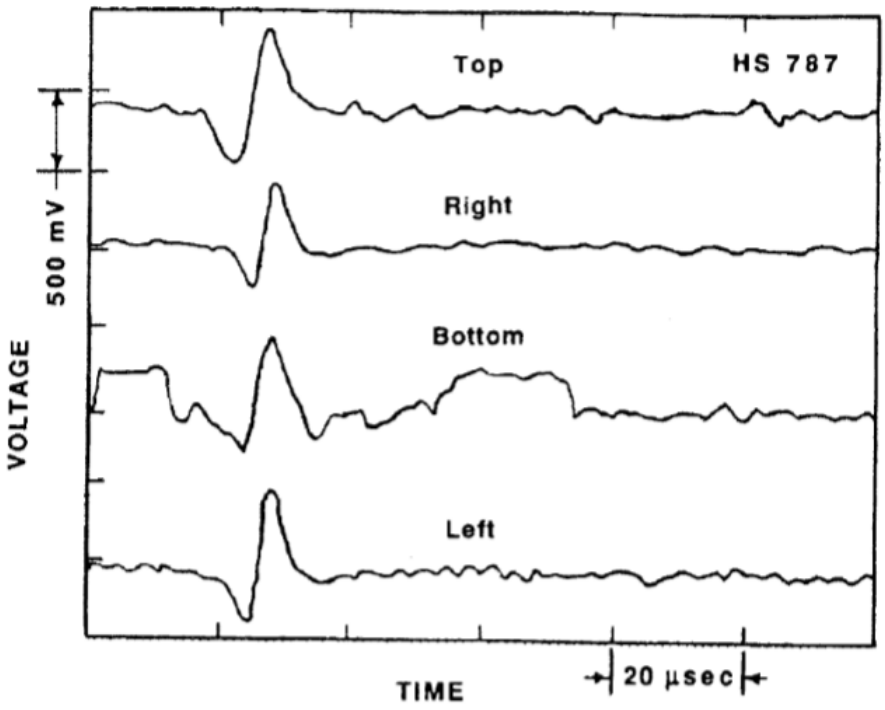

Figure 4.1: Experimental data from EM sensors 90° apart at a single station [1]

4.1.2 Data Processing Uncertainty

Determining the velocity and acceleration requires the arrival times at two stations and the distance between them. Each of the time of arrival data point had an associated 2 μs as mention above. The overall uncertainty in transit time (Δt) between the station became 4 μs. In addition, the relative uncertainty of the distance between station has already been stated at 0.5%. The linear relationship for the relative uncertainty of the experimentally determined mean projectile velocity ($\bar{u}$) at a given station was:

$$\frac{\Delta u_{EM}}{\bar{u}} = \frac{\Delta x}{\bar{x}} + \frac{\Delta t}{\bar{x}}\bar{u} \tag{4.1}$$

where $\frac{\Delta x}{\bar{x}}$ is the relative uncertainty of the station separation distance.

The calculation of mean experimental velocity under-predicted the actual projectile velocity if the projectile was accelerating. Another consideration was how much uncertainty

was introduced when ignoring the projectile acceleration between the two stations. The magnitude of the relative velocity error was as follows:

$$\frac{\Delta u_{\ddot{x}}}{\bar{u}} = \sqrt{1 + \left(\frac{\ddot{x}_o \bar{x}}{2\bar{u}^2}\right)^2} - 1 \tag{4.2}$$

where $\ddot{x}_o$ was the mean acceleration between the stations. The combination of Eq. 4.1 and 4.2 was the total uncertainty for the calculation of the mean velocity between two stations. Assuming a steady acceleration of $\ddot{x}_o = 50,000$ and a uniform station separation distance of $\bar{x} = 40$ centimeters Eq. 4.1 and 4.2 were plotted in Fig. 4.2 as function of mean projectile velocity.

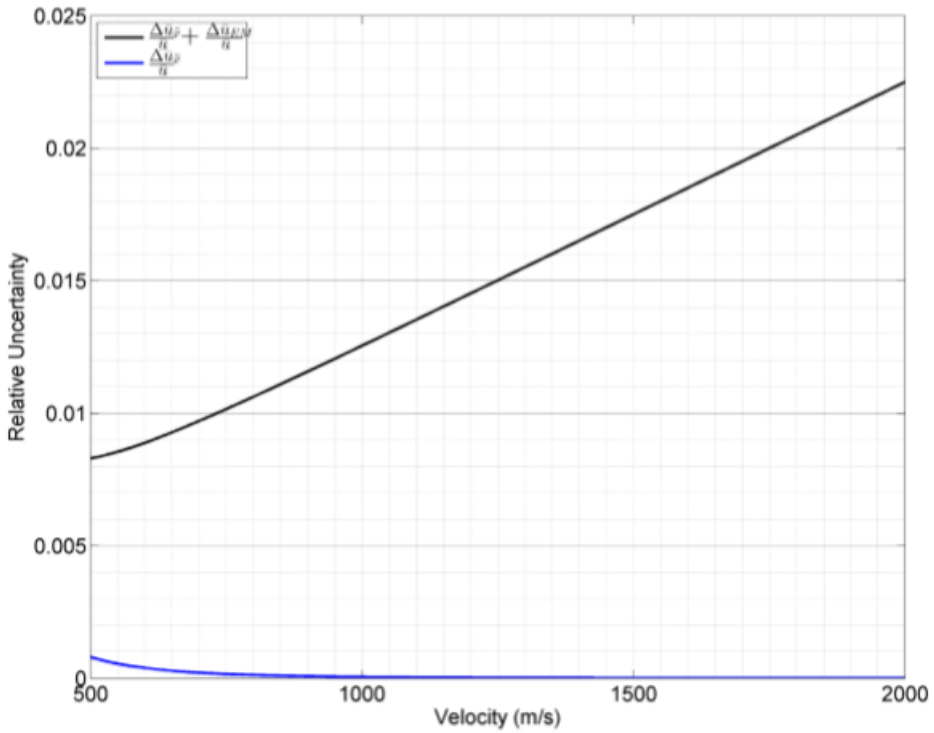

Figure 4.2: Relative uncertainty for mean projectile velocity and acceleration between instrumentation stations

The error from ignoring acceleration between two stations was much less than 0.5% at velocity range of 500 to 2000 m/s. Compared to the total relative uncertainty the error from

Eq. 4.2 was negligible. This was due to typical experiments resulting in mean accelerations from 15,000 to 30,000 g and mean velocities within the plotted range. This concludes that the actual projectile velocity was represented within the uncertainty established in Eq. 4.1.

4.2 Baffled-Tube Data Analysis

After the raw data from the EM and PCB sensors was collected and processed it can be analyzed to determined how the BTRA operated in transit and its the experimental performance. The BTRA operation was categorized as a start, unstart, or wave fall-off. The experimental performance of the BTRA can be quantified by calculating the non-dimensional thrust as a function of projectile Mach number. The experimental performance was then compared to the theoretical performance.

4.2.1 Qualitative Analysis of BTRA Operation

The categories of BTRA operation are defined by where the shock system was compared to the projectile. A start refers to when the shock system was stabilized by the combustion, attached to the projectile and thrust was produced. When the shock system was driven over the projectile by the combustion, it was referred to as an unstart. This was because the projectile cannot produce thrust due to it transiting through high pressure subsonic flow. Lastly, wave fall-off occurs when the combustion does not produce enough energy to stabilize the shock system on the projectile body and it recedes off of the projectile. This produced zero thrust because the projectile was no longer exposed to the high pressure region.

In Fig. 4.3 the uncalibrated pressure trace of a typical start was illustrated with the position of the projectile magnet. The magnet was at the projectile throat and the pressure data was inverted. At the beginning of the time window a small pressure spike and smaller spike are present. They represents the conical shock around the projectile nose cone transiting through supersonic flow and its reflection of the tube wall. Afterwards the vertical magenta line represents the projectile throat and the large pressure spike represents the strong shock system. This system was meant to decelerate the flow for subsonic combustion. This trace

was qualitatively determined to depict start at the given station because the conical shock was present and the strong shock system was behind the projectile throat.

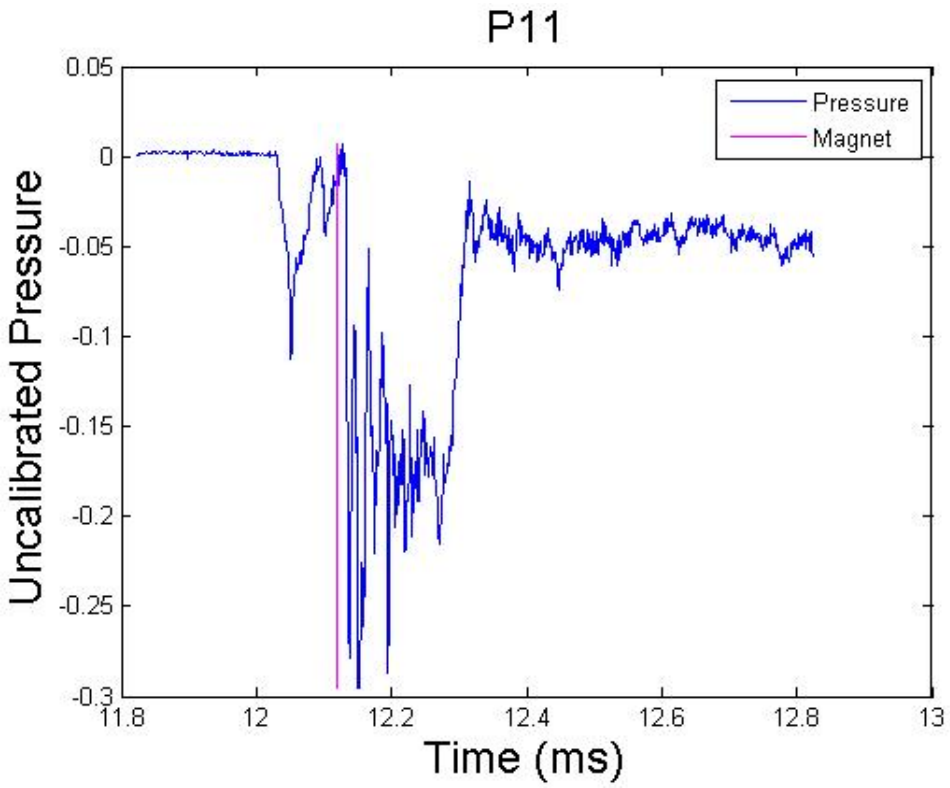

Figure 4.3: Typical BTRA "start" uncalibrated pressure trace

Again unstart occurs when the strong shock system surged ahead of the projectile. In Fig. 4.4 a typical unstart is illustrated. The shock system was clearly ahead of the projectile throat at this point and since no conical shock was present it can be concluded that it has surge in front the projectile by this station.

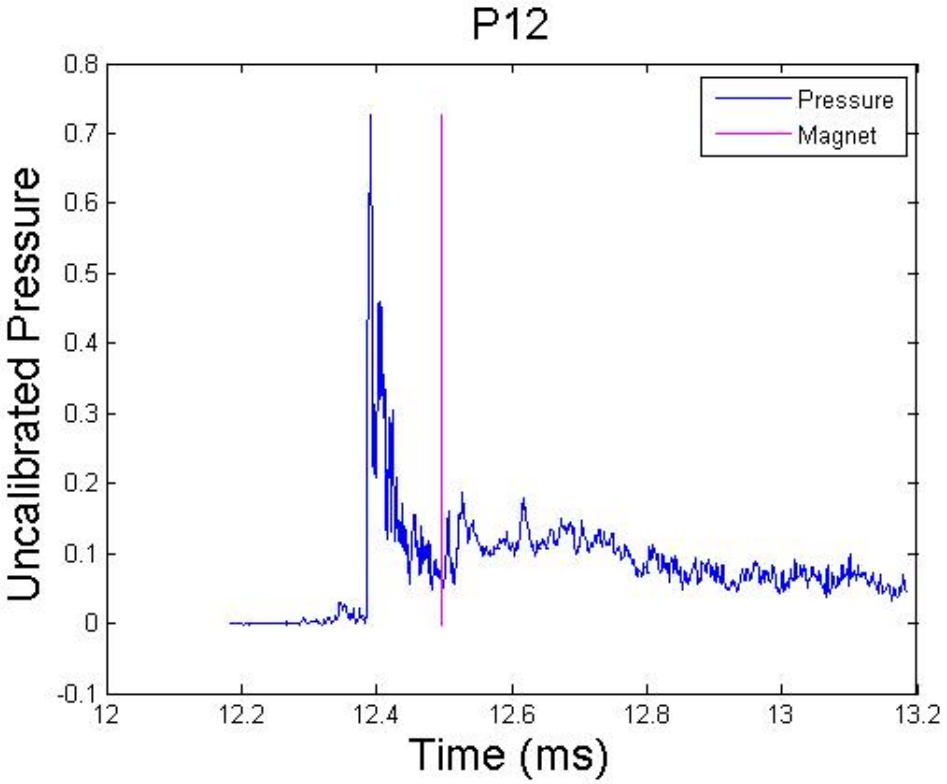

Figure 4.4: Typical BTRA "unstart" uncalibrated pressure trace

A wave fall-off was slightly more difficult to determine by inspection alone. In Fig. 4.5 the conical shock and reflection from the nose cone of the projectile were present and the strong shock system was aft of the projectile throat. However, the time separating the passage of the shock system and projectile body was much larger than Fig. 4.3. By using the mean projectile velocity between the upstream station and this one the distance between the magnet and shock system was determined. Post analysis, it was determined the shock system occurs at a distance greater than the length from the throat to tail of the projectile, thus concluding a case of wave fall-off.

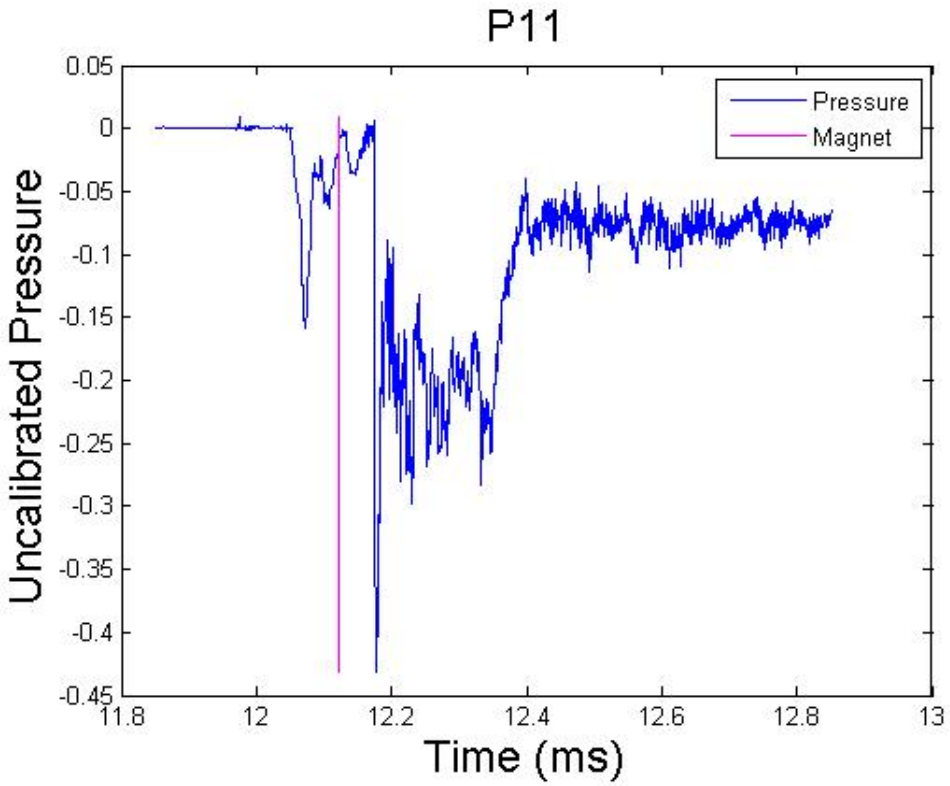

Figure 4.5: Typical BTRA "wave fall-off" uncalibrated pressure trace

4.2.2 BTRA Experimental Performance Calculations

To determine the experimental performance of the ram accelerator the non-dimensional thrust and mean projectile Mach number must be determined. By assuming a constant acceleration in the test section, kinematics was used to solve for the mean acceleration of the projectile. Eq. 4.3 was based on the initial and final projectile velocities in the test section (u_f and u_i) as well as the distance of the test section (Δx).

$$u_f^2 = u_i^2 + 2\bar{a}\Delta x$$

$$\bar{a} = \frac{u_f^2 - u_i^2}{2\Delta x} \tag{4.3}$$

From the mean acceleration Newton's First Law is used to find the experimental thrust on the projectile:

$$F_{exp} = m_p \bar{a} \tag{4.4}$$

where m_p is the mass of the projectile. Next the experimental thrust (F_{exp}) is normalized by the test section fill pressure and bore area to calculate the non-dimensional thrust (I_{exp}).

$$I_{exp} = \frac{F_{exp}}{P_1 A_b}$$

If the initial BTRA theory is followed the then effective area is used, $A_{eff} = A_b \beta$, instead of the bore area.

The mean Mach number of the projectile inside the test tube was determined by taking the average of u_f and u_i. The mean projectile velocity was then normalized by the sound speed of the quiescent mixture.

$$\bar{M} = \frac{\bar{u}}{a}$$

Chapter 5
DISCUSSION AND RESULTS

In this chapter, data from the normal BTRA experiments and slanted BTRA experiments will be presented. Experiments using the methane-nitrous oxide and methane-oxygen-carbon dioxide mixtures were originally reported in a thesis by Glusman [5]. Experiments using methane-oxygen with the normal baffled-tube were originally reported in a thesis by Hambling [12]. The normal baffled-tube experiments using methane-air mixtures and slanted baffled-tube data are exclusive to this thesis. Apart from a presentation of data, the experimental results of all the mixtures and baffle geometries will be used to calibrate and validate the experimentally-driven BTRA model.

5.1 Normal and Slanted BTRA Performance Data

The experiments conducted in the BTRA were performed with similar methodologies. Each propellant mixture started at a specific equivalence ratio, ϕ, that was deemed to have excess heat release. Then with each subsequent test the propellant mixture was diluted with an inert gas or fuel depending on the mixture class. Once a test resulted in a start the mixture ratio was maintained and the entrance Mach number and fill pressure were varied. In this section only the successfully started normal BTRA experiments will be discussed while the findings of the slanted BTRA experiments will be presented in full.

5.1.1 Normal Baffled-Tube Data

The normal BTRA was tested at a wide range of Mach numbers, propellant heat releases, and fill pressures. In total 35 thrust producing experiments over 4 propellant mixtures are presented for discussion. The following tables show the initial and final projectile velocities,

projectile mass, test section fill pressure, propellant mixture, experimental average projectile Mach number, and the experimental non-dimensional thrust. The performance of each one of these mixtures is compared to the initial performance model for the BTRA. For this comparison the thrust, experimental and theoretical, were normalized by the effective area in Eq. 2.6.

The first propellant used during the investigation of the normal BTRA performance was the $1CH_4+2O2+2CO2$ mixture (Table. 5.1). To map the operation envelope in this mixture the entrance velocity was varied from 748 to 910 m/s. The fill pressure was varied slightly as well but due to the lack of confidence in the structural integrity of normal baffles the pressure was raised no further. The largest non-dimensional thrust $I_{exp} = 9.39$ was produced at the lowest average projectile Mach number. This result enforces the theoretical concept of "negative drag" discussed in Chapter 2. However, the next largest non-dimensional thrust occurs near the highest average Mach number. The carbon dioxide content on average was 2 moles but from varied from 1.9 to 2.4 during experiments.

Table 5.1: Normal BTRA experiments with methane-oxygen-carbon dioxide (Q = 11.9)

Shot Name	**Chemistry**	u_i **(m/s)**	u_f **(m/s)**	m_p **(g)**	P_1 **(MPa)**	$\bar{M}$	I_{exp}
HS1926	$1CH_4 + 2O_2 + 2CO_2$	900	1050	145.6	1.02	3.12	9.12
HS1927	$1CH_4 + 2O_2 + 2.4CO_2$	910	950	148.8	0.997	3.01	2.44
HS1929	$1CH_4 + 2O_2 + 2CO_2$	854	975	149.1	1.02	2.92	7.10
HS1930	$1CH_4 + 2O_2 + 1.9CO_2$	856	900	127.6	1.02	2.80	2.11
HS1931	$1CH_4 + 2O_2 + 2CO_2$	815	987	128.5	1.22	2.88	7.10
HS1932	$1CH_4 + 2O_2 + 1.9CO_2$	797	970	145.7	1.23	2.81	7.94
HS1933	$1CH_4 + 2O_2 + 1.9CO_2$	748	927	143.7	1.00	2.66	9.39
HS1936	$1CH_4 + 2O_2 + 1.9CO_2$	792	944	145.6	1.22	2.76	6.83

The non-dimensional thrust data for the $1CH_4 + 2O2 + 2CO2$ mixture was plotted as a function of Mach number in Fig. 5.1. The SBRA theoretical curve with no drag ($c_d = 0$)

and initial BTRA theoretical curve with varying drag coefficients are shown along side the data. As the drag coefficient increased the model agreed with the low Mach number non-dimensional thrust values but does not possess a steep enough slope to reflect the local data trend. Furthermore, the peak in non-dimensional thrust at the higher Mach number value was not recognized by the model. The experimental BTRA data does show a maximum non-dimensional thrust increase of roughly 35% from the predicted value of the SBRA performance model.

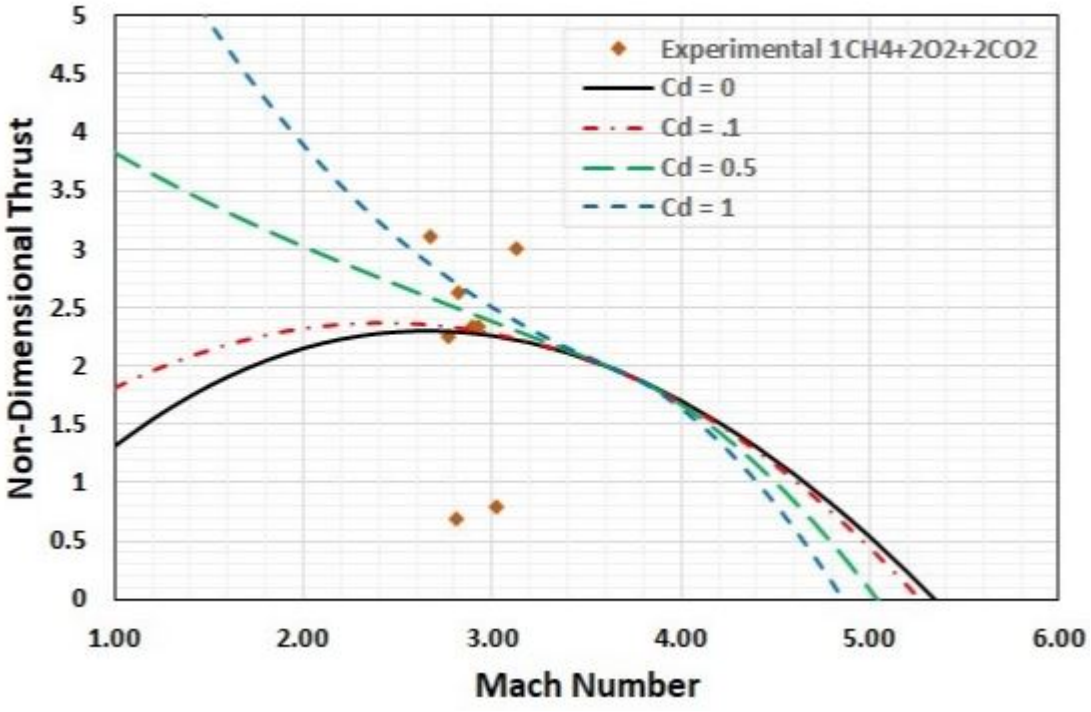

Figure 5.1: Initial BTRA performance curve compared to $1CH_4 + 2O2 + 2CO2$ experimental data

The $2CH_4+4N_2O$ mixture was next in line to be investigated in the normal BTRA (Table. 5.2). With a projectile entrance velocities from 613 to 1110 m/s the mixture had a larger range than any other data set. More specifically, the lowest entrance velocity was a 13% reduction in the lowest previous entrance velocities of the ram accelerator. The mixture also

possessed the most non-dimensional heat release successfully operated in the ram accelerator. It produced the most non-dimensional thrust out of all four mixtures investigated. The low average Mach numbers produced the highest non-dimensional thrust values which suggested the theorized "negative drag" had validity.

Table 5.2: Normal BTRA experiments with methane-nitrous oxide (Q = 12.8)

Shot Name	**Chemistry**	u_i **(m/s)**	u_f **(m/s)**	m_p **(g)**	P_1 **(MPa)**	$\bar{M}$	I_{exp}
HS1937	$2CH_4 + 4N_2O$	842	971	145.8	1.01	3.00	7.37
HS1939	$2CH_4 + 4N_2O$	844	1010	145.7	1.54	3.07	6.53
HS1941	$2CH_4 + 4N_2O$	845	1080	139.4	1.53	3.17	8.85
HS1942	$2CH_4 + 4N_2O$	1050	1150	139.8	1.02	3.62	7.04
HS1943	$2CH_4 + 4N_2O$	844	1070	140.2	2.13	3.15	6.14
HS1944	$2CH_4 + 4N_2O$	1110	1220	139.5	1.54	3.85	5.42
HS1945	$2CH_4 + 4N_2O$	732	935	139.9	1.02	2.75	10.2
HS1947	$2CH_4 + 4N_2O$	613	875	138.7	1.54	2.46	7.73

The performance data of the $2CH_4 + 4N_2O$ mixture was compared to the theoretical models in Fig. 5.2. At best it produced 8% less maximum non-dimensional thrust than expected from the SBRA performance model ($c_d = 0$). Even with the addition of baffle drag the theory-experiment discrepancy only widened. This mixture displayed different performance trends than the $1CH_4 + 2O2 + 2CO2$ mixture. Instead of the data creating non-dimensional thrust peaks at the low and high Mach numbers, it tapered off as Mach number increased.

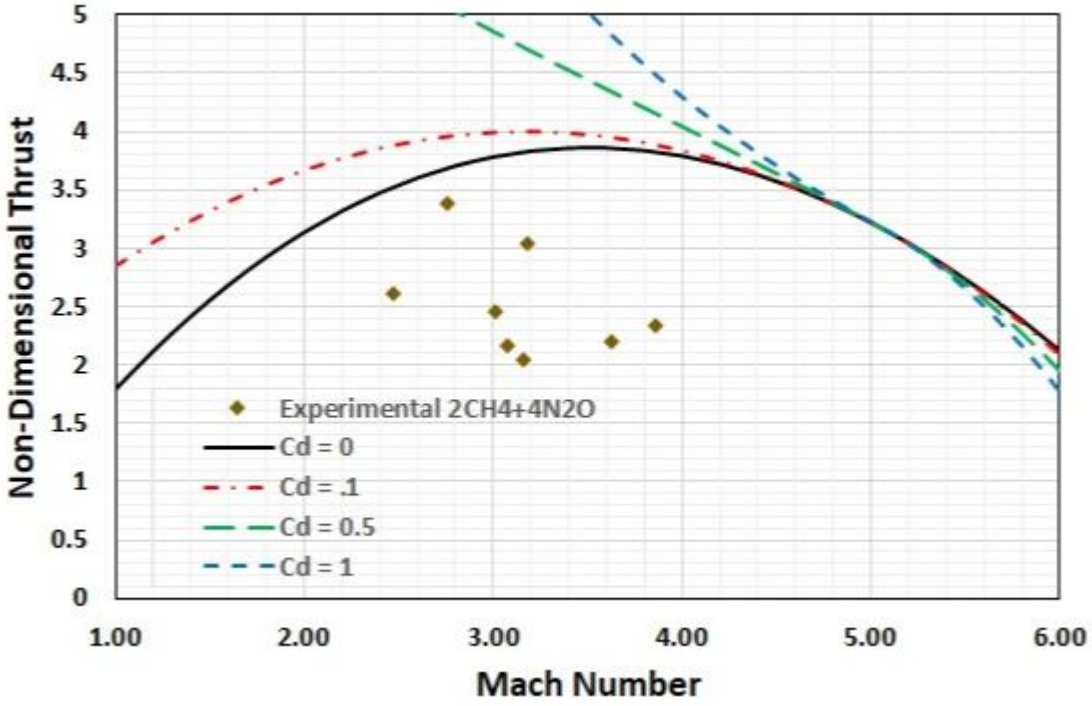

Figure 5.2: Initial BTRA performance curve compared to $2CH_4 + 4N_2O$ experimental data

After exploring the use of carbon dioxide and nitrous oxide as low acoustic speed diluent and oxidizer, respectively, a $2.5CH_4 + 2O2$ mixture was investigated (Table 5.3). With respect to entrance velocity range this mixture was able to operate at higher Mach numbers than the $1CH_4 + 2O2 + 2CO2$ mixture but not as low as then the $2CH_4 + 4N_2O$ mixture. The largest non-dimensional thrust was lower then both of the previous mixtures, which concurs with thrust being proportional to heat release. Similar to the $1CH_4 + 2O2 + 2CO2$ mixture the two largest non-dimensional thrust values occur near the highest and lowest average Mach numbers.

Table 5.3: Normal BTRA experiments with methane-oxygen (Q = 10.8)

Shot Name	**Chemistry**	u_i **(m/s)**	u_f **(m/s)**	m_p **(g)**	P_1 **(MPa)**	$\bar{M}$	I_{exp}
HS1984	$2.5CH_4 + 2O_2$	964	1053	138.7	0.951	2.66	6.01
HS1987	$2.5CH_4 + 2O_2$	842	952	146	0.965	2.37	7.12
HS1988	$2.5CH_4 + 2O_2$	1031	1130	146	1.08	2.85	6.35
HS1989	$2.5CH_4 + 2O_2$	839	980	146	1.52	2.4	5.44
HS1990	$2.5CH_4 + 2O_2$	1026	1090	145	1.48	2.81	3.54
HS1995	$2.5CH_4 + 2O_2$	1026	1070	140	0.999	2.75	4.21
HS1996	$2.5CH_4 + 2O_2$	1053	1146	115	0.972	2.9	5.32
HS1999	$2.5CH_4 + 2O_2$	1053	1133	145	1.01	2.89	5.54
HS2000	$2.5CH_4 + 2O_2$	1061	1159	150	1.08	2.93	6.67
HS2001	$2.5CH_4 + 2O_2$	1058	1156	150	1.09	2.92	6.53
HS2002	$2.5CH_4 + 2O_2$	1053	1161	150	1.10	2.92	7.19

When comparing the $2.5CH_4 + 2O2$ mixture data to the SBRA and BTRA theoretical models (Fig. 5.3) it was seen that the mixture underperformed expectations. The data presented a slightly different but similar performance trend as the previously discussed mixtures. It had peaks of non-dimensional thrust at its Mach number limits like the $1CH_4$+$2O2$+$2CO2$ mixture but a wider range of operational Mach numbers akin to the $2CH_4 + 4N_2O$ mixture. With a non-dimensional heat release lower and sound speed higher than both mixtures it was undetermined why the $2.5CH_4 + 2O2$ mixture performance possess qualities of both.

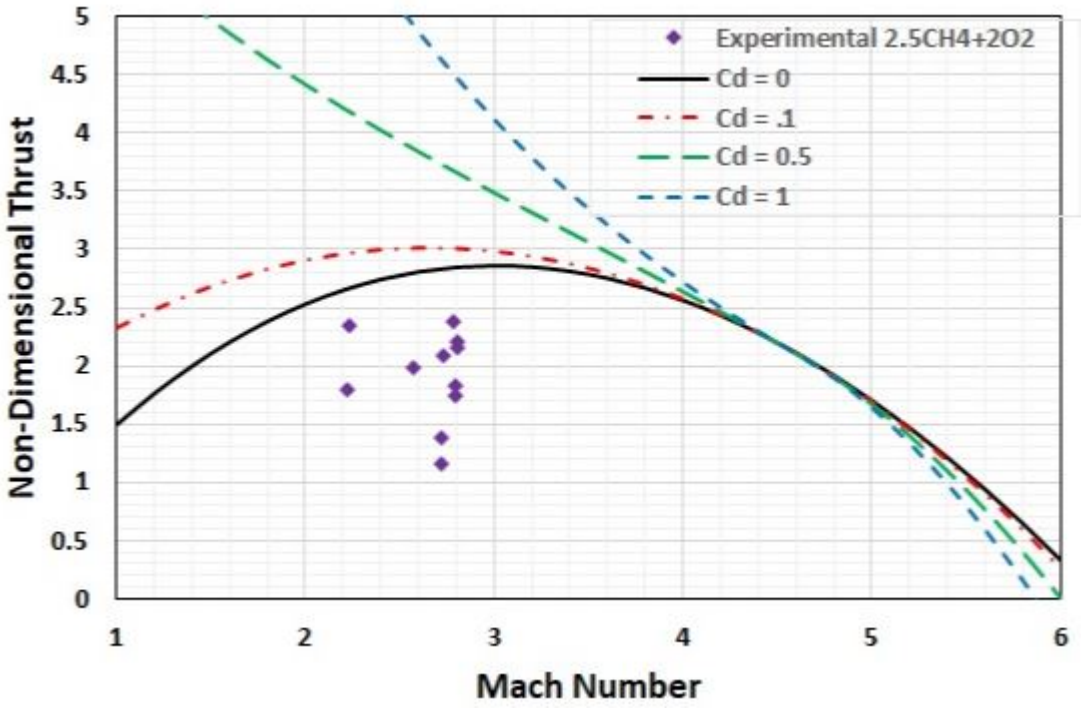

Figure 5.3: Initial BTRA performance curve compared to $2.5CH_4 + 2O2$ experimental data

Lastly, the $1CH_4 + 2O2 + 7.92N_2$ test series covered a similar entrance velocity range as the $2.5CH_4 + 2O2$ mixture. The resultant non-dimensional thrusts are lower, corresponding to the lower non-dimensional heat release as expected. At the largest Mach number the most non-dimensional thrust was produced, again similar to the previous mixtures without N_2O. However,the lower Mach number did not produce a similar value of non-dimensional thrust. Displayed in Fig. 5.4 the data was compared to the BTRA and SBRA performance model. It showed similar theory-experiment discrepancies as the $2.5CH_4 + 2O2$ mixture.

Table 5.4: Normal BTRA experiments with methane-air (Q = 7.9)

Shot Name	**Chemistry**	u_i **(m/s)**	u_f **(m/s)**	m_p **(g)**	P_1 **(MPa)**	$\bar{M}$	I_{exp}
HS2003	$1CH_4 + 2O_2 + 7.52N_2$	1075	1106	135	1.07	3.09	1.84
HS2004	$1CH_4 + 2O_2 + 7.52N_2$	1072	1118	135	1.03	3.11	2.83
HS2005	$1CH_4 + 2O_2 + 7.52N_2$	1081	1109	132	1.04	3.11	1.72
HS2006	$1CH_4 + 2O_2 + 7.52N_2$	1055	1104	131	1.26	3.06	2.38
HS2008	$1CH_4 + 2O_2 + 7.52N_2$	1081	1130	131	1.06	3.14	2.92
HS2009	$1CH_4 + 2O_2 + 7.52N_2$	1093	1156	115.3	1.01	3.19	3.52
HS2011	$1CH_4 + 2O_2 + 7.52N_2$	1067	1102	120	1.06	3.08	2.08
HS2013	$1CH_4 + 2O_2 + 7.52N_2$	830	886	120	1.01	2.43	2.56

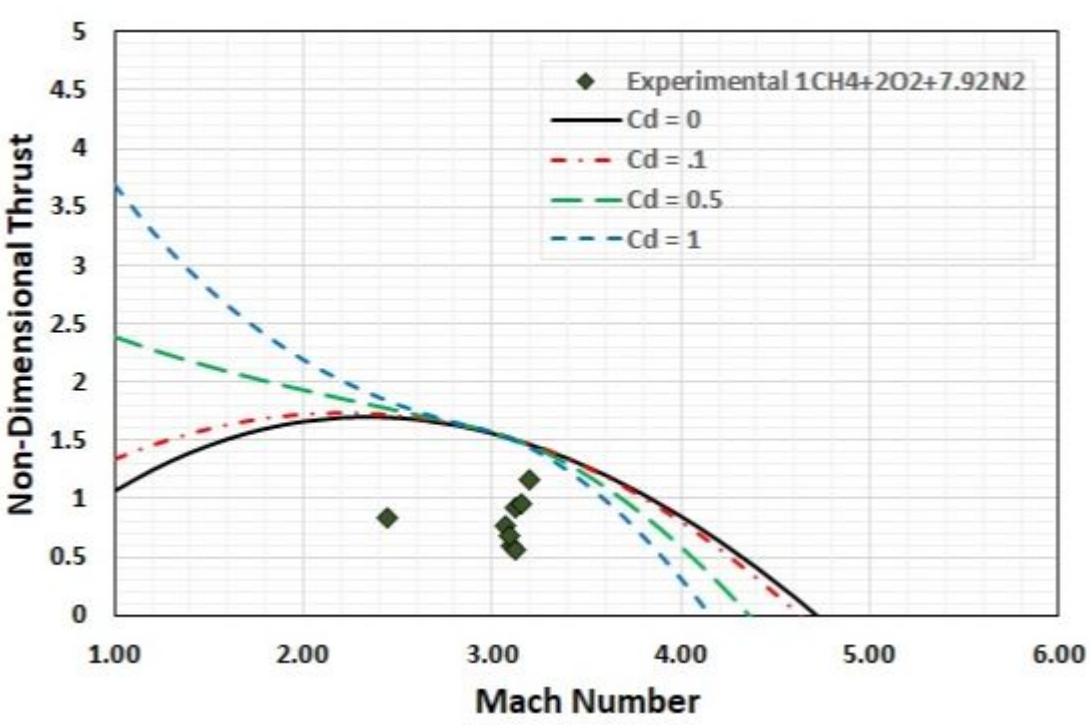

Figure 5.4: Initial BTRA performance curve compared to $1CH_4+2O2+7.92N_2$ experimental data

For all the mixtures without a CO_2 diluent, the experimental non-dimensional thrust underperformed with respect to the predicted values from the SBRA model. The addition of drag into the model only worsened the discrepancy. On the other hand, the $CH_4 + 2O2 + 2CO_2$ mixture out performed the expected SBRA non-dimensional thrust and the addition of baffle drag to the model increased agreement with the experiment. However, none of the performance data from any mixture followed the theoretical trends expected. This posed two questions: Why does the addition of a CO_2 diluent increase experimental drag and what is the cause of the under-performing mixtures?

The latter of the two questions was explored in [5]. It was proposed that the total amount of non-dimensional heat release was not being applied to the high pressure region of the control volume. A combustion sensitivity study was conducted where the non-dimensional heat release was reduced and the effective control volume cross sectional area was enlarged. The results of this study can be seen in Fig. 5.5. The non-dimensional heat release was decreased with the multiplication of an efficiency factor ranging from 1 to 0.4, where 1 meant complete combustion (a). The effective area was increased by the multiplication of a corrective factor ranging from 1 to 2.5 (b). The change to the effective area was explained to indicated incomplete combustion due to the depth of the baffle chambers. The variation of the non-dimensional heat release was explained to indicated a differing equilibrium state at the thermally choked plane. Both variations made notable changes leading to better agreement between data and theory but neither had a rigorous basis.

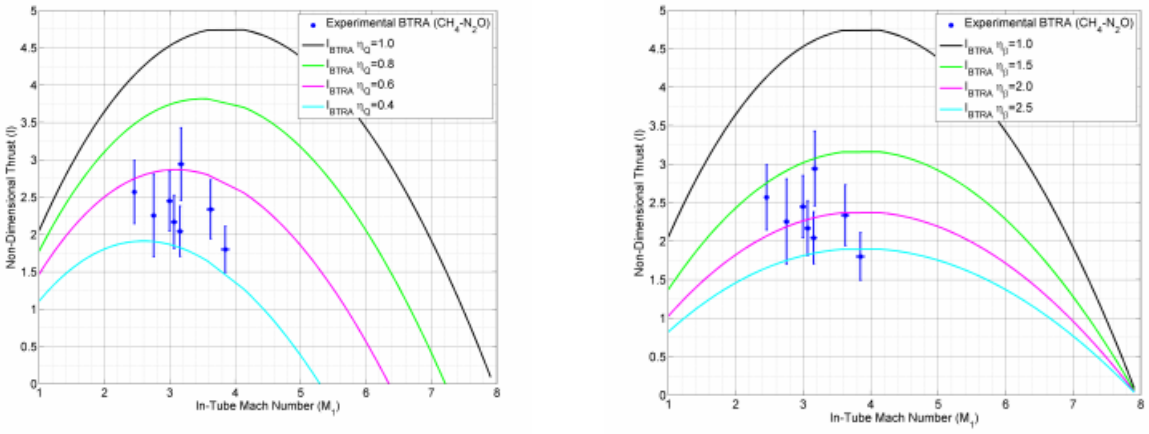

(a) Combustion efficiency

(b) Void volume efficiency

Figure 5.5: Combustion sensitivity study

5.1.2 Slanted Baffled-Tube Experiments

Experiments conducted in the slanted BTRA were done with inward and outward slanted baffles. The initial slanted baffles were designed to be inward slanted but after sufficient exploration of that operation space the baffles were installed in reverse. A similar series of tests were conducted. The slanted BTRA tests were done excursively with fuel-rich methane-oxygen mixtures. The amount of methane was varied to toggle the non-dimensional heat release parameter until the projectile successful produced thrust through the test section. Next the fill pressure was increased until an "unstart" occurred.

A total of 12 thrust producing shots were performed with the inward slanted BTRA. Ten were in a mixture with a $\phi = 4$ and two were in with a $\phi = 3.5$. In Table. 5.5 the experimental data is shown. Along with the mixture the entrance velocity, fill pressure and projectile throat diameter were varied. It was found that to produce thrust the projectile had enter the test section at a velocity greater than 1000 m/s and the methane content could not be below $\phi = 3.5$. This increased the requisite entrance velocity and decreases the heat release limit exhibited in the normal BTRA experiments with the same mixture class.

However, it was found that the projectile throat diameter plays a part in maximizing thrust.

Table 5.5: Slanted inward BTRA experiments

Shot Name	**Chemistry**	u_i **(m/s)**	u_f **(m/s)**	m_p **(gm)**	d_p **(cm)**	P_1 **(MPa)**	$\bar{M}$	I_{exp}
HS2025	$3.5CH_4 + 2O_2$	1005	1044	145	3.76	0.931	2.64	2.74
HS2027	$4CH_4 + 2O_2$	1034	1036	145	3.76	1.39	2.63	.126
HS2029	$4CH_4 + 2O_2$	1028	1042	135	3.71	1.17	2.63	0.724
HS2031	$4CH_4 + 2O_2$	1008	1064	135	3.61	1.48	2.64	2.34
HS2032	$4CH_4 + 2O_2$	1055	1104	124	3.45	1.42	2.79	3.11
HS2033	$4CH_4 + 2O_2$	1008	1075	127	3.43	1.43	2.66	2.73
HS2035	$4CH_4 + 2O_2$	1053	1102	130	3.30	1.65	2.75	1.83
HS2037	$4CH_4 + 2O_2$	1055	1111	130	3.61	1.93	2.76	1.78
HS2038	$3.5CH_4 + 2O_2$	1058	1143	131	3.61	1.39	2.83	3.85
HS2041	$4CH_4 + 2O_2$	1044	1061	131	3.61	1.08	2.68	0.933
HS2045	$4CH_4 + 2O_2$	1010	1053	127	3.61	1.43	2.63	1.71
HS2046	$4CH_4 + 2O_2$	1039	1143	126	3.61	1.95	2.78	3.20

The initial tests of the inward slanted baffles with a $\phi = 4$ and nominal projectile diameter (3.76 cm) resulted in near negligible thrust levels. It was concluded the combustion zone was being starved of fresh propellant so the gap between the projectile and baffles need to be increases. The projectile throat was decreased to 3.71 cm and the non-dimensional thrust increased by 5.7 times. Fig. 5.6 illustrates the trend as the projectile diameter continued to decrease. Optimal projectile diameter was determined to be 3.61 cm. In future data comparisons the data using the optimal projectile diameter and propellant with a $\phi = 4$ will be used.

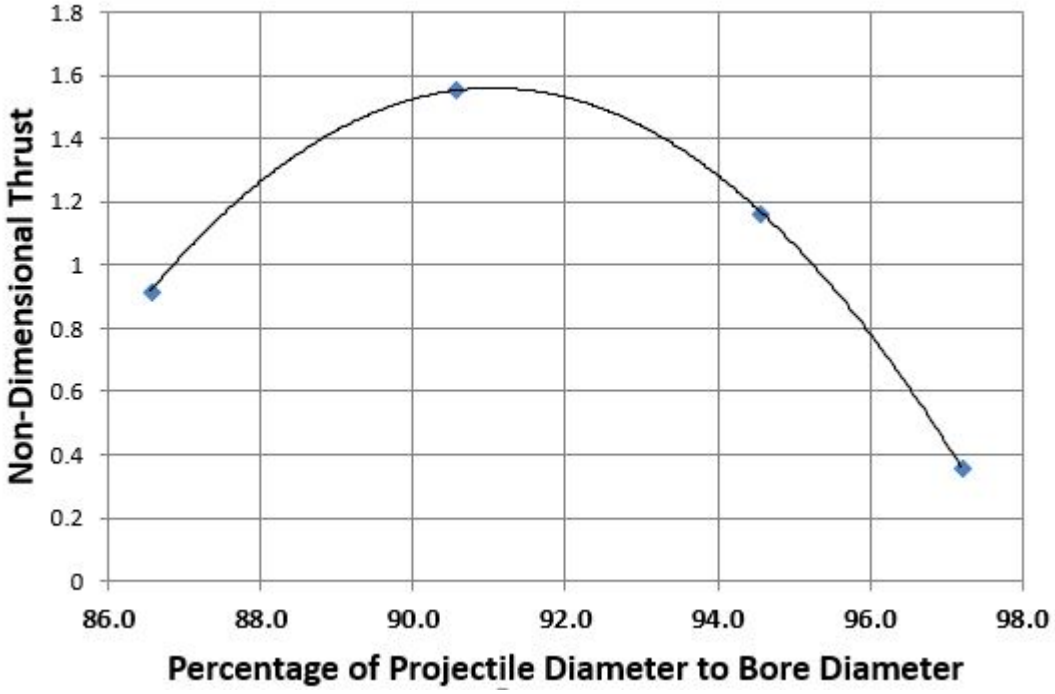

Figure 5.6: Bore-projectile gap affect on thrust

Once the inward slanted BTRA operational envelope was throughly investigated in the given mixture class, the BT were reinstalled in reverse. The collect data is presented in Table. 5.6. The outward slanted BTRA was capable of operating with the excess fuel minimized to $\phi = 3$. In addition the peak fill pressure was 33% higher than the inward BTRA. The outward slanted BTRA seems to perform better in every aspect except the minimum entrance velocity. This characteristic seemed to be a function of the geometry where the minimum entrance Mach number defined by Eq. 2.8 changes along the axial distance due to the slant. An entrance velocity of 1000 m/s or Mach 2.5 must be high enough to obtain a start in a given baffle and transit into the next before the shock system surges ahead of the projectile.

Table 5.6: Slanted outward BTRA experiments

Shot Name	**Chemistry**	u_i **(m/s)**	u_f **(m/s)**	m_p **(gm)**	P_1 **(MPa)**	$\bar{M}$	I_{exp}
HS2052	$4CH_4 + 2O_2$	1013	1081	127	1.08	2.67	3.68
HS2053	$4CH_4 + 2O_2$	1023	1111	127	1.44	2.72	3.63
HS2055	$3.5CH_4 + 2O_2$	1008	1026	127	1.46	2.59	0.699
HS2056	$3.5CH_4 + 2O_2$	1008	1053	127	1.46	2.63	1.77
HS2057	$3CH_4 + 2O_2$	1018	1176	127	1.46	2.80	6.62
HS2059	$3CH_4 + 2O_2$	1034	1212	127	1.76	2.86	6.34
HS2062	$4CH_4 + 2O_2$	1008	1026	127	1.74	2.59	0.586
HS2063	$4CH_4 + 2O_2$	1028	1081	127	1.96	2.69	1.58
HS2064	$4CH_4 + 2O_2$	1034	1143	127	2.10	2.77	3.15
HS2065	$4CH_4 + 2O_2$	1008	1081	127	2.41	2.66	1.77
HS2066	$4CH_4 + 2O_2$	1036	1212	127	2.61	2.87	4.21

With high pressure data from the slanted BTRA the linear scalability with fill pressure was investigated. In conjunction, if the BTRA thrust does not scale with fill pressure the non-dimensional thrust parameter is no longer appropriate. Laying a linear regression line over the thrust per unit area of the slanted BTRA with respect to fill pressure results in Figure 5.7. The inward and outward slanted baffles at a $\phi = 4$ have enough data points to suggest a quasi-linear relationship.

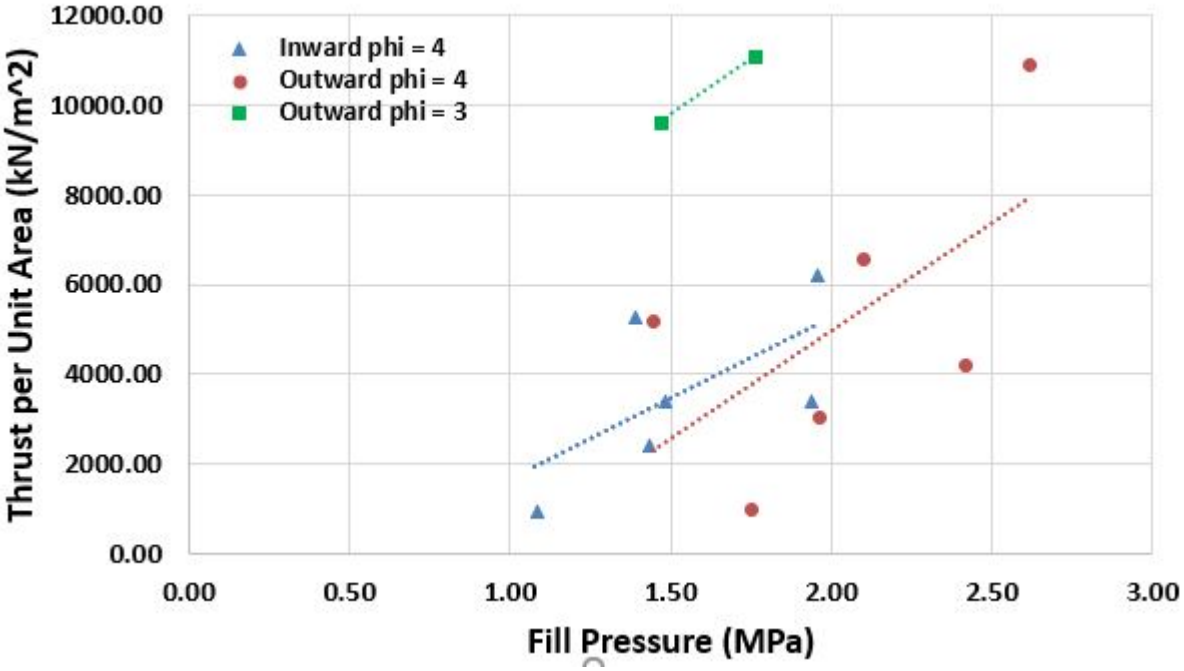

Figure 5.7: Linear scalability of thrust for the slanted BTRA

Besides comparing operational limits another method can be used to determine the efficacy of the slanted baffle configurations. Chapter 4 discussed the interpretation of a pressure trace from the PCB probes in the test section. By tracking the large pressure spike on a pressure trance with respect to the smaller pressure spike the position of the shock system relative to conical shock (projectile nose) was determined. The uncertainties in this method lay in the angle of the conical shock and any signal delay. However, a comparison between slanted baffles can be made. Fig. 5.8-5.9, shows the relative position of the shock system with the distance from nose tip to shoulder and base superimposed.

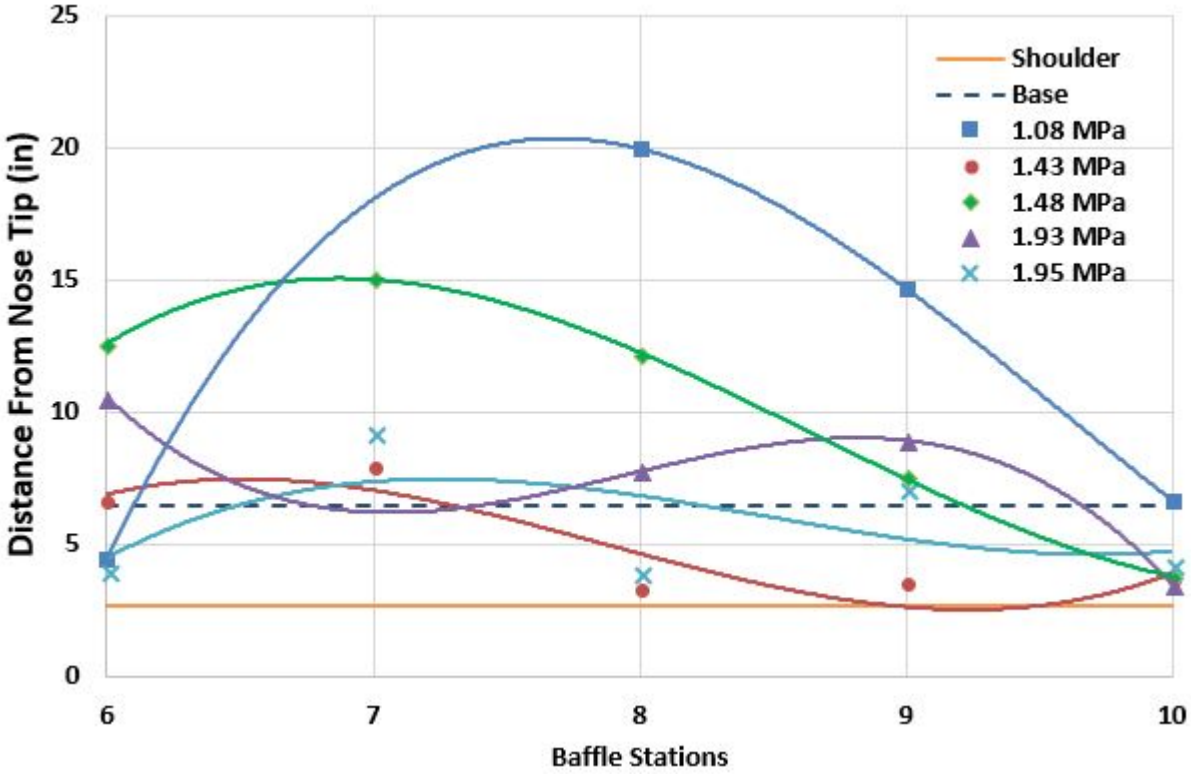

Figure 5.8: Inward slanted baffle shock system position ($\phi = 4$)

The region between the shoulder and base represent the ideal location for the shock system. If it was ahead of the shoulder an "unstart" was in progress and if it was behind the base the shock system had fallen off the projectile completely. From the individual figures it was seen that the shock system stabilizes in the ideal region as the fill pressure increased. When comparing the figures to each other, the outward slanted baffles seemed to drive the shock system toward the projectile base and the inward slanted baffles allowed the shock system to approach the projectile shoulder. The outward baffles were better at attenuating the shock system which allowed operation at higher fill pressures and heat releases.

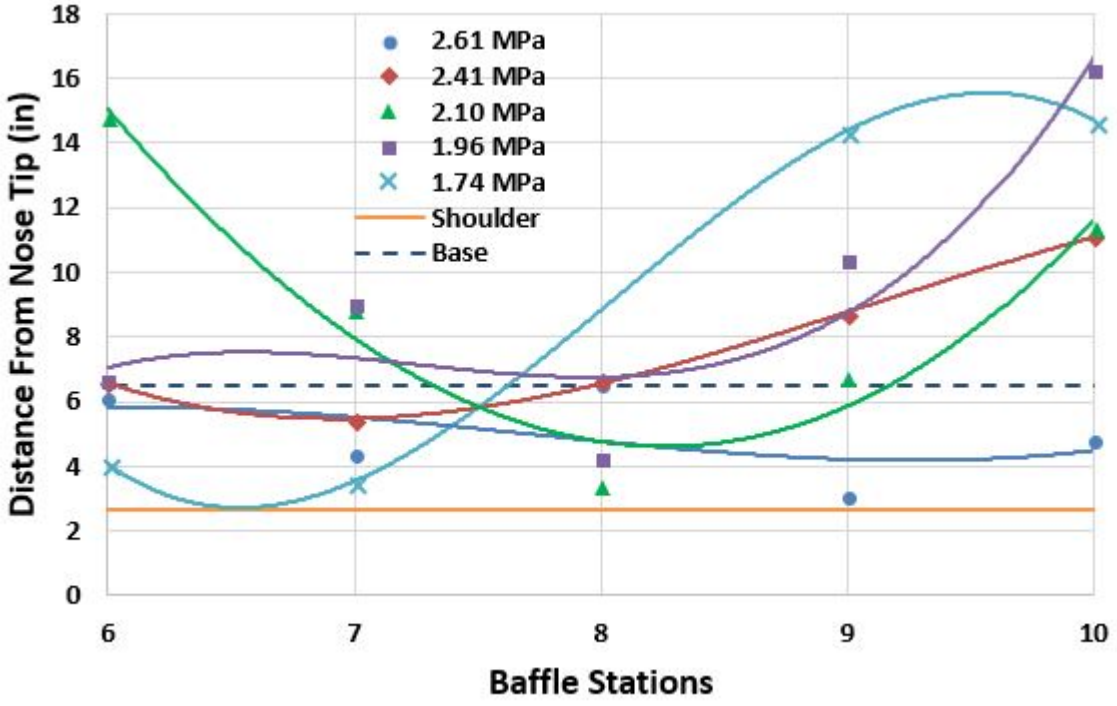

Figure 5.9: Outward slanted baffle shock system position ($\phi = 4$)

From the preliminary tests it was seen that the outward slanted baffles had a larger operational envelop then the inward slanted baffles. The amount of non-dimensional thrust produced was also in favor of the outward slanted but how did they compare to the normal baffles? Fig. 5.10 illustrates the performance of the methane-oxygen mixture class with the three baffle configurations. The data was compared with the theoretical curves from the initial BTRA performance model. It was seen that the inward slanted baffles had the lowest recorded non-dimensional thrust while the outward baffles have the highest. With a $\phi = 3$ mixture the outward slanted baffles out perform the normal baffles with a $\phi = 2.5$ by 41%.

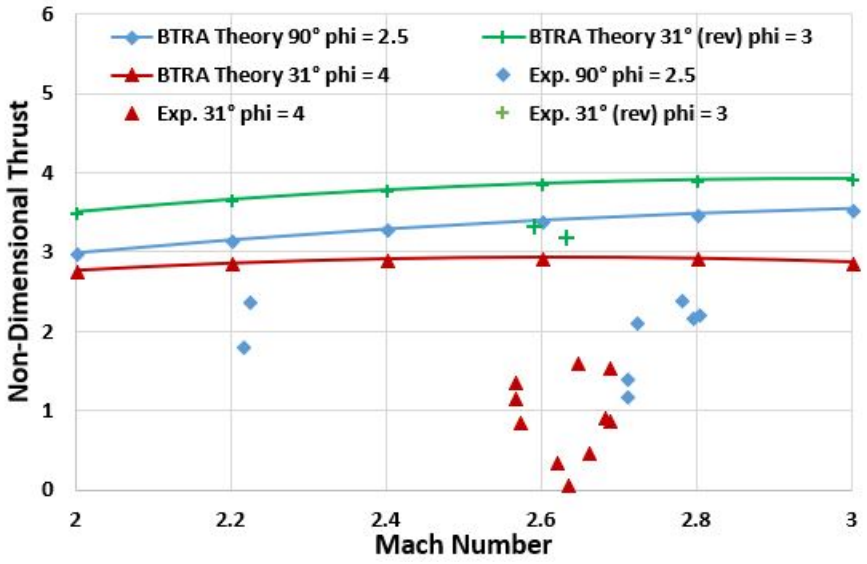

Figure 5.10: Comparison of Methane-Oxygen mixture class in 3 baffle configurations

5.2 Experimentally-Driven Performance Model Application

The initial BTRA performance model did not capture the processes that occur in the BTRA experiments. Three out of the four mixtures compared to the initial theory underperformed while the $1CH_4 + 2O_2 + 2CO_2$ mixture correlated well at low Mach numbers. From the combustion sensitivity study previously completed the reduction of the non-dimensional heat release reduced the expected non-dimensional thrust to the experimental values. A combustion efficiency was determined using dimensional analysis and the mixture chemical properties. The drag was then directly related to the geometry of the control volume used in analysis. In this manner the combustion efficiency and drag were coupled through the control volume geometry. In this section the results of these modifications to the BTRA model are presented along side a comparison to the data.

5.2.1 Combustion Efficiency

For each mixture the combustion efficiency (Eq. 2.10 was determined using the chemical kinetic software Cantera, a total enthalpy balance, and a length scale taken as a single baffle

length. The results for the heat release, q, and heat release rate, $\dot{q}$ are presented in Table. 5.7. The ratio of $\frac{\dot{q}}{q}$ represents an effective reaction rate for each mixture. Each of the values were found at the pressure and temperature associated with the CJ condition. The sound speed at the exit of the thermally choked plane was determined by iterating a total enthalpy balance between the shock system and thermally choked plane at each projectile Mach number by incrementally changing the product temperature.

$$h_1(T_1) + h^o_{f1} + \frac{u_1^2}{2} = h_2(T_2) + h^o_{f2} + \frac{a_2^2}{2}$$

This allowed for the calculation of the the high pressure region velocity relative to the laboratory reference frame, $v_{lab} = u_1 - a_2$. The unique combustion efficiency was applied to the BTRA performance model of each mixture using the same aerodynamic drag model as the initial BTRA model.

Table 5.7: Mixture total heat release and heat release rate from CANTERA

Chemistry	q **(MJ)**	$\dot{q}$ **(MW)**	**Reaction Rate,** $\frac{\dot{q}}{q}$ **(1/s)**
$1CH_4 + 2O_2 + 2CO_2$	3.54	1210	342
$2CH_4 + 4N_2O$	4.15	36700	8840
$2.5CH_4 + 2O_2$	4.57	8790	1920
$1CH_4 + 2O_2 + 7.92N_2$	2.53	6030	2380
$4CH_4 + 2O_2$	2.75	4370	1590

The $1CH_4 + 2O_2 + 2CO2$ mixture performance data was plotted along side the BTRA performance model with the combustion efficiency of the given mixture in Figure 5.11. The relatively low reaction rate of the mixture required double digit drag coefficients to induce enough negative drag to obtain thrust in the model. At a Mach number of roughly 3.3, $\eta_q = 1$, this is were v_{lab} goes to zero and the combustion has a large time constant to reaction completion. The non-dimensional thrust was drastically reduced at low Mach numbers due to low combustion efficiencies. Unfortunately, modeling a single baffle chamber of combustion did not produce promising results for the $1CH_4 + 2O_2 + 2CO2$ mixture.

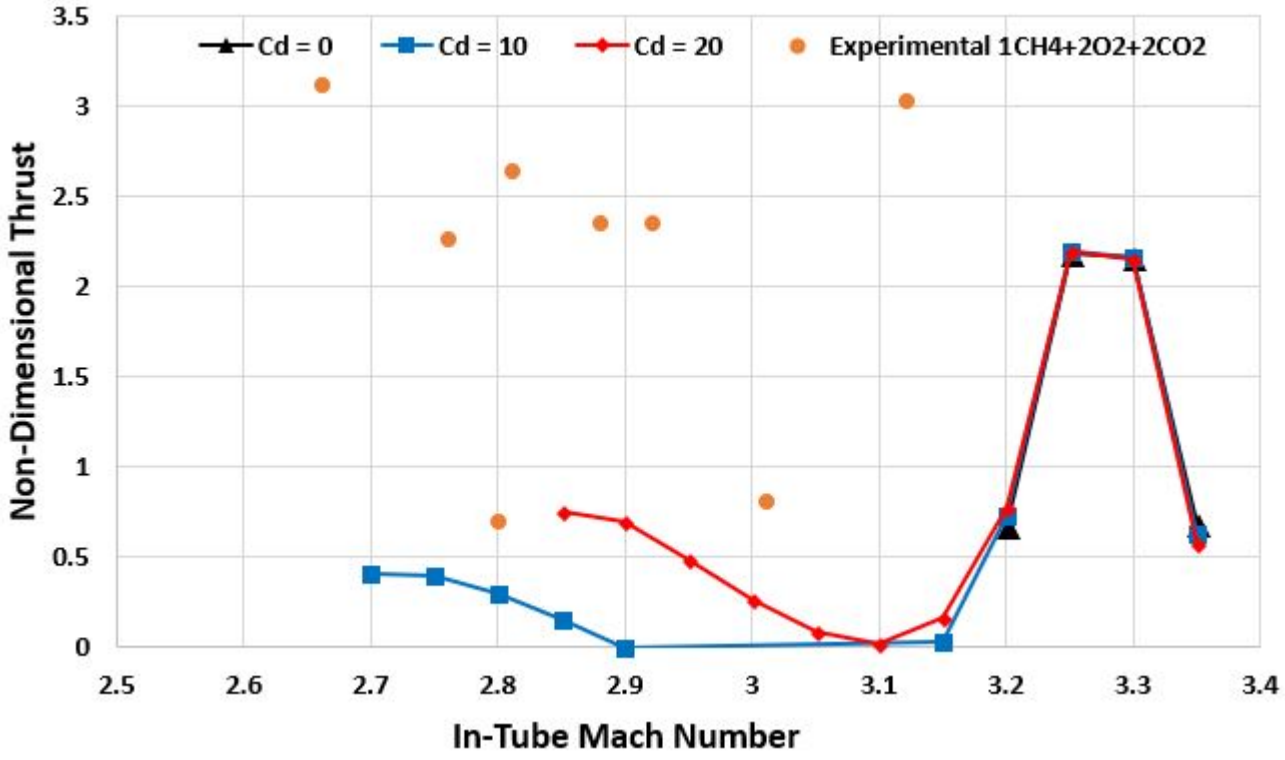

Figure 5.11: BTRA performance model for $1CH_4 + 2O_2 + 2CO2$ mixture with a single baffle of combustion

The BTRA performance model for the $2CH_4 + 4N_2O$ mixture with the combustion efficiency acts different. Fig. 5.12 shows the non-dimensional thrust reduction due to the combustion efficiency. Without accounting for drag, the model showed agreement with the data points at low Mach number. However, due to the large reaction rate of the mixture the combustion efficiency reaches unity at roughly a Mach number of 3. This caused the model to maintain a high non-dimensional thrust after Mach 3 but divergence from the downward slopping data points. The combustion efficiency modification using a single baffle of combustion showed promises for this mixture but lack of drag influence was physically inconsistent.

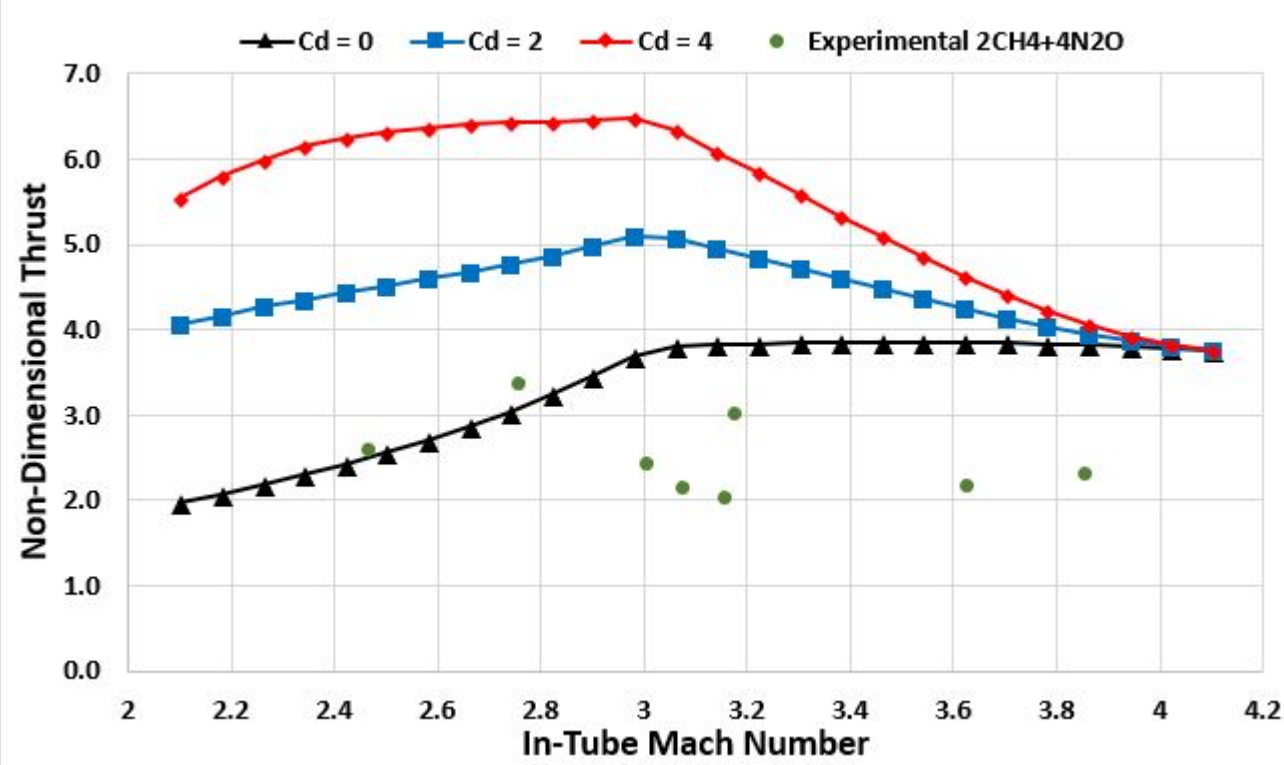

Figure 5.12: BTRA performance model for $2CH_4 + 4N_2O$ mixture with a single baffle of combustion

The BTRA model for the $2.5CH_4 + 2O_2$ mixture with the combustion efficiency modification was the first to show solid agreement with the data. With a $c_d = 7$ the model predicts the performance of the mixture across its Mach number range (Fig. 5.12). The difference between the curve for a $c_d = 0$ and $c_d = 7$ illustrate the effects of drag on the system very well. Without the negative drag contributions at low Mach numbers the model would be ill-fitted. Intriguingly, the low Mach number limitation of the mixture were also predicted. The combustion efficiency did not reach unity until a Mach number of 3.1, which creates a steep slope in the Mach 2.8 to 3 range. This corresponds to the data showing a strong sensitivity to Mach number fluctuations in this region. The single baffle chamber combustion efficiency for the $2.5CH_4 + 2O_2$ mixture model shows great promise with the given drag coefficient.

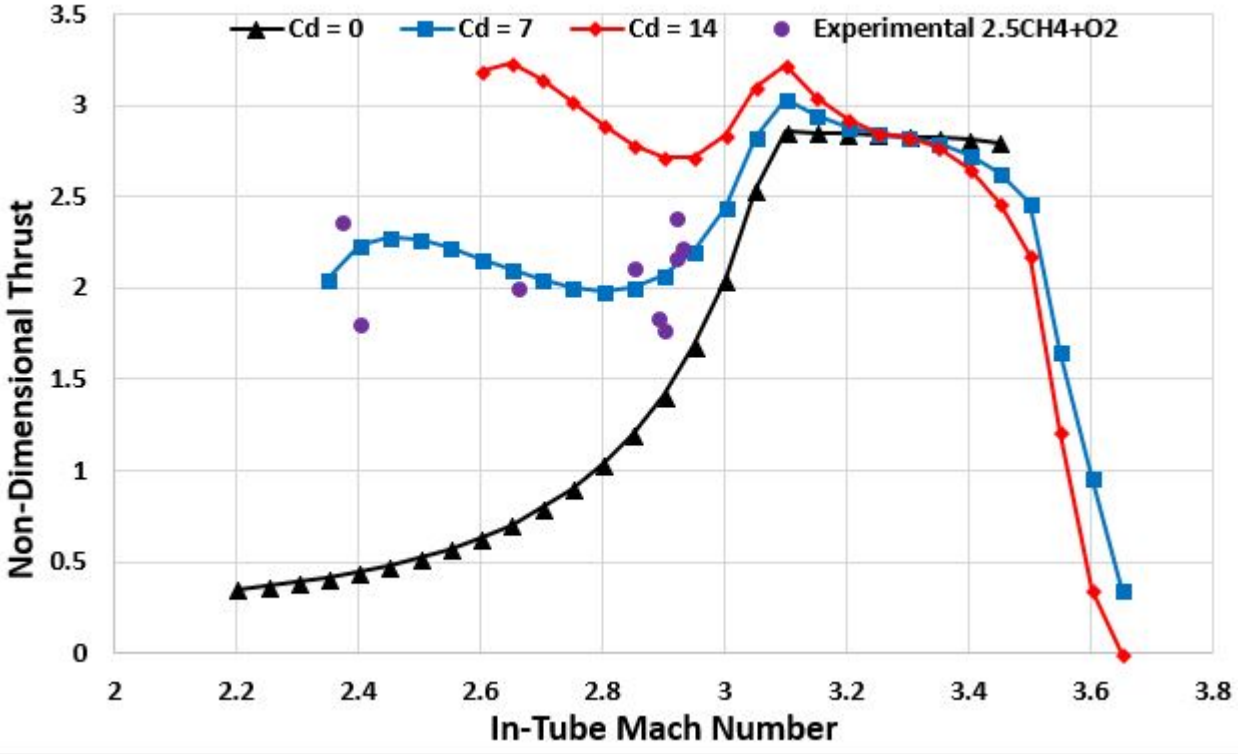

Figure 5.13: BTRA performance model for $2.5CH_4 + 2O_2$ mixture with a single baffle of combustion

Continuing with promising results from the initial application of the combustion efficiency modifier the $1CH_4 + 2O_2 + 7.92N_2$ mixture model is presented in Fig. 5.14. When selecting an appropriate drag coefficient for this data set a $c_d = 3$ mimicked the Mach number sensitive range and the single low Mach number data point. The fact that only changing the drag coefficient resulted in the prediction of both features was a promising result. Again, the variation in c_d shows the effect the drag has on the performance specifically at low Mach numbers. Thus far the mixtures with similar reaction rates have show promise in predicting their performance assuming a single baffle chamber of combustion.

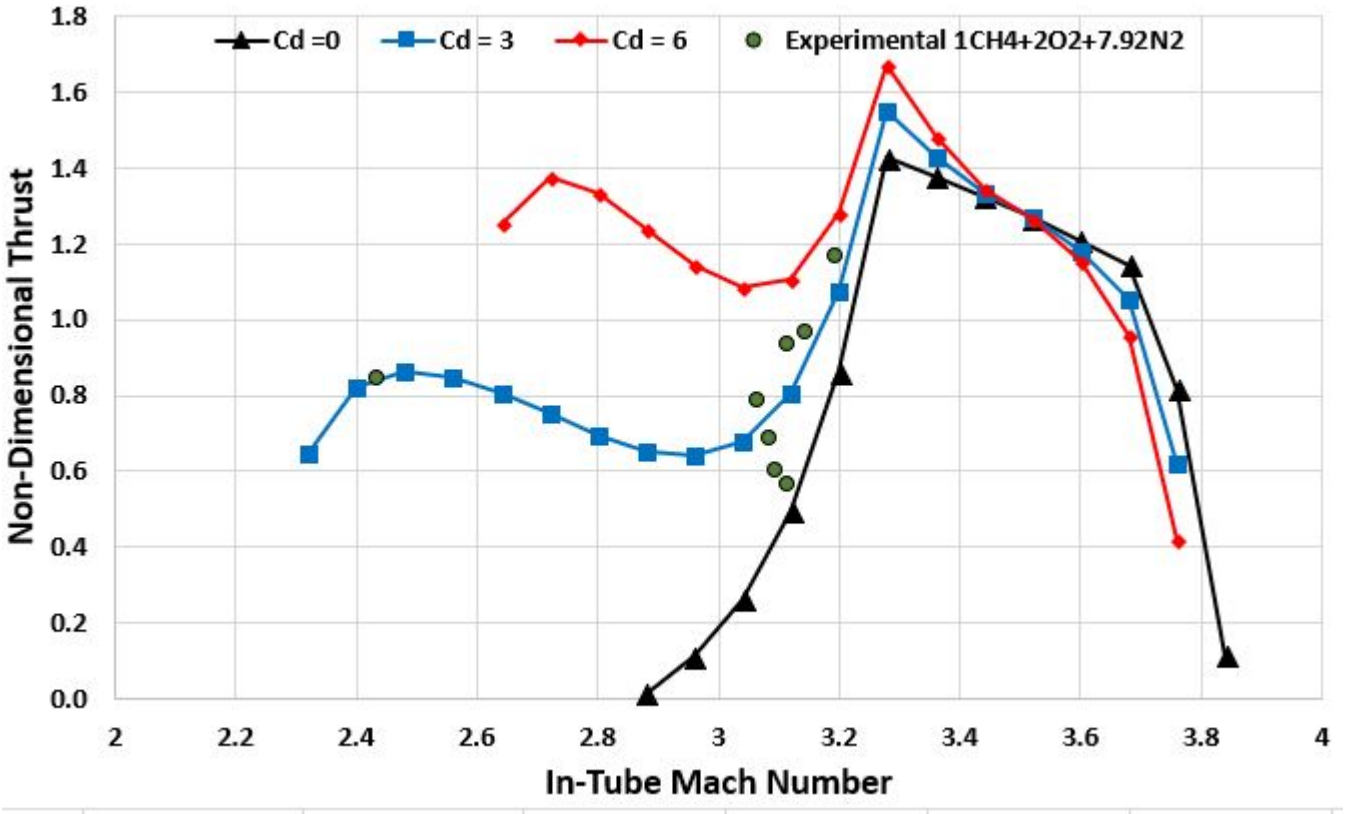

Figure 5.14: BTRA performance model for $1CH_4 + 2O_2 + 7.92N_2$ mixture with a single baffle of combustion

When applying the combustion efficiency modifier to the slanted baffle-tube data the correlation process was more difficult. Without relatively low Mach number data points the $c_d = 0$ predictions were very similar to any prediction with the addition of drag. The inward slanted BT data can be seen in Fig. 5.15 and the outward slanted BT data can be seen in Fig. 5.16. Since the most data points for both configurations were collect with a mixture of $4CH_4 + 2O_2$, that is the only data presented for comparison to the model. The chemical behavior of the mixture was the same for each baffle configuration. At a Mach number of 2.8 the combustion efficiency went to unity causing a maximum in non-dimensional thrust. The abrupt peak caused the Mach number sensitive region from Mach 2.5 to 2.7 which agrees with the data collect in the region very well. The prediction of the Mach number sensitive

region, regardless of drag influence, is encourage for the combustion efficiency validity.

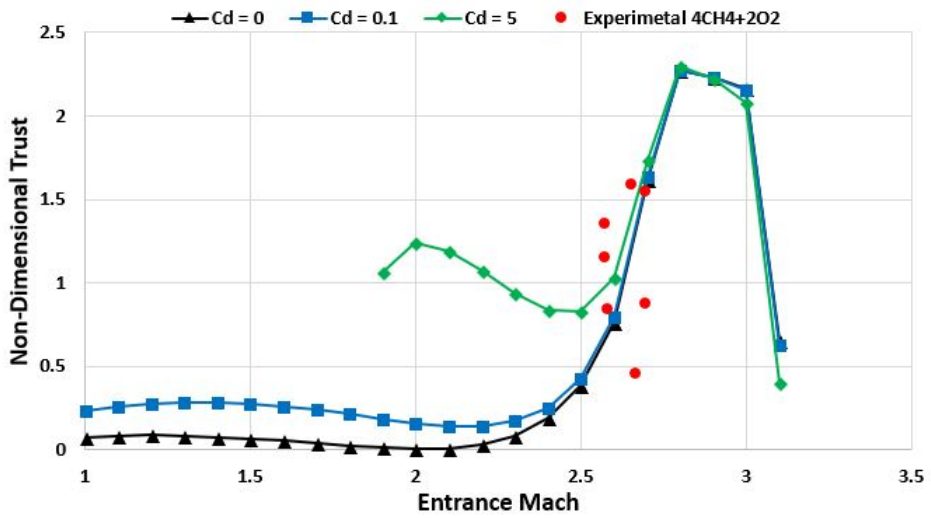

Figure 5.15: Inward slanted BTRA performance model for $4CH_4 + 2O_2$ mixture with a single baffle of combustion

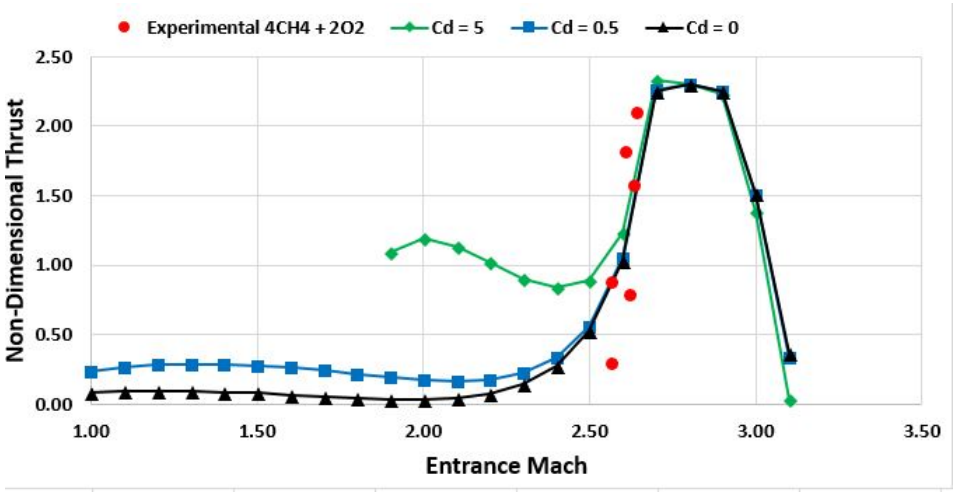

Figure 5.16: Outward slanted BTRA performance model for $4CH_4 + 2O_2$ mixture with a single baffle of combustion

For methane-oxygen and methane-air mixtures the combustion efficiency modifier showed promise assuming the combustion occurred in a single baffle chamber. At the limits of

reaction rates presented the assumptions had to be reconsiders. The $1CH_4 + 2O_2 + 2CO_2$ mixture possessed the lowest reaction rate causing a drastic reduction in predicted non-dimensional thrust that did not reflect the data. An encouraging trend was present but the magnitude of the predicted performance was inadequate. The $2CH_4 + 4N_2O$ mixture possessed the highest reaction rate thus causing an over-prediction in non-dimensional thrust. Relaxing the assumption of a single baffle chamber of combustion, for the two mixtures with poor agreement, lead to an exploration of the effects of the reacting flow length on the model.

5.2.2 Combustion Length Variability Study

Varying the length scale of the combustion efficiency modifier resulted in some intriguing results and may lend some insight into the transient nature of the BTRA. The length scale was varied as increments of baffle chamber lengths. For the low reaction rate mixture, $1CH_4 + 2O_2 + 2CO_2$, the length was increased from 1 to 4 baffle chambers (Fig. 5.17) at a $c_d = 20$. The increase in length reflected the large chemical time scale requiring a longer distance to reach the thermally shocked conditions with obstructing baffles. At 4 baffle chambers of combustion there was a significant increase in data predictability. However, there were two data point with a high deviation from the mean value of the rest of the data set. These points correlated well with the 2 baffle chamber combustion efficiency suggesting an unaccounted for transient effect or mixture composition uncertainty.

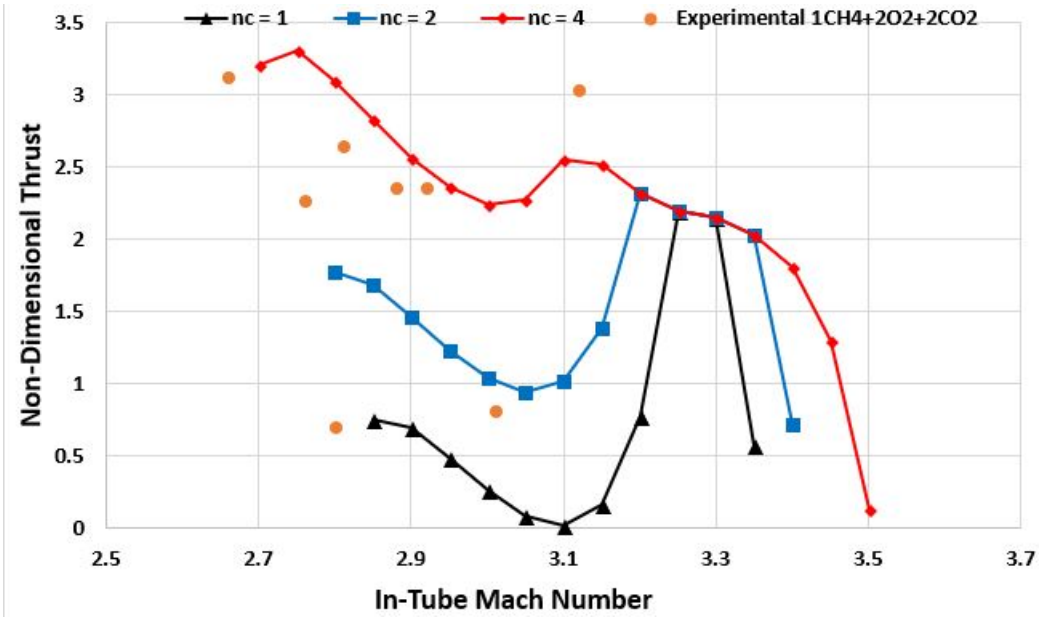

Figure 5.17: BTRA performance model for $1CH_4 + 2O_2 + 2CO2$ mixture with a variable length scale

When considering the high reaction rate of the $2CH_4 + 4N_2O$ mixture the opposite of the former mixture was considered. It was assumed that with a small chemical time scale the combustion would thermally choke the tube in a length scale less than a single baffle chamber. The lengths investigated, along with the baffle chamber length for comparison, were half the baffle length and one-fifth the baffle length (Fig, 5.18) at a $c_d = 2$. The reduction in length reduced the non-dimensional thrust down to adequate magnitudes but did not reflect the trend presented from the data. The combustion efficiency with $\eta_c = 1$ still predicts a curve with a more similar trend to the data. The length variation study for the $2CH_4 + 4N_2O$ mixture did not result in any solid conclusions about the combustion zone characteristics. Although, for the $1CH_4 + 2O_2 + 2CO_2$ mixture the study produced positive results suggesting a low reaction rate may result in a long combustion zone. If the high reaction rate played a minimal role in combustion zone length perhaps it plays a role in the effective area. For the effective area to be relative to a given mixture the control volume used to create the model had to be redefined.

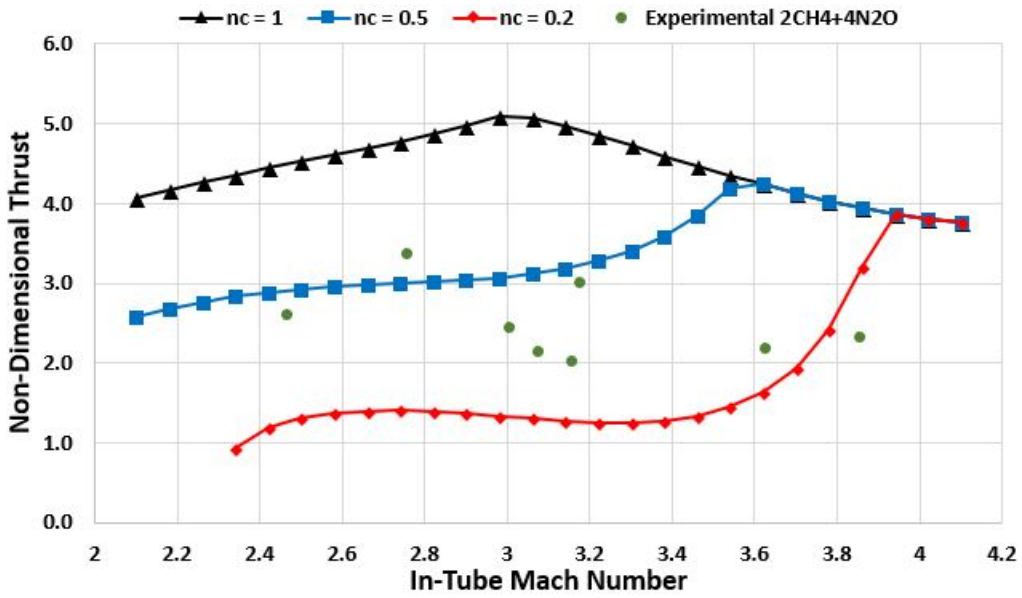

Figure 5.18: BTRA performance model for $2CH_4 + 4N_2O$ mixture with a variable length scale

5.2.3 Drag-Combustion Efficiency Coupling Through Control Volume Aspect Ratio

Using the drag model for the BTRA already established in [7] and discussed in Chapter 2, the control volume geometry could be varied. The drag force was determined from the shear stress caused by the baffles on the surface area of the control volume. After normalizing all the quantities the drag force was determined from the shear stress and aspect ratio of the control volume. The aspect ratio was defined as the length of the control volume over its diameter. Traditionally the control volume was defined as the area between the tube walls, projectile nose tip, and thermally choked plane. For this analysis the c.v. was redefined as the combustion zone behind the projectile terminated by the shock system on the projectile tail and thermally chocked plane (Fig. 5.19).

The length component of the aspect ratio was defined as the combustion zone length used in the combustion efficiency multiplier.The diameter of the aspect ratio was not directly dependent on the combustion process but it does influence the effective area used to normalize the thrust data and predictions. This effectively couples the combustion and drag concepts

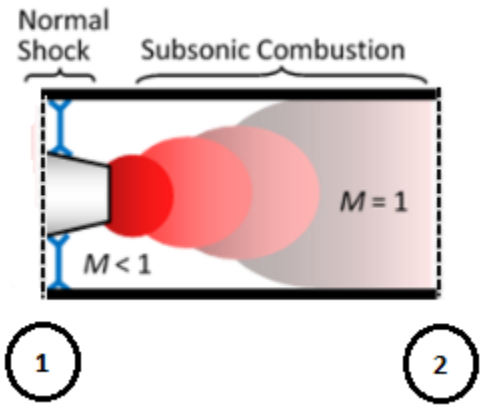

Figure 5.19: Definition of control volume used for analysis

allowing for the aspect ratio to be the single variable to be varied. The new form of the non-dimensional thrust equation:

$$\frac{F}{P_1 A_{eff}} = M_1 \frac{\gamma_1}{\gamma_2}(1+\gamma_2)\sqrt{\frac{\gamma_2-1}{\gamma_1-1}\left(\frac{\eta_q Q + \frac{h_1}{c_{p1}T_1} + \frac{\gamma_1-1}{2}M_1^2 + \frac{4\Psi(\gamma_1-1)}{P_1\gamma_1}\frac{L}{D}}{\frac{h_2}{c_{p2}T_2}+\frac{\gamma_2-1}{2}}\right)} - (1+\gamma_1 M_1^2) - \frac{4\Psi}{P_1}\frac{L}{D} \tag{5.1}$$

Where Ψ was the shear stress, η_q the combustion efficiency, and A_{eff} the nominal area of smooth bore; corresponding to the inner diameter of the BT; corrected for the experimentally determined diameter of the control volume.

$$A_{eff} = A_b \frac{d_{c.v.}^2}{d_b^2} = A_b \lambda$$

To determined the appropriate c.v. aspect ratio of each mixture diameter and length terms were iterated on until the best theory-data agreement occurred. For the best result the drag coefficient related to the shear stress was held at a value of 100 for all mixtures. The results of this process are displayed in Table 5.8. The c.v. diameter was bounded at a minimum of 1.78 cm and maximum of 7.60 cm. Physically these values correspond to the diameter of the projectile tail base and the largest diameter inside the BT, respectively. The

models for the mixtures with the highest and lowest reaction rates were the only ones effected by the aspect ratio variations. The mixtures between were determined to have the originally assume c.v. geometry with the length being a single baffle tube chamber and diameter being the nominal inner BT diameter. At the highest reaction rate, $2CH_4 + 4N_2O$, the control volume was determined to be short and wide, spreading to the maximum allowable diameter and a length slightly less than a baffle chamber. At the lowest reaction rate, $1CH_4+2O_2+2CO_2$, the control volume was determined to be long and skinny. The diameter did not quiet reach the minimum value but the consequences of the long combustion zone are evident in the experimental results.

Table 5.8: Experimentally determined c.v. geometry and λ

Chemistry	**Diameter (cm)**	**Length (cm)**	**Corrective Area Term, λ**
$1CH_4 + 2O_2 + 2CO_2$	2.79	14.4	0.732
$2CH_4 + 4N_2O$	7.60	2.55	1.99
$2.5CH_4 + 2O_2$	3.82	3.19	1.00
$1CH_4 + 2O_2 + 7.92N_2$	3.82	3.19	1.00
$4CH_4 + 2O_2$	3.82	2.43	1.00

Fig. 5.20 displays the modified BTRA performance model with the data from the $1CH_4+2O_2+2CO_2$ mixture. The model predicted the high and low Mach number produced non-dimensional thrust peaks and the trough between them. From the excellent agreement between the theory and data it would seem the stretching of the combustion zone had some validity. This would explain why the $1CH_4+2O_2+2CO_2$ mixture was the only one to exceed the performance predicted by the SBRA model. Its long control volume provided a large surface area for the shear stress to apply work. The excess energy input made up for the low reaction rate. The two outlying points are still unaccounted for so it must be assumed they represent some unknown error possibly still in the theory or mixture composition during the experiment.

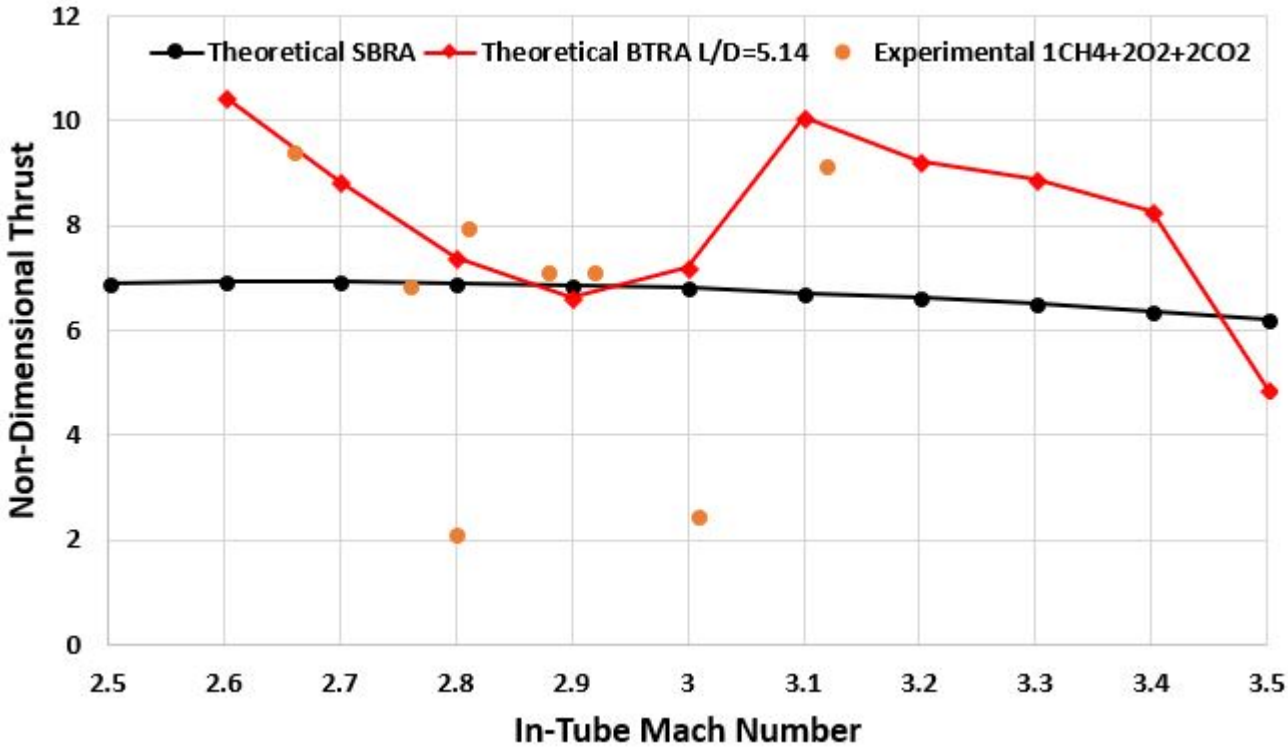

Figure 5.20: Aspect ratio dependent BTRA performance model for $1CH_4 + 2O_2 + 2CO_2$ compared to data

Next the data from the $2CH_4 + 4N_2O$ mixture data and its predicted performance are compared in Figure 5.21. Out of all the model variations the aspect ratio dependence finally predicts the downward sloping non-dimensional thrust as Mach number increases at the correct magnitude. It also predicts the low Mach number operation where the non-dimensional thrust goes to zero. The high reaction rate of this mixture actually works to its disadvantages when trying to meet the predictions of the SBRA model. With a short control volume the shear stress does not have the surface area required to input work and boost the performance as once expected. The large diameter also suggested a significant amount of momentum and energy was spend in the radial direction rather then the axial direction of projectile motion.

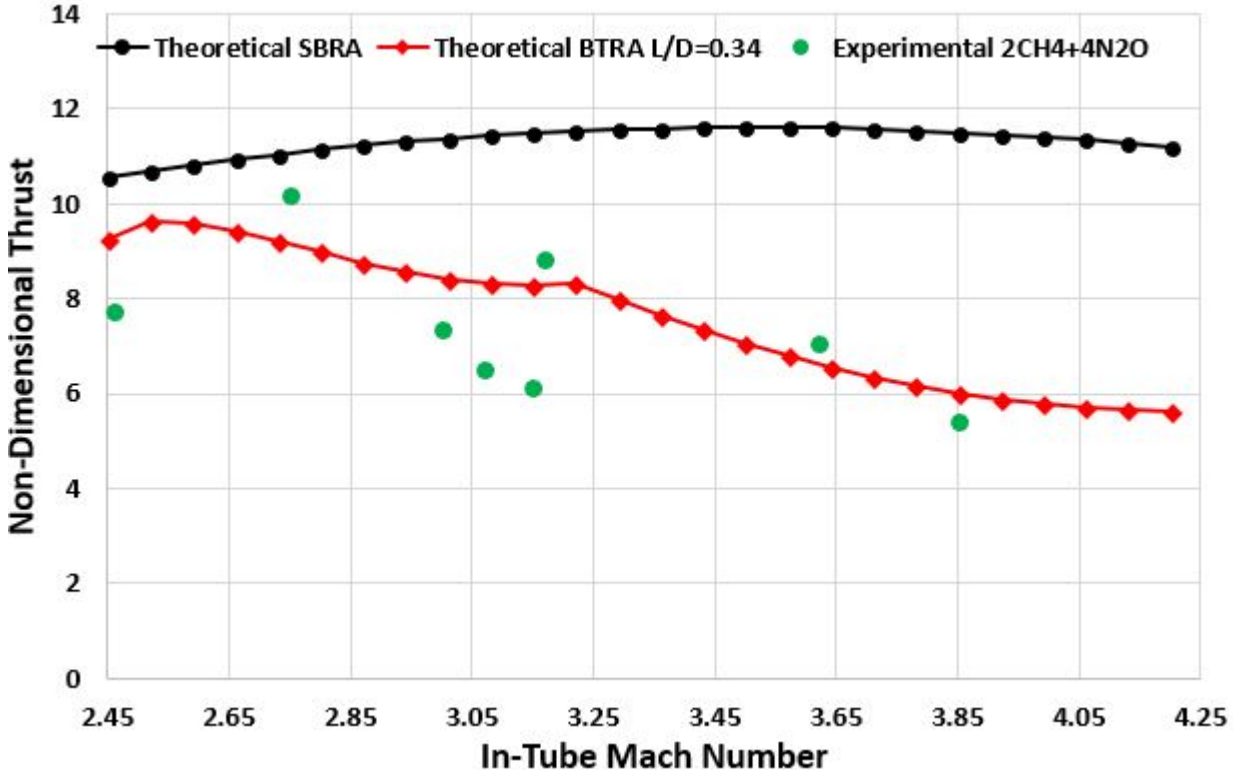

Figure 5.21: Aspect ratio dependent BTRA performance model for $2CH_4 + 4N_2O$ compared to data

With the aspect ratio dependent model the $2.5CH_4 + 2O2$ mixture performance model changed very little. The model still shows excellent agreement with the major features in the data while predicting the low Mach number limits of the mixture (Fig. 5.22). The aspect ratio of the control volume suggests the flow thermally chokes at the baffle inner diameter as the projectile passes through each chamber. This propulsive cycle could be leverage to produce more thrust in two ways: making the baffle chambers longer or having baffles with larger inner diameters in between the chambers. The first would expose the projectile longer to the peak of the high pressure cycle. The second would induce excess energy input from the shear stress on the surface area of the control volume. The two outlying data points are assumed to be measurement errors or experimental errors.

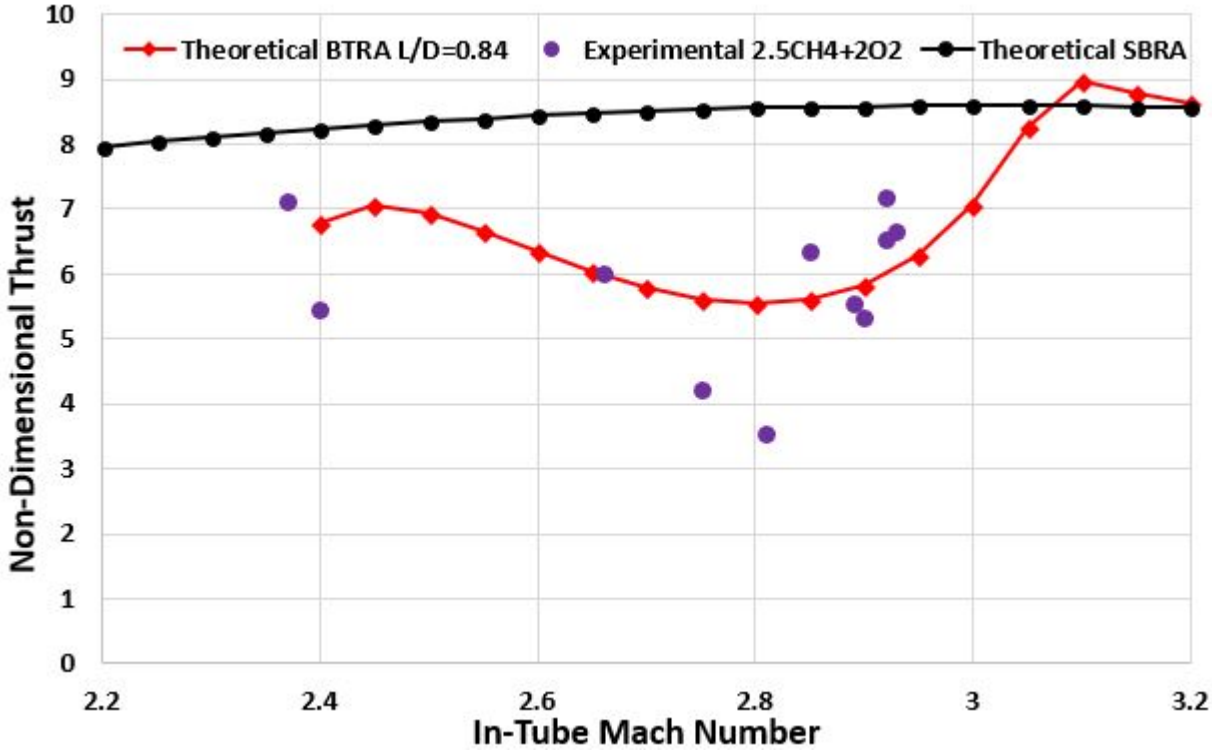

Figure 5.22: Aspect ratio dependent BTRA performance model for $2.5CH_4 + 2O2$ compared to data

The assumption of a single baffle chamber of combustion seemed to work very well for the methane-oxygen based mixtures. When comparing the $1CH_4 + 2O_2 + 7.92N_2$ mixture data to the aspect ratio dependent model, similarly to the $2.5CH_4 + 2O_2$, the agreement of data and theory still hold with no adjustments. The aspect ratio suggests a propulsive cycle periodic with the baffle chambers. Even with a nitrogen diluent the reaction rate does not decrease enough to stretch the combustion zone. The $4CH_4 + 2O_2$ mixture follows the same trend for both inward and outward baffles.

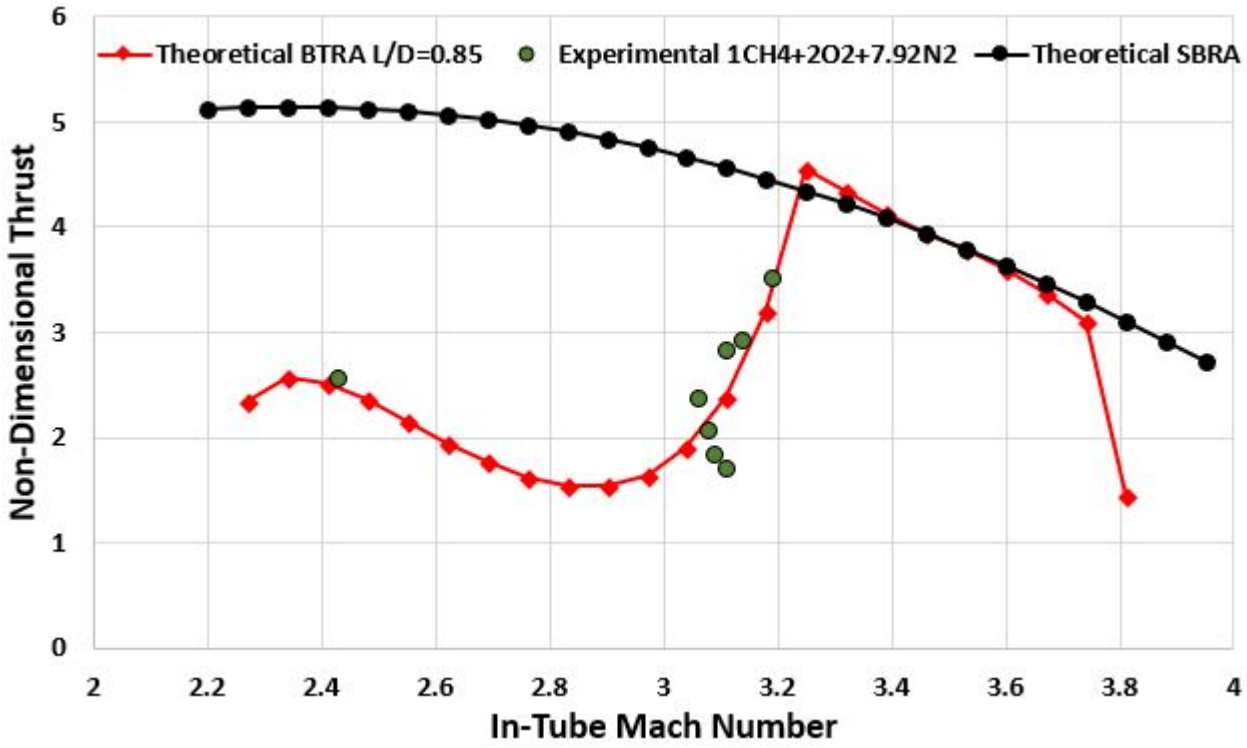

Figure 5.23: Aspect ratio dependent BTRA performance model for $1CH_4 + 2O_2 + 7.92N_2$ compared to data

Both baffle configuration resulted in the same control volume aspect ratio suggesting the mixture is the influencing factor not baffle configuration, according to the control volume analysis in Figure 5.24 and 5.25. The only difference the baffle configuration make is the operational limits of the BTRA. The drag coefficient that was set to 100 for all mixtures could be reduced for the slanted baffles making the effects of drag much less prominent. The Mach number sensitive region where the majority of the data lives would not be effected but from what is understood about the drag, the bump in thrust at low Mach number would vanish with a low enough coefficient. This suggests that perhaps the drag with the slanted BT is lower then the normal BT but that is not necessarily a positive outcome if the drag is relied on to obtain thrust at low Mach numbers.

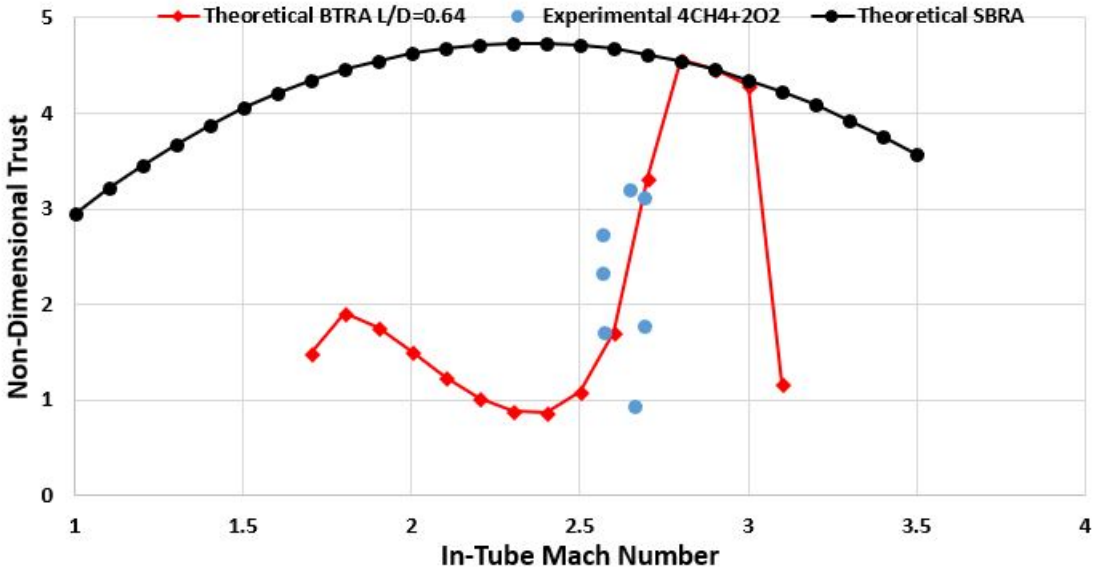

Figure 5.24: Aspect ratio dependent inward slanted BTRA performance model for $4CH_4 + 2O_2$ compared to data

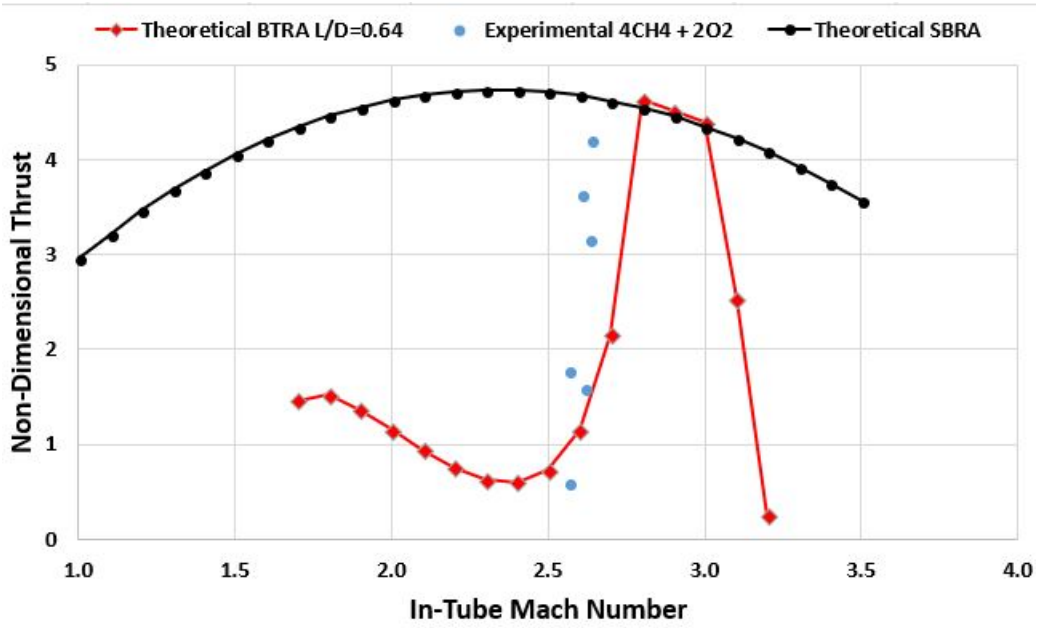

Figure 5.25: Aspect ratio dependent outward slanted BTRA performance model for $4CH_4 + 2O_2$ compared to data

Lastly, with the experimentally determined aspect ratios determined from correlating the model to the data a compared was to the reaction rates. Figure 5.26 shows the aspect ratio and reaction rate for all four normal BT mixtures. The slanted BT mixtures were excluded because the aspect ratios cannot be directly related to the normal BT aspect ratios due to differing hardware geometries. The two quantities seemed to have a relationship similar to a power law which reinforces the ideas stated earlier that a lower reaction rate caused stretching and a high reaction results in a thick but short combustion zone. The association suggested for mixtures in between the reaction rates tested a similar trend will hold true. Ideally a mixture with a medium to low reaction rate may provide the most thrust by taking advantages of a long reaction zone that terminates at the inner diameter of the baffles. This may provide enough shear stress work input and projectile exposure to the peak pressure for a longer time to exceed SBRA model expectations with more non-dimensional thrust then the $1CH_4 + 2O_2 + 2CO_2$ mixture.

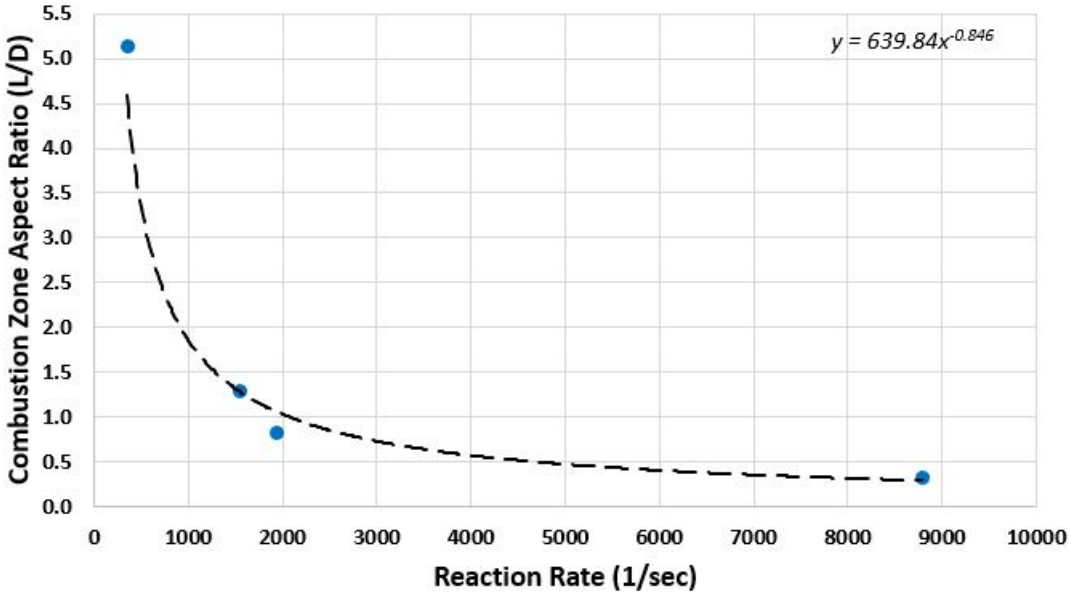

Figure 5.26: Combustion zone aspect ratio related to the reaction rate for a given mixture

Chapter 6

CONCLUSION

The initial experimental results of the slanted BTRA were presented in two configurations: slanted into the flow and out from the flow. The inward slanted BT were believed to be a promising alternative to the normal BT. The implications of each were discussed in detail. In conjunction an investigation of the combustion efficiency of the BTRA was conducted and a modified model was presented. The model attempted to experimentally determined the combustion characteristics of the individually tested mixtures by estimating the aspect ratio of the high pressure region. Data from four different mixtures in the normal BTRA and one mixture in the slanted BTRA configurations were utilized to calibrate the model.

The operational limits of heat release and fill pressure were mainly investigated in the slanted BT. A mixture class of $\phi CH_4 + 2O_2$ was utilized for both configurations, where ϕ ranged was 3, 3.5, and 4. The diameter of the projectile throat was found to play are pivotal role in the thrust production and an optimal 3.61 cm was used in subsequent tests. The inward baffles experiments resulted in thrust production for tests where $\phi = 3.5$ with a fill pressure below 1.4 MPa and $\phi = 4$ with a fill pressure below 1.95 MPa. The outward baffles performed better with successful tests ranging from $\phi = 3$ at fill pressures below 1.76 MPa and $\phi = 4$ at fill pressures below 2.61 MPa. From analyzing the shock system position on the projectile for each configuration the outward slanted baffles seemed to have an expanded operational envelope because the shock system trended toward the projectile suggesting better attenuation. When comparing the outward slanted BT tests to the normal BT tests in a $2.5CH_4+2O_2$ mixture, the slanted baffles produced more thrust at similar Mach numbers. This suggested the outward slanted BT are a promising alternative to realize the

potential thrust predicted by the SBRA theory but a different slant angle must be considered to relax the operational heat release constraint.

Combustion efficiency was defined as the fraction of heat released before the baffles disrupted the thermally choked plane. The reaction rate, or inversely the chemical time scale, was defined as the heat release rate of the mixture over the total heat release at the CJ condition. The time constant for the peak pressure in the combustion zone was defined as the high pressure region velocity in the laboratory frame over a length scale. In the initial study the length scale was defined as the length of a single baffle. The combustion efficiency was applied to the BTRA performance model from Reference [5] and show promising results. Mixtures using methane-oxygen or methane-air show excellent agreement with the assumed length scale, the $2CH_4 + 4N_2O$ and $1CH_4 + 2O_2 + 2CO_2$ did not. On further investigation, changing the length scale predicted the outlying mixtures better. Realizing the combustion length would directly affect the amount of drag applied to the high pressure region the drag and combustion concepts were coupled through the length of the region. The aspect ratio of each mixture was determined by data correlation and applied to the newly derived performance model. It was found that the aspect ratio depends on the reaction rate of the mixture and the length of the combustion zone has an affect on the amount of drag applied. The $1CH_4 + 2O_2 + 2CO_2$ mixture resulted in the highest aspect ratio and consequently the only mixture to out-perform the expected SBRA theory.

6.1 Future Work

There is plenty of research that still can be conducted on the baffled-tube ram accelerator performance, operational envelope, and geometric variations. The aspect ratios presented have yet to be experimentally validated with combustion probing techniques or thermally choked plane identification methods. The slanted BT have not yet been explored using mixtures other than methane-oxygen and Mach numbers above 2.7. Furthermore, no slant angle variations have been tested or designed.

To further validate the proposed modified BTRA performance model, experiments can

be done at higher Mach numbers to determine if the prediction still holds. An ion probe or combustion radical sensing probe can be utilized to further understand the combustion characteristics inside the BT. Using the results from the aspect ratio and reaction rate proposed relation an ideal mixture can be composed. The mixture may be a mixture class containing methane-nitrous oxide-carbon dioxide. Testing the ideal mixture and conducting a similar analysis, detailed above, my prove validity or expose errors in the conclusions made.

BIBLIOGRAPHY

[1] Knowlen, C., "**Theoretical and Experimental Investigation of the Thermodynamics of the Thermally Choked Ram Accelerator**," Ph.D. thesis, University of Washington, April, 10 1991.

[2] Hertzberg, A., Bruckner, A. P., and Bogdanoff, D. W., "**Ram Accelerator: A New Chemical Method for Acceleration Projectiles to Ultrahigh Velocities**," *Journal of Propulsion and Power*, Vol. 14, No. 6, Nov. - Dec., 1988, pp. 195–203.

[3] Knowlen, C., Glusman, J., Bruckner, A. P., and Higgins, A. J., "**Experimental Investigation of a Baffled-Tube Ram Accelerator**," *52nd AIAA/SAE/ASEE Joint Propulsion Conference*, Salt Lake City, UT, July 25 - July 27, 2016.

[4] Higgins, A. J., Knowlen, C., and Bruckner, A. P., "**Ram Accelerator Operating Limits, Part 1: Identification of Limits**," *Journal of Propulsion and Power*, Vol. 14, No. 6, Nov. - Dec., 1998, pp. 951–958.

[5] Glusman, J., "**Theoretical Performance Model and Initial Experimentation of a Baffled-Tube Ram Accelerator**," Master's thesis, University of Washington, 2016.

[6] Daneshvaran, N., "**Transient Computational Fluid Dynamics Modeling of the Baffled-Tube Ram Accelerator**," , 2017.

[7] Tanguay, V., and Higgins, A. J., "**On the Inclusion of Frictional Work in Non-Ideal Detonations**," *20th International Colloquium on the Dynamics of Explosions and Reactive Systems*, Montreal, Canada, July 31 - Aug. 5, 2005.

[8] Bruckner, A. P., Knowlen, C., Hertzberg, A., and Bogdanoff, D. W., "**Operational Characteristics of the Thermally Choked Ram Accelerator**," *Journal of Propulsion and Power*, Vol. 7, No. 5, 1991, pp. 828–836.

[9] Bogdanoff, D. W., Knowlen, C., Murakami, D., and Stonich, I., "**Magnetic Detection for Projectiles in Tubes**," *AIAA Journal*, Vol. 28, No. 11, 1990, pp. 1942–1944.

[10] Jardin, M. R., and Bruckner, A. P., "**Feedback-Controlled Gas Mixing System for the Ram Accelerator**," *Journal of Propulsion and Power*, Vol. 11, No. 6, Nov. - Dec., 1995.

[11] Heflin, L., "**Baffled Tube Ram Accelerator Structural Design**," *AIAA Region VI Student Conference*, Corvallis, OR, April 1 - April 3, 2016.

[12] Hambling, C. H., "**Experimental Investigation of Baffled Tube Ram Accelerator Operational Characteristics**," Master's thesis, Fachhochschule Weiner Neustadt, 2017.

[13] Knowlen, C., Daneshvaran, N., Byrd, T., and Dumas, J., "**Computational Fluid Dynamics Modeling of Baffled Tube Ram Accelerator Experiments**," *AIAA Science and Technology Forum and Exposition*, Kissimee, FL, Jan 8 - Jan 12, 2018.

[14] Knowlen, C., Byrd, T., Dumas, J., Daneshvaran, N., Bruckner, A. P., and Higgins, A. J., "**Baffled Tube Ram Accelerator Combustion**," *26th International Colloquium on the Dynamics of Explosions and Reactive Systems*, Boston, MA, July 30 - Aug. 4, 2017.

[15] Chiping, L., and Kailasanath, K., "**Highly Transient Flow Features in the Ram Accelerator**," Tech. rep., *Naval Research Laboratory*, Laboratory for Computational Physics and Fluid Dynamics, Washington, D.C., 1997.

[16] Sasoh, A., Knowlen, C., and Bruckner, A. P., "**Effect of Finite Rate Chemical Reactions on Ram Accelerator Thrust Characteristics**," *31st AIAA/SAE/ASEE Joint Propulsion Conference*, San Diego, CA, July 10 - July 12, 1995.

[17] Knowlen, C., Higgins, A. J., and Kiyanda, C. B., "**Gasdynamic Operation of Baffled Tube Ram Accelerator in Highly Energetic Mixtures**," *20th International Colloquium on the Dynamics of Explosions and Reactive Systems*, Montreal, Canada, July 31 - Aug. 5, 2005.

[18] Peterson, E. L., and Davidson, D. F., "**Ignition Delay Times of Ram Accelerator Mixtures**," *32st AIAA/SAE/ASEE Joint Propulsion Conference*, Buena Vista, FL, July 1 - July 3, 1996.

[19] Higgins, A. J., "**Ram Accelerator: Outstanding Issues and New Directions**," *Journal of Propulsion and Power*, Vol. 22, No. 6, Nov. - Dec., 2006, pp. 1170–1187.

[20] Higgins, A. J., Knowlen, C., and Bruckner, A. P., "**Ram Accelerator Operating Limits, Part 2: Nature of Observed Limits**," *Journal of Propulsion and Power*, Vol. 14, No. 6, Nov. - Dec., 1998, pp. 959–966.

[21] Knowlen, C., and Bruckner, A. P., "**Direct Space Launch Using Ram Accelerator Technology**," *Space Technology and Applications International Forum*, American Institute of Physics, 2001.

[22] Knowlen, C., Bundy, C., Schwab, R., and Bruckner, A. P., "**University of Washington High Pressure Ram Accelerator Facility**," *Proceedings of the 50th Aeroballistic Range Association*, Pleasant, CA, Nov. 8-12, 1999.

Appendix A

PYTHON CODE USING CANTERA

- The python code used to determine the heat release rate of the mixtures using a minimum of 40 reactions for the chemical kinetics

Initial Temperatures and Pressures taken at the CJ Condition

```
import cantera as ct
import numpy as np
import matplotlib.pyplot as plt

mixtures =['CH4:4, O2:2','CH4:1, O2:2, CO2:2' ,'CH4:2, N2O:4']
Tint = [3153.4,3523,3984.4] #K
Pint = [5.29e7,3.93e7,6.8e7] #Pa
cp = [1.418e3, 0.997e3, 1.096e3]

Q = []
Qdot_array = []
for i in range(len(mixtures)):
gas = ct.Solution('gri30.xml')
initial_state = Tint[i], Pint[i], mixtures[i]
gas.TPX = initial_state
HR = gas.h
gas.equilibrate('TP')
HP = gas.h
```

```
Qdot = np.dot(gas.net_rates_of_progress,gas.delta_enthalpy)
Qdot_array.append(Qdot)
Q.append(HP-HR)



Rmax = np.zeros(gas.n_reactions)
rnet = abs(gas.net_rates_of_progress)
rnet /= max(rnet)
Rmax = np.maximum(Rmax, rnet)
R = sorted(zip(Rmax, gas.reactions()), key=lambda x: -x[0])

Reduced_reactions = list(range(40,200,10))
Qdot_N = []
N_array = []
Q2 = []
for j,N in enumerate(Reduced_reactions):
    # Get the N most active reactions
reactions = [r[1] for r in R[:N]]
# find the species involved in these reactions. At a minimum, include all
    # species in the reactant mixture
species_names = {'CH4', 'O2','CO2','N2O'}
for reaction in reactions:
species_names.update(reaction.reactants)
species_names.update(reaction.products)

    # Get the species objects
species = [gas.species(name) for name in species_names]
```

```
    # create the new reduced mechanism
gas2 = ct.Solution(thermo='IdealGas', kinetics='GasKinetics',species=species, r

# Re-run the ignition problem with the reduced mechanism
initial_state = Tint[i], Pint[i], mixtures[i]
gas2.TPX = initial_state
HR2 = gas2.h
gas2.equilibrate('TP')
HP2 = gas2.h
Qdot_indiv = np.dot(gas2.net_rates_of_progress,gas2.delta_enthalpy)
Qdot_N.append(Qdot_indiv)
N_array.append(N)
Q2.append((HP2-HR2))


fig, ax1 = plt.subplots()
ax2 = ax1.twinx()
ax1.plot(N_array,Qdot_N,'r')
ax2.plot(N_array,Q2,'b')
ax1.set_xlabel('Number of Reactions')
ax1.set_ylabel('Heat Release Rate (W)',color = 'r')
ax2.set_ylabel('Total Heat Release (J)',color = 'b')
plt.title('Reduced Mechanism Heat Release Rates\n'+ mixtures[i])
print('Reduced Mechanism Reaction Heat Release Rate '+ mixtures[i],min(Qdot_N),
print('Reduced Mechanism Reaction Heat Release '+ mixtures[i],min(Q2),'J')
print('Ratio of Heat Release Rate to Total Heat Release '+mixtures[i], min(Qdot
print(mixtures[i]+' Q =',Q2[i]/(cp[i]*298))
```

```
plt.show()
print('Full Mechanism Reaction:',Qdot_array,Q,'W')
```

- The python code used to determine the end state temperature with 40 reactions mechanisms. Each mixture had a different increase of temperature and pressure post shock system based on the specific heat ratio.

The conservation of energy equation was applied to each mixture

```
import numpy as np
import matplotlib.pyplot as plt
import time
import cantera as ct
import math as m

Ru = 8.314 # J/K-mol
T0 = 298 #K
P0 = 150/0.000145038 #psi*(Pa/psi)
theta = 15 #deg
M1 = np.linspace(1,6,5)
#mixture = 'CH4:2 N2O:4'
mixture = 'CH4:4 O2:2 '
#mixture = 'CH4:1 O2:2 CO2:2'
gas = ct.Solution('gri30.xml')
gas.TPX = T0,P0,mixture
#HR = gas.h
cp0 = gas.cp
```

```
g0 = gas.cp/gas.cv
MW0 = gas.mean_molecular_weight/1000 #kg/mol
R0 = Ru/MW0
a0 = m.sqrt(g0*R0*T0)
gas.TP = 0.1,P0
Hf1 = gas.h



T1 = 1.5*298 #K
P1 = 2.25*150/0.000145038 #psi*(Pa/psi)
gas = ct.Solution('gri30.xml')
gas.TPX = T1,P1,mixture
H1 = gas.h
cp1 = gas.cp
MW1 = gas.mean_molecular_weight/1000 #kg/mol
R1 = Ru/MW1
rho1 = gas.density
g1 = gas.cp/gas.cv
a1 = m.sqrt(g1*R1*T1)
E1 = H1 +((M1*a1)**2)/2
Ab = 0.001134*3.009



#Reduce Reaction Mechanisms
Rmax = np.zeros(gas.n_reactions)
rnet = abs(gas.net_rates_of_progress)
rnet /= max(rnet)
```

```
Rmax = np.maximum(Rmax, rnet)
R = sorted(zip(Rmax, gas.reactions()), key=lambda x: -x[0])
# Get the N most active reactions
reactions = [r[1] for r in R[:40]]
# find the species involved in these reactions. At a minimum, include all
# species in the reactant mixture
species_names = {'CH4', 'O2','CO2','N2O'}
for reaction in reactions:
species_names.update(reaction.reactants)
species_names.update(reaction.products)

    # Get the species objects
species = [gas.species(name) for name in species_names]


E6 = np.zeros(len(M1))
T6 = np.zeros(len(M1))
P6 = np.zeros(len(M1))
H6 = np.zeros(len(M1))
HR = np.zeros(len(M1))
HP = np.zeros(len(M1))
a6 = np.zeros(len(M1))
v6 = np.zeros(len(M1))
rho6 = np.zeros(len(M1))
del_q = np.zeros(len(M1))
Qdot = np.zeros(len(M1))
vis = np.zeros(len(M1))
cp6 = np.zeros(len(M1))
```

```
T6guess = 1000 #K
P6guess = P1 #Pa
gas = ct.Solution(thermo='IdealGas', kinetics='GasKinetics',species=species, re
gas.TPX = T6guess,P6guess,mixture
gas.equilibrate('TP')
H6guess = gas.h
MW6guess = gas.mean_molecular_weight/1000 #kg/mol
R6guess = Ru/MW6guess
rho6guess = gas.density
g6 = gas.cp/gas.cv
a6guess = m.sqrt(g6*R6guess*T6guess)
cp6[0] = gas.cp
v6g = a6guess/((M1[0]*a1)*rho1)
P6g2 = (((g6-1)/g6)*cp6[0]*T6guess)/v6g
gas.TP = 0.1,P0
Hf6guess = gas.h
E6guess = H6guess + (a6guess**2)/2
print('Entrance Velocity: ',M1*a0,'m/s\n')


t0 = time.time()
for i in range(len(M1)):
gas = ct.Solution('gri30.xml')
gas.TPX = T6guess,P6g2,mixture
T6[i] = T6guess
E6[i] = E6guess
a6[i] = a6guess
cp6[i] = cp6[0]
```

```
v6[i] = v6g
if (abs(E1[i]) - abs(E6[i])) < 0:
count = 0
while ((E1[i] - E6[i])) > 10:
T6[i] += 1.1
v6[i] = a6[i]/((M1[i]*a1)*rho1)
P6[i] = (((g6-1)/g6)*cp6[i]*T6[i])/v6[i]
gas.TPX = T6[i],P6[i],mixture
gas.equilibrate('TP')
H6[i] = gas.h
MW6 = gas.mean_molecular_weight/1000 #kg/mol
R6 = Ru/MW6
rho6[i] = gas.density
cp6[i] = gas.cp
g6 = gas.cp/gas.cv
a6[i] = m.sqrt(g6*R6*T6[i])
gas.TP = 0.1,P0
Hf6 = gas.h
E6[i] = H6[i]+(a6[i]**2)/2
count += 1
#print(count)
if count == 50000:
break
else:
count = 0
while ((E6[i] - E1[i])) < 10:
T6[i] += 1.1
v6[i] = a6[i]/((M1[i]*a1)*rho1)
```

```
P6[i] = (((g6-1)/g6)*cp6[i]*T6[i])/v6[i]
#HR[i] = gas.h
gas.TPX = T6[i],P6[i],mixture
gas.equilibrate('TP')
H6[i] = gas.h
MW6 = gas.mean_molecular_weight/1000 #kg/mol
R6 = Ru/MW6
rho6[i] = gas.density
cp6[i] = gas.cp
g6 = gas.cp/gas.cv
a6[i] = m.sqrt(g6*R6*T6[i])
gas.TP = 0.1,P0
Hf6 = gas.h
E6[i] = H6[i]+(a6[i]**2)/2
count += 1
#print(count)
if count == 50000:
break
gas.TPX = T6[i],P6[i],mixture
HR[i] = gas.h
gas.equilibrate('TP')
gas.transport_model = "Multi"
vis[i] = gas.viscosity
Qdot[i] = np.dot(gas.net_rates_of_progress,gas.delta_enthalpy)
HP[i] = gas.h
#gas.TP = 0.1,P0
#Hf6[i] = gas.h
del_q[i] = HR[i]-HP[i]
```

```
Qt = del_q/(cp0*T0)
print('Energy State 1: ',E1)
print('Energy State 6: ',E6,'\n')
print('Temperature State 6: ',T6)
print('Pressure State 6: ',P6,)
print('Q/cp0T0: ',Qt,'\n')
print('Count: ',count)
```